$E801215$

AFATL-TR-85-39

Three-Dimensional Unsteady Reactive Two-Phase Flow Analysis to Predict Detonation Transition in Fragmented High Explosives/Warheads

Herman Krier
Martin R Dahm

UNIVERSITY OF ILLINOIS
DEPARTMENT OF MECHANICAL AND INDUSTRIAL ENGINEERING
1206 WEST GREEN
URBANA, ILLINOIS 61801

SEPTEMBER 1985

INTERIM REPORT FOR PERIOD SEPTEMBER 1982 - MARCH 1985

DTIC
ELECTE
OCT 22 1985
A

Air Force Armament Laboratory
AIR FORCE SYSTEMS COMMAND ★ UNITED STATES AIR FORCE ★ EGLIN AIR FORCE BASE, FLORIDA

AD-A160 777

DTIC FILE COPY

AD-A160777

REPORT DOCUMENTATION PAGE

1a. REPORT SECURITY CLASSIFICATION	1b. RESTRICTIVE MARKINGS
Unclassified	None

2a. SECURITY CLASSIFICATION AUTHORITY	3. DISTRIBUTION/AVAILABILITY OF REPORT
	Approved for Public Release;
2b. DECLASSIFICATION/DOWNGRADING SCHEDULE	Distribution Unlimited

4. PERFORMING ORGANIZATION REPORT NUMBER(S)	5. MONITORING ORGANIZATION REPORT NUMBER(S)
UILU-ENG-84-4008	AFATL-TR-85-39

6a. NAME OF PERFORMING ORGANIZATION	6b. OFFICE SYMBOL (If applicable)	7a. NAME OF MONITORING ORGANIZATION
University of Illinois	UIUC	

6c. ADDRESS (City, State and ZIP Code)	7b. ADDRESS (City, State and ZIP Code)
Dept. of Mechanical and Industrial Engr. 144 MEB; 1206 W. Green Urbana, IL 61801	

8a. NAME OF FUNDING/SPONSORING ORGANIZATION Analysis & Strategic Defense Division	8b. OFFICE SYMBOL (If applicable) AFATL/DLYV	9. PROCUREMENT INSTRUMENT IDENTIFICATION NUMBER F08635-82-K-0321

8c. ADDRESS (City, State and ZIP Code)	10. SOURCE OF FUNDING NOS.			
Air Force Armament Laboratory Eglin Air Force Base, Florida 32542	PROGRAM ELEMENT NO.	PROJECT NO.	TASK NO.	WORK UNIT NO.

11. TITLE (Include Security Classification) (See reverse)

12. PERSONAL AUTHOR(S)
HERMAN KRIER and MARTIN R. DAHM

13a. TYPE OF REPORT	13b. TIME COVERED	14. DATE OF REPORT (Yr., Mo., Day)	15. PAGE COUNT
INTERIM REPORT	FROM Sep 82 TO Mar 85	September 15, 1984	168

16. SUPPLEMENTARY NOTATION

Availability of this report is specified on verso of front cover.

17	COSATI CODES		18. SUBJECT TERMS (Continue on reverse if necessary and identify by block number)
FIELD	GROUP	SUB. GR.	Prediction of Detonation Transition in Damaged Warheads; Three-Dimensional Unsteady Two-Phase Reactive fluid mechanics

19. ABSTRACT (Continue on reverse if necessary and identify by block number)
General purpose warheads can provide devastating effects, with best results obtained through maximum reliability of conventional explosive weapon penetration and detonation. However, advances in target hardening technology have created conditions where such explosive-loaded warheads may fail to meet this goal. Prior to fuse initiation, metal containment wall failure and fragmentation of the high explosive can result from the impact forces between the warhead and the hardened target. The detonation that is expected to occur under totally confined conditions may be reduced to an unsteady, rapid deflagration with much less damage to the target. The principal work presented in the report is the development of a three-dimensional unsteady flow model which can be used to predict whether detonation will occur after the impact of a ruptured warhead filled with fragmented high explosive.

The delay of detonation transition can be quite significant if there is sufficient mass loss through container walls. This is clearly demonstrated here, where significant detonation delays could be predicted when using even a quasi, one-dimensional assumption.

(continued on back)

20. DISTRIBUTION/AVAILABILITY OF ABSTRACT	21. ABSTRACT SECURITY CLASSIFICATION
UNCLASSIFIED/UNLIMITED ☒ SAME AS RPT. ☒ DTIC USERS ☐	UNCLASSIFIED

22a. NAME OF RESPONSIBLE INDIVIDUAL	22b. TELEPHONE NUMBER (Include Area Code)	22c. OFFICE SYMBOL
Mr. Mark Amend	904-882-8302	AFATL/DLYV

DD FORM 1473, 83 APR   EDITION OF 1 JAN 73 IS OBSOLETE.

19. ABSTRACT (CONCLUDED)

However, the loss of mass, momentum, and energy through an opening in the case walls is a multi-dimensional phenomenon. Even though the reaction front may progress axially through the damaged explosive, the mass is basically ejected in the radial direction. This turning of the flow is accomplished by changes in momentum and energy which cannot be described accurately by a one-dimensional representation. Clearly a two- or three-dimensional analysis is required to provide a much more accurate description of these dynamic effects.

This report includes significant new findings and is the culmination of more than two years of effort to solve the two- and three-dimensional flow in a reactive gas/solid mixture. The results demonstrate that it may be possible to predict whether a warhead with case failure (and filled with fragmented high explosive) will produce a low order detonation which is weaker than one required to damage structures. A major portion of the report deals with the numerical methods required in order to carry out such solutions. Results include not only pressure histories, but flow velocities, reaction front loci, and temperature distributions.

11. TITLE (CONCLUDED)

Three Dimensional Unsteady Reactive Two-Phase Flow Analysis to Predict Detonation Transition in Fragmented High Explosives/Warheads

PREFACE

This program was conducted by the Department of Mechanical and Industrial Engineering, University of Illinois at Urbana-Champaign, Illinois 61801, under Contract F08635-82-K-0321 with the Air Force Armament Laboratory, Eglin Air Force Base, Florida 32542-5000. Mr. Mark Amend, DLYV, managed the program for the Armament Laboratory. The program was conducted during the period from September 1982 through March 1985.

This report is a companion document to AFATL-TR-85-12, entitled A Fully Viscous Two-Dimensional Unsteady Flow Analysis Applied to Detonation Transition in Porous Explosives, which describes the treatment of the unsteady, two-phase, separated flow conservation equations in one space dimension. This report extends the treatment to two space dimensions.

Accesion For		
NTIS CRA&I		☑
DTIC TAB		☐
Ui.a i. ou..ced		☐
J .sti..cation		
By		
Di.t ib.tion/		
Availability Codes		
Dist	Avail a:d,or Special	

i

(The reverse of this page is blank.)

TABLE OF CONTENTS

LIST OF FIGURES

LIST OF FIGURES (CONCLUDED)

LIST OF TABLES

NOMENCLATURE

Symbol	Definition	Units
a	Speed of sound in gas	cm/s
A_h	Surface area of crack	cm^2
C_{v_g}	Gas constant volume specific heat	erg/g·K
C_{v_p}	Particle constant volume specific heat	erg/g·K
C_0	Opening ratio for 1-D crack	
d_{p_0}	Initial particle diameter	μm
D	Interphase drag term	$g/cm^2·s^2$
E^g_{chem}	Gas chemical energy	ergs/g
E^p_{chem}	Particle chemical energy	ergs/g
E_{gt}	Gas total energy	ergs/g
E_{pt}	Particle total energy	ergs/g
f_{pg}	Interphase friction factor	
h_{pg}	Convective heat transfer coefficient	$ergs/s·cm^2·K$
K_0	Bulk modulus of solid	$g/cm·s^2$
k_g	Gas thermal conductivity	ergs/s·cm·K
ℓ_0	Stand-off distance of crack	cm
L	Total length of bed	cm
m_{r_1}	Gas bulk momentum in the $\vec{r}$-direction	$g/cm^2·s$
m_{r_2}	Particle bulk momentum in the $\vec{r}$-direction	$g/cm^2·s$
m_{θ_1}	Gas bulk momentum in the $\vec{\theta}$-direction	$g/cm^2·s$

Symbol	Definition	Units
$m_{\theta 2}$	Particle bulk momentum in the $\hat{\theta}$ -direction	$g/cm^2 \cdot s$
$m_{z 1}$	Gas bulk momentum in the $\hat{z}$ -direction	$g/cm^2 \cdot s$
$m_{z 2}$	Particle bulk momentum in the $\hat{z}$ -direction	$g/cm^2 \cdot s$
n	Number of cells cracked	
P_g	Gas phase pressure	$dynes/cm^2$
P_p	Particle phase pressure	$dynes/cm^2$
P_1	Bulk gas phase pressure	$dynes/cm^2$
P_2	Bulk particle phase pressure	$dynes/cm^2$
Pr	Gas Prandtl number	
$\dot{Q}$	Interphase convective heat transfer	$ergs/cm^3 \cdot s$
r_p	Particle radius	μm
$\dot{r}$	Surface burning rate	cm/sec
R	Total bed radius	cm
R'	Gas constant	$ergs/mole \cdot K$
$\hat{r}$	Unit vector in radial direction	
S_ϕ	Generalized source/sink term	
$S_{\phi 1}$	Generalized gas phase source/sink term	
$S_{\phi 2}$	Generalized particle phase source/sink term	
t	time	sec
T_g	Gas temperature	K

Symbol	Definition	Units
T_p	Particle temperature	K
u_g	Gas phase velocity in the x-direction in 1-D model and in the $\vec{r}$ -direction in the 3-D model	cm/sec
u_p	Particle phase velocity in the x-direction in 1-D model and in the $\vec{r}$ -direction in the 3-D model	cm/sec
v_g	Gas phase velocity in the azimuthal direction	cm/sec
v_p	Particle phase velocity in the azimuthal direction	cm/sec
V_{cv}	Volume of control cell	cm^3
w_g	Gas phase velocity in the axial direction	cm/sec
w_p	Particle phase velocity in the axial direction	cm/sec
W	Ratio of crack length to total bed length	cm/cm
$\vec{z}$	Unit vector in the axial direction	
β_g	Gas phase mass loss term in pseudo 1-D model	
β_p	Particle phase mass loss term in pseudo 1-D model	
Δr	Distance between nodes in the $\vec{r}$ -direction	cm
Δx	Distance between nodes in the $\vec{x}$ -direction	cm

NOMENCLATURE (concluded)

Symbol	Definition	Units
Δz	Distance between nodes in the $\vec{z}$ -direction	cm
$\Delta\theta$	Angle between nodes in the $\vec{\theta}$ -direction	rads
δ	Differencing operator	
ϕ	Porosity	
Γ	Gas production rate from particles	$g/cm^3 \cdot sec$
μ_g	Interphase viscosity	$g/cm \cdot sec$
$\vec{\theta}$	Unit vector in the azimuthal direction	
θ_1	Location of left-hand azimuthal boundary	rads
θ_2	Location of right-hand azimuthal boundary	rads
ρ_g	Gas density	g/cm^3
ρ_p	Particle density	g/cm^3
ρ_1	Gas bulk density	g/cm^3
ρ_2	Particle bulk density	g/cm^3

SECTION I

INTRODUCTION

With recent developments in target hardening technology, damage to the casings of impacting bombs prior to initiation of the explosive charge by the fuse has been occurring with increasing frequency. The work done here was motivated by the desire to be able to predict whether or not detonation will occur in warheads whose casings have been fractured. The existence of a hole in the casing which confines the explosive can be expected to have a considerable effect on the formation of a detonation wave in the explosive. The purpose of this work is to present a model which will determine the extent of this effect.

An on-going effort has been present at the University of Illinois at Urbana-Champaign for the past several years, under the direction of Professor Herman Krier, to develop a model which accurately describes the fluid mechanics that result from flame spreading through a fragmented (and thus porous) high-energy solid propellant or explosive media. The thrust of this effort has been to: (a) formulate the equations of motion governing the fluid dynamics of a combusting propellant bed and, (b) develop a stable numerical scheme using these equations that will predict the transition from deflagration to detonation (DDT) in a confined propellant bed. Previous studies (including those of Van Tassel and Krier [1], Krier and Gokhale [2], Krier, Rajan, and Van Tassel [3], Dimitsein [4], Krier, Dimitstein, and Gokhale [5], Krier, Gokhale, and Hughes [6], Krier and Kezerle [7], and Butler, Krier, and Lembeck [8]) have laid a strong foundation towards the achievement of the goal. Models were derived to treat the unsteady, two-

1

phase, separated flow conservation equations in one space dimension and these were incorporated into a computer code which yielded stable solutions for a wide range of input parameters. In its present form, the existing code is capable of showing the rapid building up of a pressure shock front from an initially quiescent, but locally ignited bed of packed, granulated particles and predicting the formation of a steady-state detonation wave, provided that the motion of the gas and particle phases is in one space dimension only. (This has been shown experimentally to be the case for flame spreading through a granulated propellant or explosive material which is completely enclosed in a solid container (Reference 9).) Table 1 is a list which compares the detonation conditions predicted by this one-dimensional DDT code for various values of the initial particle density and porosity with the results predicted by a steady-state thermo-chemical code (Reference 10); it illustrates the high degree of accuracy using these methods.

TABLE 1. COMPARISON OF DATA FROM 1-D CODE AND TIGER CODE
(ρ_0 AND ϕ_0 ARE INPUT PARAMETERS)

	ρ_0(g/cc)	ϕ_0	P_{CJ}(GPa)	T_{CJ}(°K)	ρ_{CJ}(g/cc)
DDT - Code	1.20	0.368	14.38	4201	1.64
TIGER	1.20	0.368	14.92	4337	1.65
DDT - Code	1.30	0.316	16.90	4289	1.76
TIGER	1.30	0.316	17.26	4304	1.78
DDT - Code	1.33	0.300	18.11	4406	1.80
TIGER	1.33	0.300	18.00	4300	1.81
DDT - Code	1.40	0.263	19.64	4393	1.87
TIGER	1.40	0.263	19.60	4280	1.89

In its current state, the model can predict DDT in fractured high explosives contained within undamaged bomb casings, but does not contain the necessary considerations for modeling the accelerated flame spreading in realistic 2-D and 3-D bomb casing configurations, since one of the assumptions in its formulation was that the flow was strictly one dimensional. The addition of cracks or holes in the container walls (partial confinement) would cause the flow to become multi-dimensional. The work presented in this report undertakes to develop a model of a combusting propellant bed which is not always totally confined, that is, in which some of the gas generated by the burning fragments is allowed to escape (along with, perhaps, some of the entrained particles).

Two approaches to solving this problem are discussed: (a) modifying the conse /ation equations in the one-dimensional model to include loss terms which simulate the mass, momentum, and energy escaping through the holes in the casing, and (b) developing a new, unsteady, three-dimensional flow model with a new numerical scheme, which incorporates the hole in the casing as a boundary condition to the flow.

Approach (a), which is discussed in detail in Section II, utilizes pseudo-sink terms in the conservation equations which simulate the effects of mass loss on the formation of a pressure wave in the burning particle bed. The approach was taken as a first approximation of the effect of partial confinement since the working one-dimensional model was already available. Clearly, since the mass would be ejected out of the domain in a direction transverse to the direction of the flame spreading, the problem becomes multi-dimensional. However, even though the quasi two-dimensional formulation will not yield exact results, it can provide meaningful physical insight into the

3

behavior of partially confined accelerating reactive flows. This phase of the work has been successfully completed and published in a proceedings (Reference 11). The results are both reasonable and consistent.

Approach (b) is much more ambitious in its scope. It requires the two-phase, unsteady, separated flow conservation equations to be expressed in three space dimensions and a new stable numerical scheme to be developed which can solve these very non-linear, coupled time-dependent equations. Once this has been done, the condition of partial confinement can then be added in by simply using the appropriate boundary condition. However, the difficulty of developing a stable numerical scheme to integrate these coupled, hyperbolic partial differential conservation equations alone provides a formidable task. When coupled to the large domain of the problem the task becomes even more difficult. It is therefore apparent that this phase of the work cannot be expected to have been seen through to its completion in the short year that it has been underway. However, important strides have been made toward that completion. Section III of this report presents the formulation of the unsteady, three-dimensional, two-phase reactive flow model, while the numerical scheme is discussed in Section IV. Results currently available are presented in Section V.

SECTION II

THE PSEUDO TWO-DIMENSIONAL FORMULATION

1. INTRODUCTION

Impact forces imparted from hardened concrete targets to aerial bombs
can, in some cases, cause outer case failure and breakup of the high explosive
filler. The detonation wave which may be expected to form if the bomb casing
were undamaged (total confinement of the explosive media) may be reduced or
even quenched completely in the presence of the damaged casing (partial
confinement). In this chapter the effect of partial confinement is
investigated by adding quasi two-dimensional sink terms to the equations of
mass, momentum, and energy that describe the accelerating flame spreading
through a granular high explosive. These sink terms are formulated by
assuming that the gas escapes from the hole at the choked velocity for the
local pressure conditions at the hole location. It is clear from the results
presented that such partial confinement can indeed have a significant effect
on the formation of a detonation wave.

2. Assumptions

The important assumptions in formulating this psuedo one-dimensional
model are listed below.

a. The analysis considered here explicitly assumes that at time $t = 0$,
the warhead has already impacted with the surface, and the explosive filler
has already fragmented, causing damage to the casing (see Figure 1). It is
also assumed that at $t = 0$, ignition of a small region of the explosive by the
fuse had already occurred.

b. The deflagration and possible transition to detonation occurs only in one direction (x-space).

c. The surface-to-volume ratio of the fragmented particles is sufficiently high that they may be treated as uniform pseudo-spheres, typically of the millimeter or sub-millimeter diameter.

d. The unsteady two-phase, separated flow analysis previously developed in Reference 8 represents the basis upon which this model was built.

e. The possibility of mass, momentum, and energy loss is treated by psuedo-side venting from cracks of prescribed width, length, and location.

f. The decision on whether the fragmented bed of explosive will detonate is based on the transient reacting flow events occurring in the first 10 to 20 cm of length. A run-up length of greater than 20 cm requires times well beyond established experimental DDT events.

g. The explosive particles, when ignited, burn at a rate $\dot{r} = aP^n$ where a and n are assumed to be known constants for typical high explosives used in warheads. Ignition is assumed to have occurred when a prescribed critical temperature is reached by the particles (see Reference 8).

h. The porosity (gas volume/total volume) of the fragmented bed is assumed initially to be uniform, and typically in the range of 0.2 to 0.3.

6

i. The product gases obey a non-ideal equation of state (see Reference 7).

j. Heat transfer from the gas to the solid is by rapid convection only; conduction and radiation are ignored.

k. The gas is assumed to be inviscid. The drag between the gas and particle phase is included as a source/sink term in the momentum and energy equations. (This is equivalent to assuming that the gas-gas momentum viscous losses are orders of magnitude less than the gas-particle viscous interaction.)

l. The equations are expressed as averaged-laminar flow properties in that the turbulence due to the two-phase nature of the problem has been averaged out.

3. THE FLUID MECHANICS MODEL

In the analysis of two-phase reactive flow, one must describe the conservation of mass, momentum, and energy throughout the domain for both the solid particle phase and the gaseous products phase. In separated flow analysis, each phase is assumed to be a continuum, and the important quantities of mass, momentum, and energy are therefore conserved separately in each phase. The governing differential equations are presented below, including the modifications made in this work to account for the losses occurring through the hole in the casing. For a detailed derivation of the basic equations, the reader is referred to Reference 7.

7

GAS PHASE CONTINUITY

$$\frac{\partial \rho_1}{\partial t} = - \frac{\partial(\rho_1 u_g)}{\partial x} + \Gamma - \beta_g \qquad (1)$$

SOLID PHASE CONTINUITY

$$\frac{\partial \rho_2}{\partial t} = - \frac{\partial(\rho_2 u_p)}{\partial x} - \Gamma - \beta_p \qquad (2)$$

GAS PHASE MOMENTUM

$$\frac{\partial(\rho_1 u_g)}{\partial t} = - \frac{\partial(\rho_1 u^2_g)}{\partial x} - \frac{\partial(P_g \phi)}{\partial x} - D + \Gamma u_p - \beta_g u_g \qquad (3)$$

SOLID PHASE MOMENTUM

$$\frac{\partial(\rho_2 u_p)}{\partial t} = - \frac{\partial(\rho_2 u^2_p)}{\partial x} - \frac{\partial(P_p[1-\phi])}{\partial x} + D - \Gamma u_p - \beta_p u_p \qquad (4)$$

GAS PHASE ENERGY

$$\frac{\partial(\rho_1 E_{gt})}{\partial t} = - \frac{\partial(\rho_1 E_{gt} u_g + \phi u_g P_g)}{\partial x} - D u_p - \dot{Q}$$

$$+ \Gamma(E^g_{chem} + \frac{u^2_p}{2}) - \beta_g E_{gt} \qquad (5)$$

SOLID PHASE ENERGY

$$\frac{\partial(\rho_2 E_{pt})}{\partial t} = - \frac{\partial(\rho_2 E_{pt} u_p + (1-\phi) u_p P_p)}{\partial x} + D u_p + \dot{Q}$$

$$+ \Gamma(E^p_{chem} - \frac{u^2_p}{2}) - \beta_p E_{pt} \qquad (6)$$

In the energy equation,

$$E_{gt} = C_{vg} T_g + 0.5 \, U_g^2$$

8

and $\quad E_{pt} = C_{vp}T_p + 0.5\ U_p^{\ 2}$

The subscripts g and p denote the gas and particle phase respectively. The quantities ρ_1 and ρ_2 in equations (1) - (6) refer to the bulk densities for each phase and are defined as

$$\rho_1 = \rho_g\phi$$
$$\rho_2 = \rho_p(1-\phi)$$

The porosity ϕ is defined as the ratio of instantaneous gas volume to the mixture volume. Hence, the solids fraction is $1-\phi$. The B_g and B_p terms in Equations (1) - (6) are the sink terms which account for the losses through the cracked casing. They are derived in detail in the next section.

In addition to the six conservation equations, several constitutive relations are necessary for closure. The relations used in this work are presented in detail in Appendix A, along with some discussion on their validity under the extreme conditions imposed by this problem. The necessary equations are:

(A-1) An equation of state for the gaseous products phase, $P_g = P_g(\rho_g, E_g)$.

(A-2) An equation of state for the solid particle phase, $\rho_p = \rho_p(P_p)$.

(A-3) A relation for predicting the instantaneous porosity, ϕ.

(A-4) A relation for the interphase heat transfer, $\dot{Q}$.

(A-5) A gas particle interphase drag relation, D.

(A-6) An equation determining the gas generation by the burning particles, Γ.

(A-7) An ignition criteria.

9

4. DERIVATION OF THE MASS LOSS TERM

The condition of partial confinement requires that extra terms be added to the conservation equations in Reference 7. Figure 2 shows the fragmented bed being modeled. The fourth volume cell from the left shows the crack in the casing, exposing the granulated propellant inside. Superimposed on the front face of the illustration are the pressure versus distance profiles showing the expected pressure drop at the hole.

Consider now the single control volume with a hole in it shown in Figure 3. Pressure gradients due to combustion are causing gas flow in the x-direction, as well as causing some of the mass to flow out of the hole. The rate of mass flow of the gas out of the hole, per unit volume, is given by:

$$B_g = \frac{\dot{m}_\ell}{V_{cv}} \tag{7}$$

$$\dot{m}_\ell = \rho_g U A_h \tag{8}$$

where ρ_g = gas density

U = velocity of gas leaving the control volume

A_h = area of the hole

Due to the high gas pressures present in the bed, we can assume that the flow of the gas out of the hole into the atmosphere will always be choked. Hence, U will always be the local speed of sound:

$$U = \left[\left(\frac{\partial p}{\partial \rho} \right)_s \right]^{\frac{1}{2}} = U_s \tag{9}$$

A detailed derivation of the speed of sound equation for the non-ideal gas used in this model can be found in Appendix B.

The area of the hole is defined as:

$$A_h = \Delta x' \Delta x \phi \tag{10}$$

Note that ϕ is included in the definition of A_h since, in the separated flow analysis, only the area of the hole occupied by the gas is considered.

The volume of the control cell is given by $V_{cv} = \Delta x^3$. Substituting back into the expression for β_g, one obtains

$$\beta_g = \frac{\dot{m}_\ell}{V_{cv}} = \frac{\rho_g U_s \Delta x \, \Delta x' \phi}{\Delta x^3} = \frac{\rho_1 U_s}{\Delta x} \left(\frac{\Delta x'}{\Delta x}\right) \tag{11}$$

$$\beta_g = \frac{\rho_1 U_s}{\Delta x} C_o \tag{12}$$

where C_o is a prescribed constant which defines the width of the crack.

If one were to consider entrainment of some of the particles of unburned solid propellant in the gas which is escaping out of the hole, the mass loss for the solid phase may be written as:

$$\beta_p = \frac{\rho_p U_p A_h}{\Delta x^3}$$

$$\beta_p = \frac{\rho_2 U_s D_o}{\Delta x} C_o \tag{13}$$

where D_o is a prescribed drag factor between the entrained particles and the escaping gas, $0 \leq D_o \leq 1$.

11

The momentum losses through the hole then become $\beta_g U_g$ and $\beta_p U_p$ for the gas and particle phase, respectively. Note that the velocity in the x-direction is used in these terms rather than the sound speed. This is done because of the one-dimensional formulation of the equations of motion. The quantity of interest is the amount of momentum in the x-direction which the ejected mass removes from the domain.

Likewise, the sink terms in the energy equations are $\beta_g E_{gt}$ and $\beta_p E_{pt}$ for the gas and particle phase, respectively. Note that the work term found in the flux terms of Equations (5) and (6) are not included in the mass loss term because there is no work done in the x-direction in removing the mass from the domain.

5. NUMERICAL SOLUTION OF THE CONSERVATION EQUATIONS

The highly non-linear partial differential equations (1) - (6) do not admit any analytical solutions. In order to obtain solutions, the time-dependent equations were discretized over the domain and solved numerically via the method of lines. In this approach, the flux terms on the right-hand side of Equations (1) - (6) are evaluated as centered finite differences, along with any source/sink terms. The remaining differential equations are then treated as ordinary differential equations and solved via an O.D.E. solver. For example, Equation (1):

$$\frac{\partial \rho_1}{\partial t} = - \frac{\partial(\rho_1 U_g)}{\partial x} + \Gamma - \beta_g \tag{14}$$

would be solved by first evaluating the terms on the right-hand side of the equation at the current time level to get, say, $G(t)$. This result is then put back into Equation (1) to give:

12

$$\frac{\partial \rho_1}{\partial t} = G(t) \qquad (15)$$

This is an ordinary differential equation with ρ_1 as the dependent variable and t as the only independent variable. Now an O.D.E. solver such as Runge-Kutta may be employed to predict the new value of ρ_1. In this work a variable time step Runge-Kutta-Fehlberg fourth-fifth order algorithm was used. (For more information on the method of lines, the reader is referred to Reference 12.)

6. COMPUTED RESULTS

The model described in the previous sections is first applied to a baseline case, one in which there is no hole in the confining wall (total confinement, $C_0 = 0.0$). The results for this case are then compared with the output for cases where holes of various length, width, and location have been introduced into the wall. The important input parameters for these cases are listed in Table 2. The output presented here is primarily in the form of pressure profiles and plots of the locus of the flame front. These profiles are presented in preference to others because pressure and flame front velocity are the two most critical parameters in determining whether or not a detonation will occur.

Figure 4 shows the pressure versus distance profiles for various times for the baseline (no hole) case. The plot shows the shock building and advancing through the bed as time progresses. At $x = 9.0$ cm the peak pressure is almost 14.0 GPa, which is just a little less than the Chapman-Jouget (CJ) detonation pressure for an explosive with this bulk density (see Reference 8).

13

TABLE 2.   INPUT PARAMETERS FOR 1-D MODEL

Bed Length, L	10 cm
Particle Radius, r_{po}	200 μm
Porosity, ϕ_o	0.3
Pressure, P_{go}	1×10^5 GPa
Gas Temperature, T_{go}	300 °K
Particle Temperature, T_{po}	300 °K
Ignition Temperature, T_{ign}	306 °K
Chemical Energy of Solid, E_{chem}	5.74 MJ/kg
Gas Constant, R'	296.8 J/kg °K
Prandtl Number of Gas, Pr	0.70
Constant Volume Specific Heat, C_v	1500 J/kg °K
Interphase Viscosity, μ	1.80×10^{-3} Ns/m^2
Burning Rate Index, n	1.0
Coefficient in Burning Rate, a	0.001
Co-efficient in Equation of State, b_1	4.0
Node Size, Δx	1 mm

Figure 5 shows the effect of having placed a hole 4 mm in length with an opening ratio (C_o) of 0.5 at a distance of 2.5 cm from the initiated end of the bed. The location of the hole on the plot is evident from the severe indentation in the pressure profile. It is interesting to compare the profile at $t = 68$ μsec for Figures 4 and 5. As one can see, the presence of the hole has reduced the peak pressure by almost 6 GPa, while retarding the advance of the flame front by 2 cm. Indeed, even at $t = 72$ μsec, the peak pressure is still about 3 GPa less than the baseline case at $t = 68$ μsec.

Figures 6 and 7 compare the effect of varying the width (C_o) of the crack while keeping the length constant at 4 mm. Figure 6 shows the pressure profiles at $x = 5.0$ cm for various values of C_o. It is apparent that as C_o increases, the profiles converge. Figure 7 shows the effect of the various C_o's on the flame front velocity. As can be seen from the plots, the flame

14

front achieves a constant velocity near the end of the burn. This final Chapman-Jouget velocity is one of the critical parameters in determining detonation. As one can see from the plots, the final velocity decreases as C_0 increases. We also see that the flame profiles again converge for large values of C_0.

Figures 8 and 9 show the effect of varying the length of the crack while keeping C_0 constant at a value of 0.1. Figure 8 shows the pressure versus distance profiles at t = 58 usec for cracks ranging from 4 mm to 16 mm in length. As one can see, varying the length of the crack has a more severe effect on the profile than varying C_0. For the case where W = 0.16 (16 mm crack), the peak pressure in the bed is a mere fraction of the value obtained for the totally confined case. Moreover, Figure 9 shows that the final flame front velocity has been reduced from 5.2 mm/usec to only 2.7 mm/usec.

While results such as Figure 5 shows that partial confinement does indeed have a significant effect on the forming detonation wave, one is still concerned whether, after encountering a hole in the confining wall, the reaction wave could possibly recover and still form a detonation wave if there were a sufficient length of confined bed downstream of the hole. Therefore, a condition was simulated for a bed of 20 cm length with no hole in the casing. This result was then compared to another 20 cm long bed in which a hole with W = 0.02 (2 mm in length) and a C_0 = 0.20 had been introduced into the casing. Figure 10 shows the pressure versus distance profile for the partially confined bed. Also shown is the maximum pressure achieved by the totally confined bed. As one can see, even though the process in the partially confined case required 10 usecs longer, the peak pressure in the damaged case has almost completely recovered the depressurization suffered due

15

to the hole. Figure 11 further confirms this recovery by showing that the final velocities of the two flame fronts are almost equal for the two cases. This result was somewhat unexpected. It was at first believed that the presence of such a hole would permanently quench a detonation. Of course, a crack of much longer width would likely prevent a detonation altogether.

Finally, a case was run in which the conditions for the crack formation were changed. Instead of assuming that the crack already existed at prescribed locations at $t = 0$, it was assumed that the impact with the hardened surface had instead weakened the casing so that if the pressure inside the bed exceeded a prescribed critical pressure, the casing would crack. The model was set up so that when the pressure at any point in the bed exceeded 5 kbar (72,500 psia) a crack with $C_0 = 0.1$ and $W = 0.01$ would form at that location.

Figure 12 shows the pressure versus distance profile for this case. As can clearly be seen the pressure in the damaged explosive never exceeds the prescribed critical pressure. Therefore it would be impossible for a detonation to occur if such physics as modeled were actually valid. Figure 13 shows the flame front locus for the totally confined case and for two cases where the casing fails at a prescribed pressure -- one at $P = 0.5$ GPa and one at $P = 1.0$ GPa. One can see the severe reduction in the final flame velocity caused by the erupting cracks.

7. CONCLUSIONS AND REMARKS

The results presented in the previous section verify the fact that incomplete confinement of the explosive media does have a strong affect on the

formation of a steady-state detonation wave in a fragmented explosive. The presence of a hole can bring about a very significant reduction in the gas pressure as well as cause a severe reduction in the reaction front velocity. The results also showed that if a sufficient length of confined bed remained downstream of the hole, a detonation wave could recover and still reach steady-state detonation.

The procedure outlined in this section, while providing results which are heuristically reasonable, does make some major simplifying assumptions in order to allow us to use the existing, proven one-dimensional flame spreading model. Perhaps the greatest weakness of this model is that it does not simulate the actual two and/or three dimensional processes of the gas and particles flowing out of the hole. Since the one-dimensional model allows only flow in the direction of the deflagration front, it is impossible to model the turning of the gas as it gains y and z velocity components. Furthermore, the one-dimensional model does not allow us to take the geometry of the bomb or the cracks into account.

Therefore, we thought it necessary to formulate an unsteady flame spreading model in three space dimensions to allow us to simulate this problem with greater accuracy. In such a three-dimensional model, the hole in the confining wall would simply become a boundary condition which allows the normal velocity component at the wall to be nonzero. (Rather than the usual boundary condition which states that the normal velocity component at the wall must be zero.)
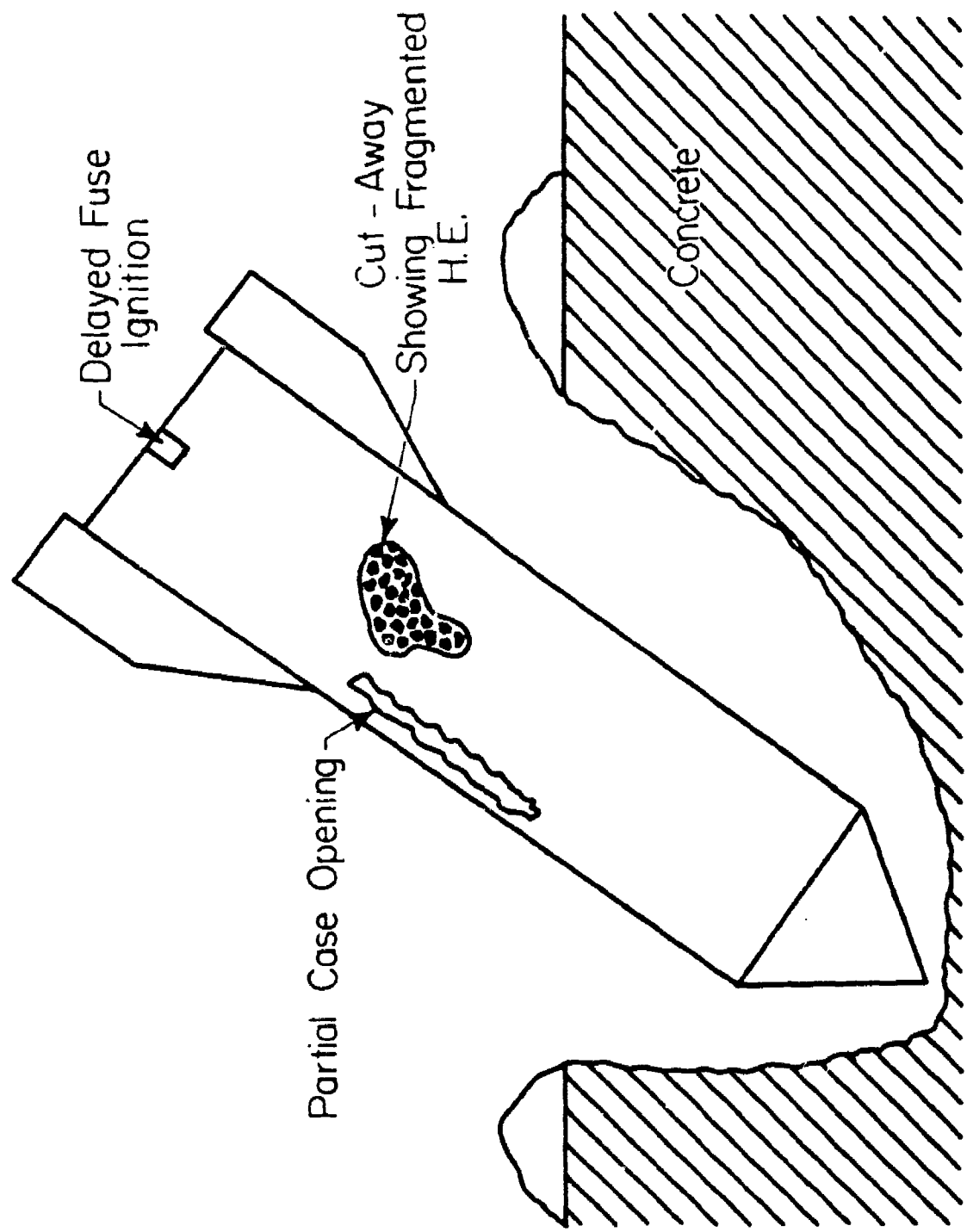
Figure 1. Schematic of Impact Damaged Warhead

Delayed Fuse Ignition

Cut - Away Showing Fragmented H.E.

Partial Case Opening

Concrete

18
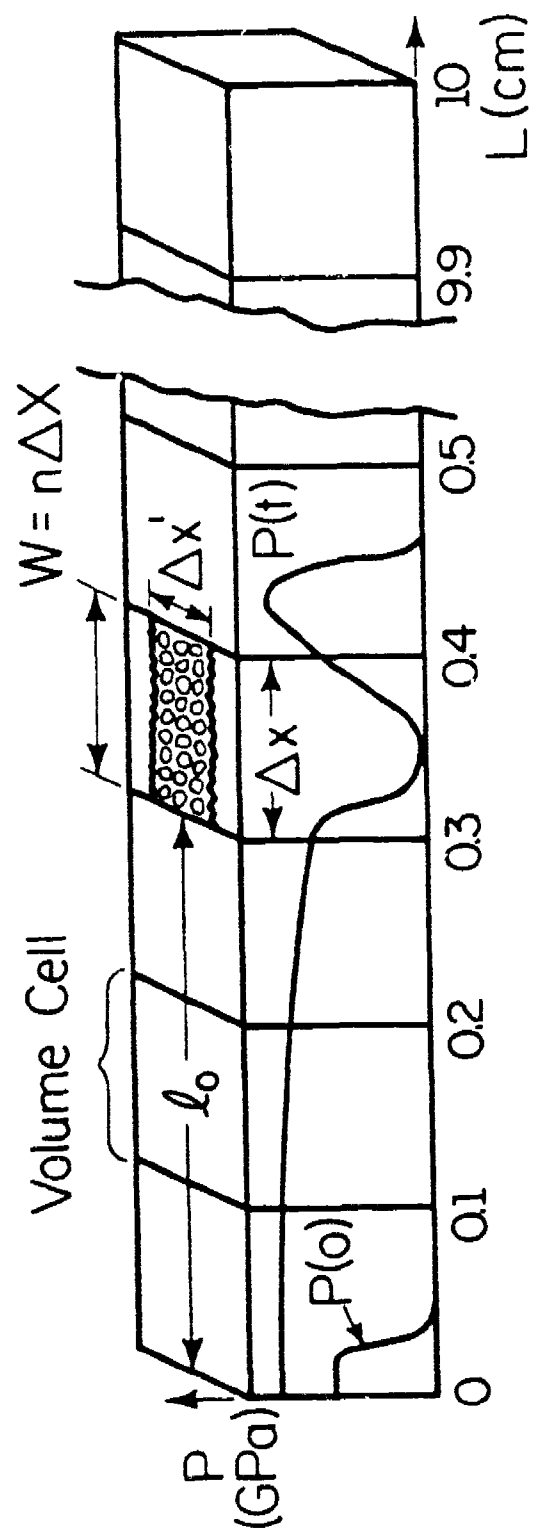
Variables:

ℓ_o = distance from Ignition end of bed to hole
$C_o = (\Delta x'/\Delta x)$, width of hole, $\Delta x'$, may be varied
n = number of volume cells with holes

Figure 2. Schematic of Explosive Bed Showing Assumed Crack in Casing

19
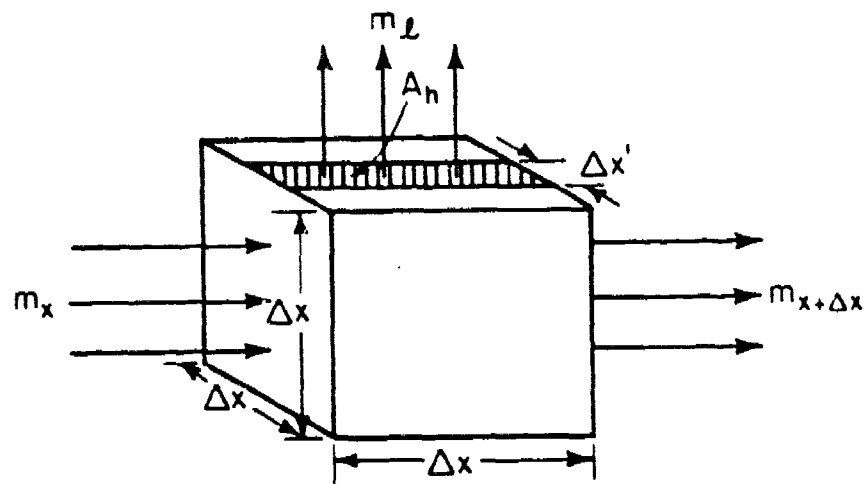
Figure 3. Single Volume Cell Showing the Hole on the Top Face
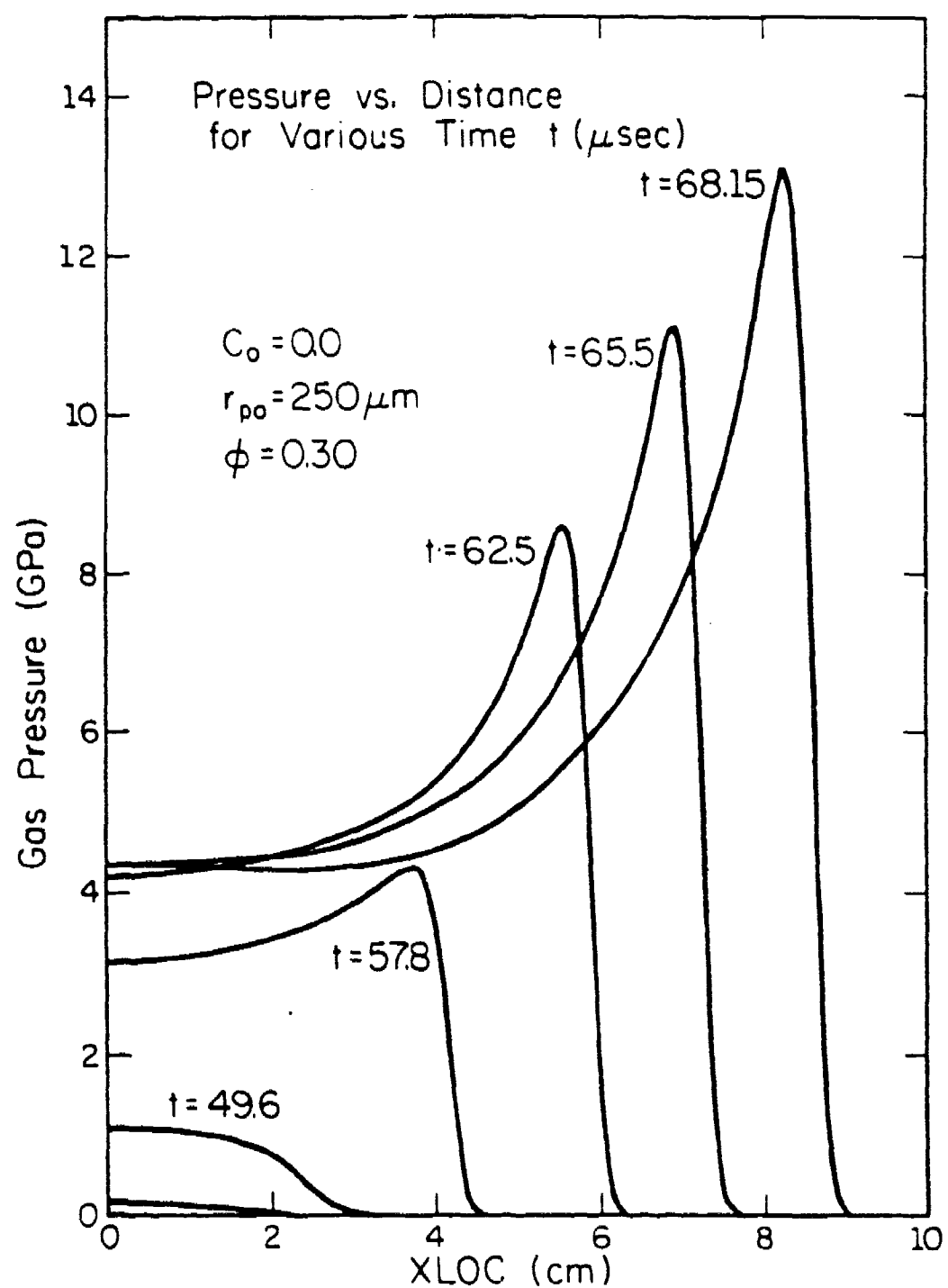
Figure 4.   Pressure History for Baseline Case (no crack in casing)

21
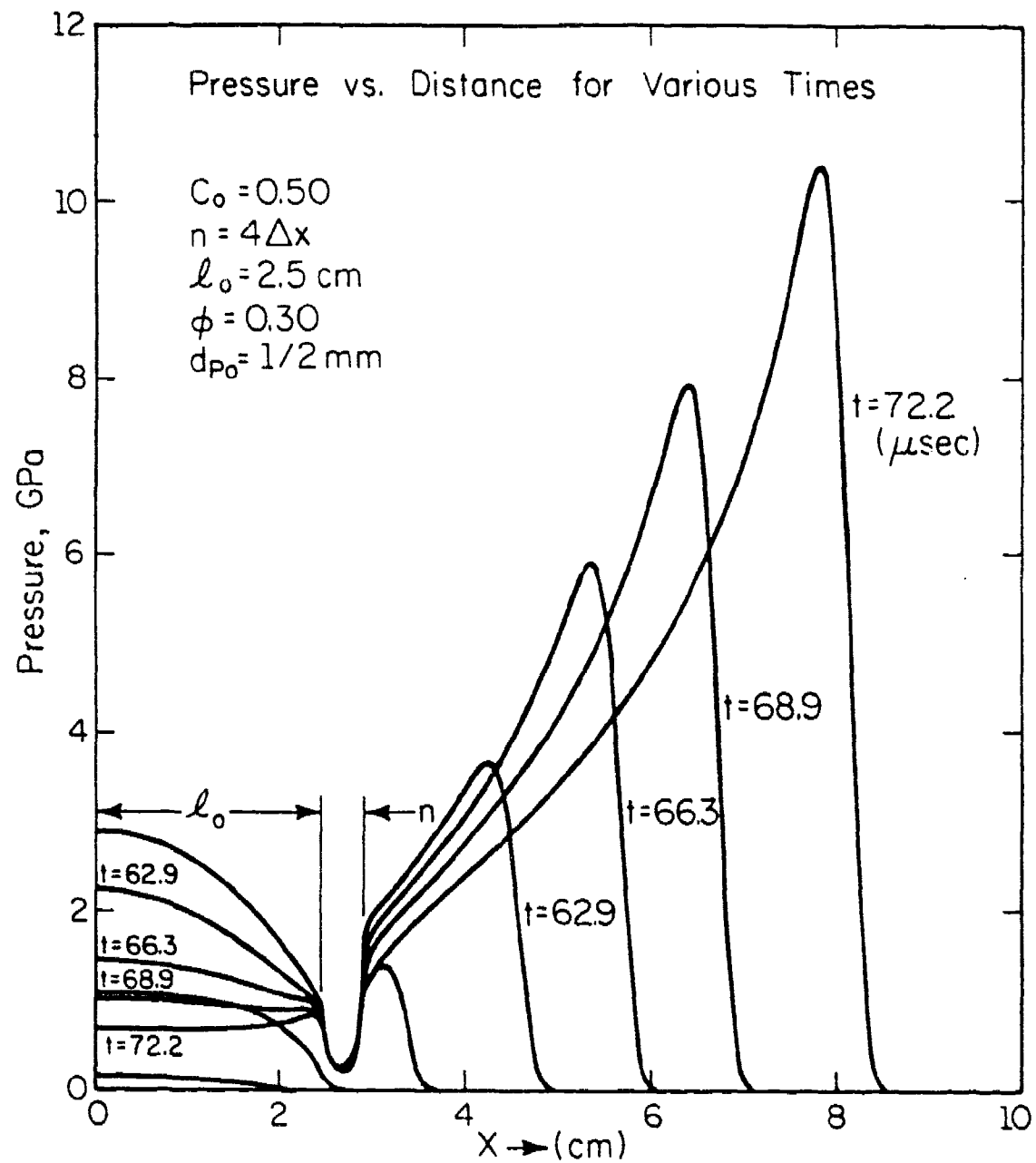
Figure 5. Pressure History Showing Effect of Hole in Casing
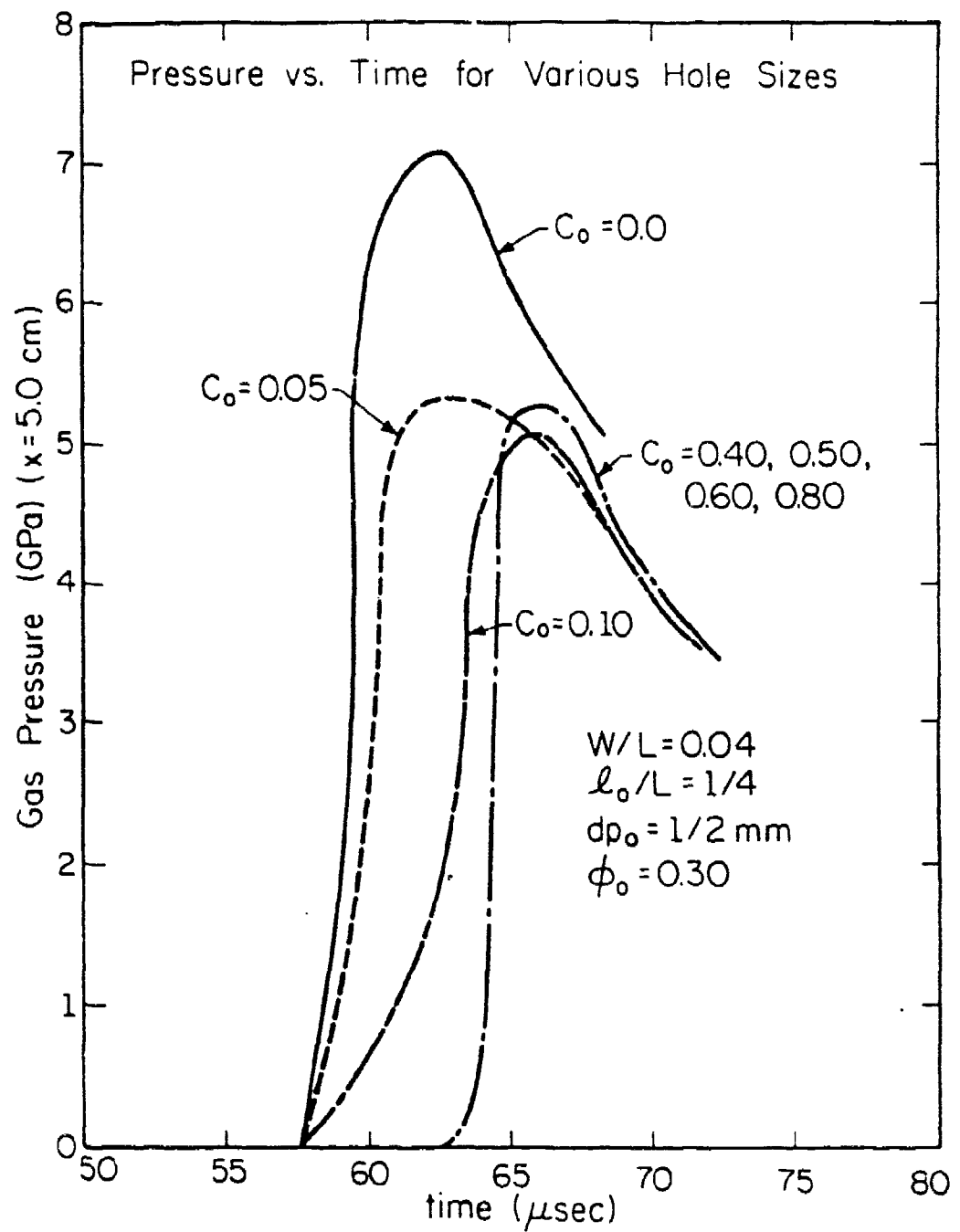
Figure 6. Comparison of Pressure Profiles at Bed Midpoint for Various Sized Cracks
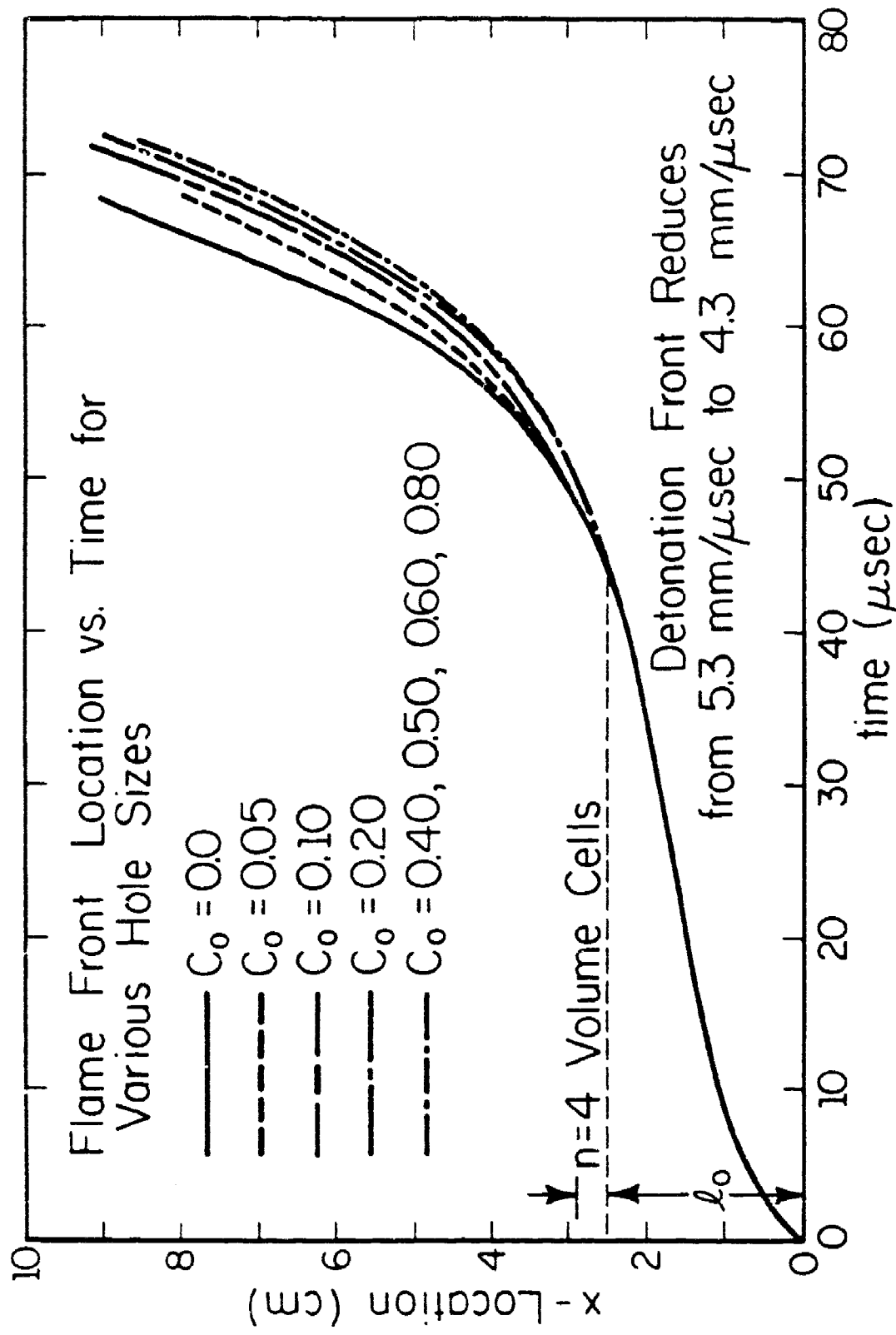
Figure 7. Locus of Flame Front for Various Crack Values of C_o
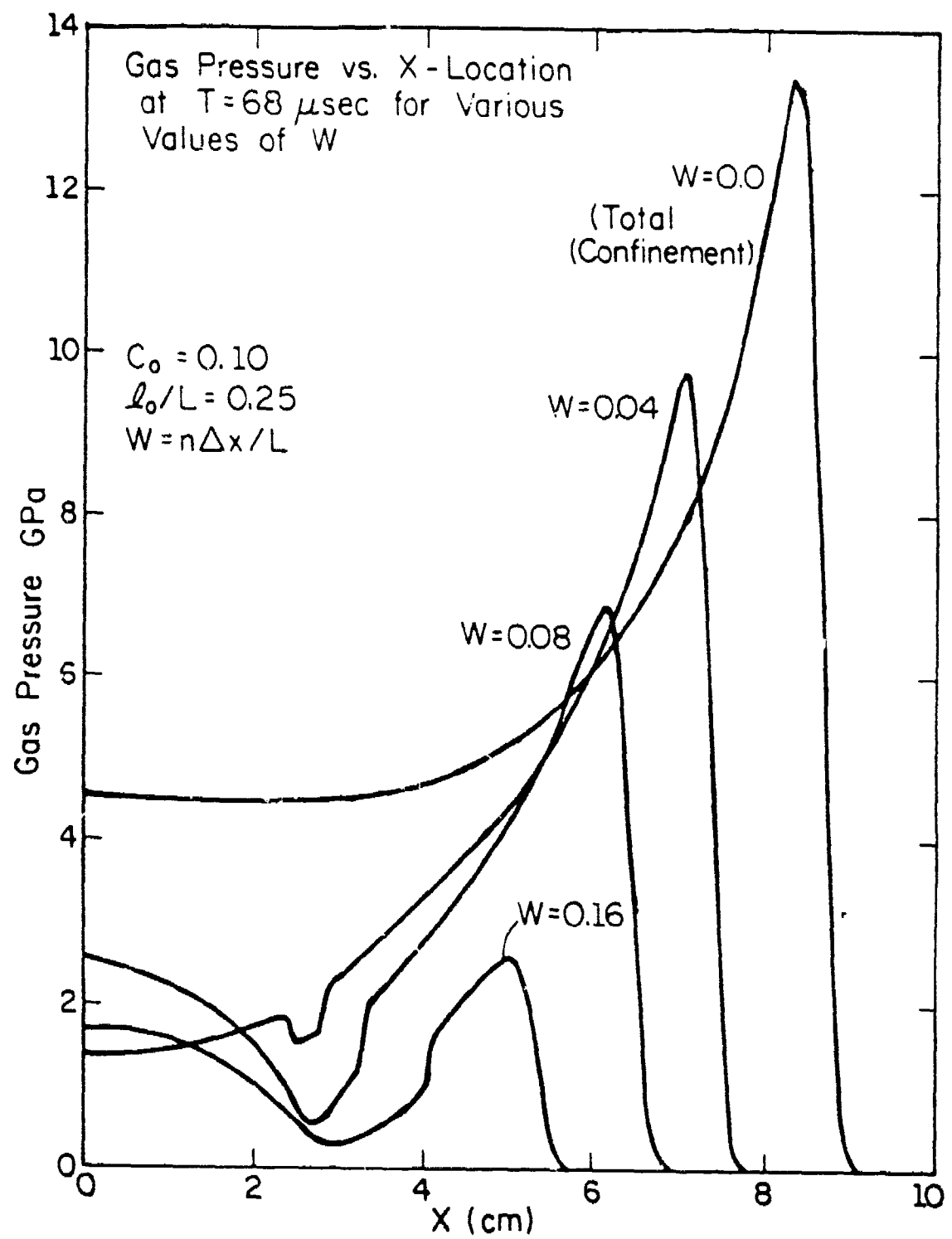
Figure 8. Comparison of Pressure Histories for Cracks of
Various Lengths
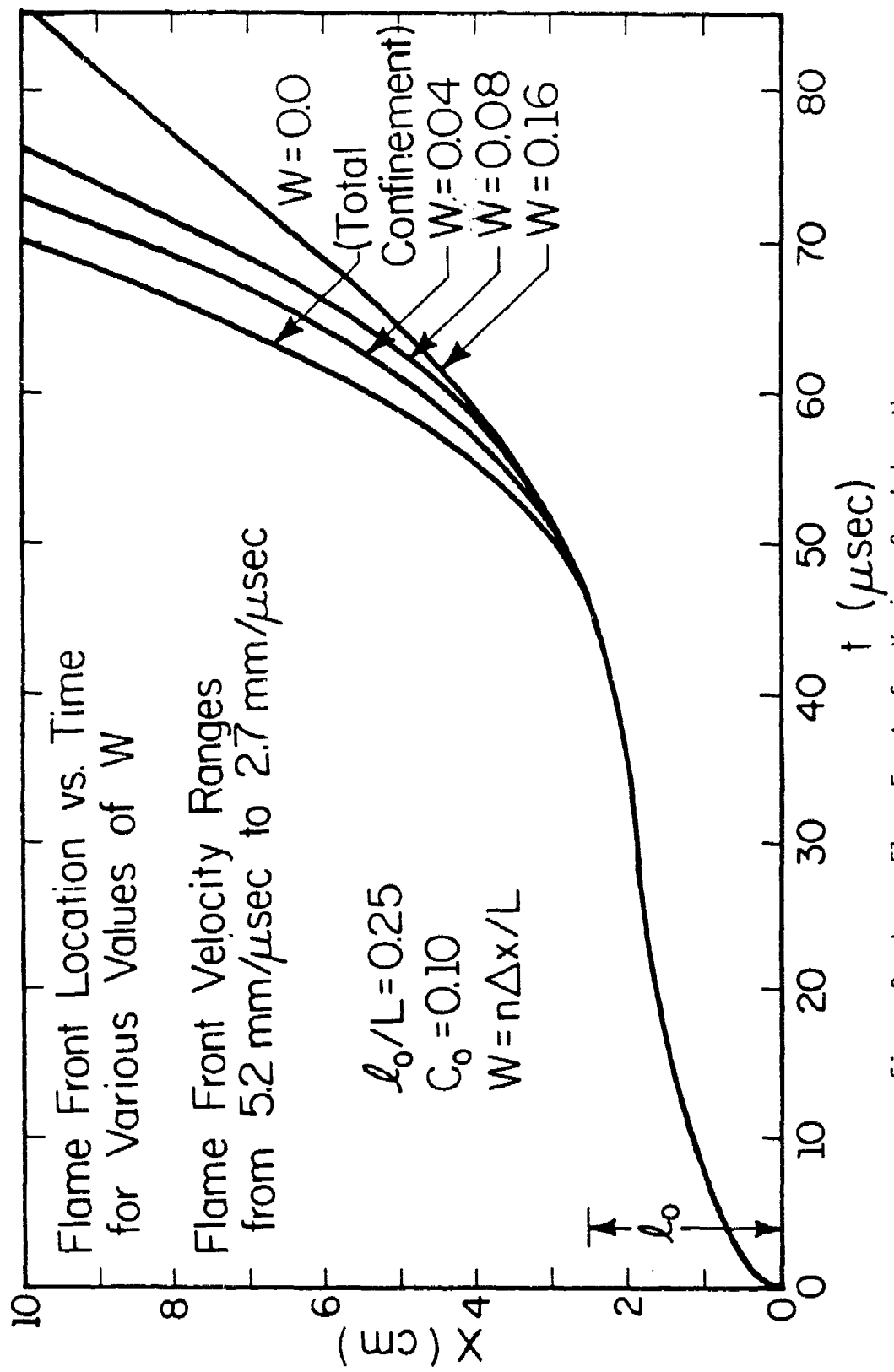
Figure 9. Locus Flame Fronts for Various Crack Lengths

26

Pressure History for Ruptured
Bed Showing Recovery Downstream of Hole
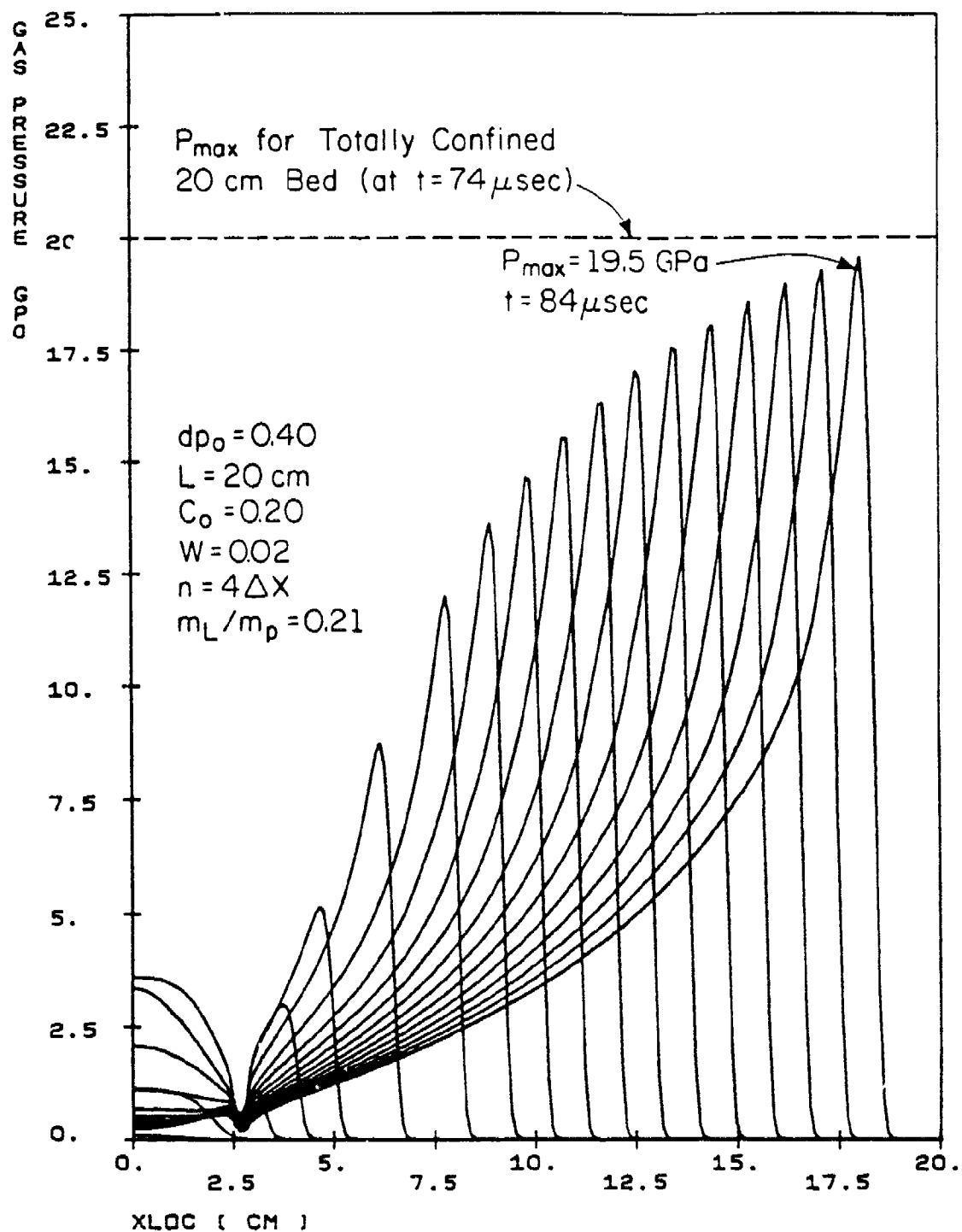
Figure 10.   Pressure History for Extended Bed, Showing
Pressure Recovery Downstream of Hole
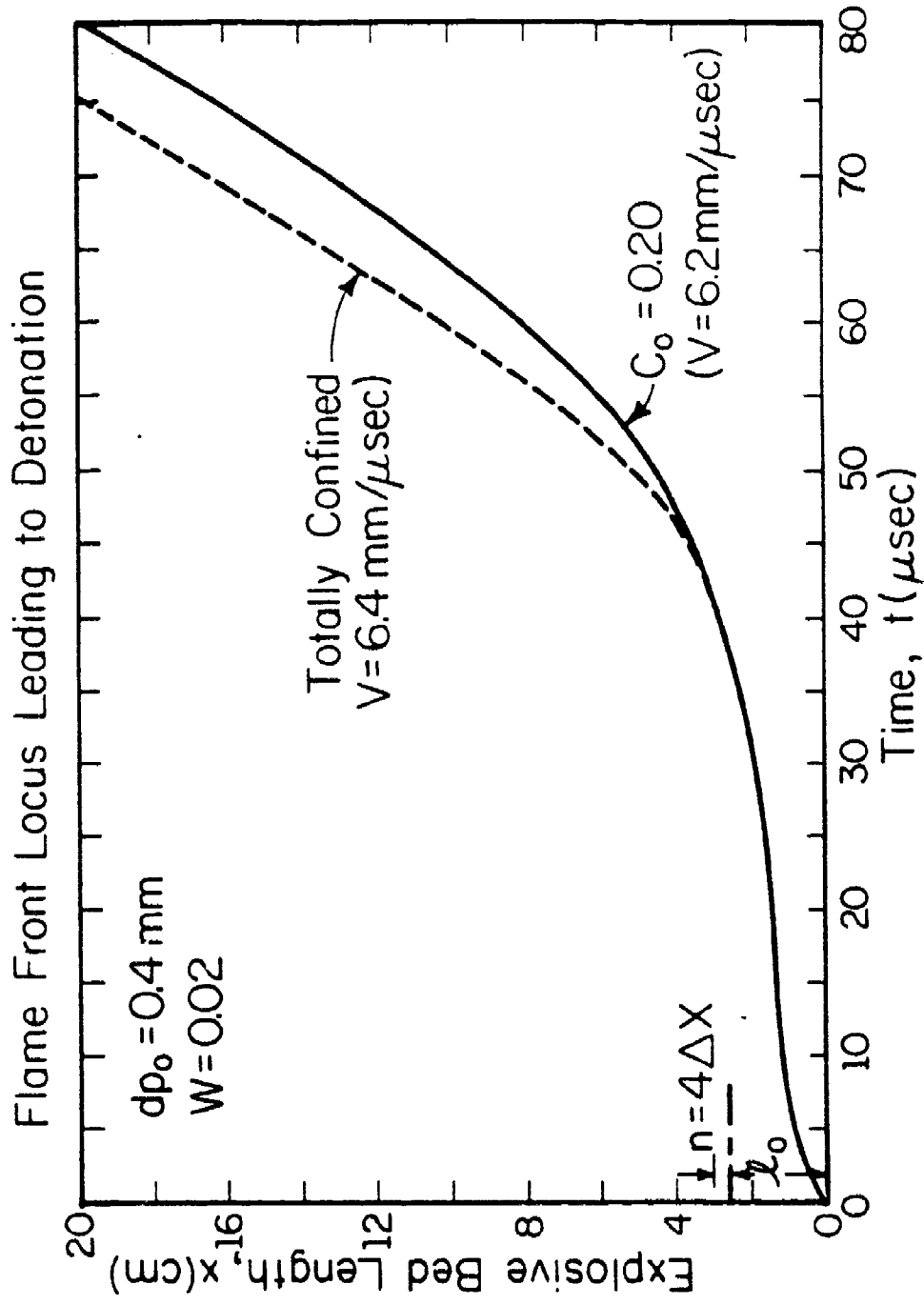
Figure 11.   Flame Front Locus for Extended Bed, Showing Flame Front
Recovery Downstream of Hole
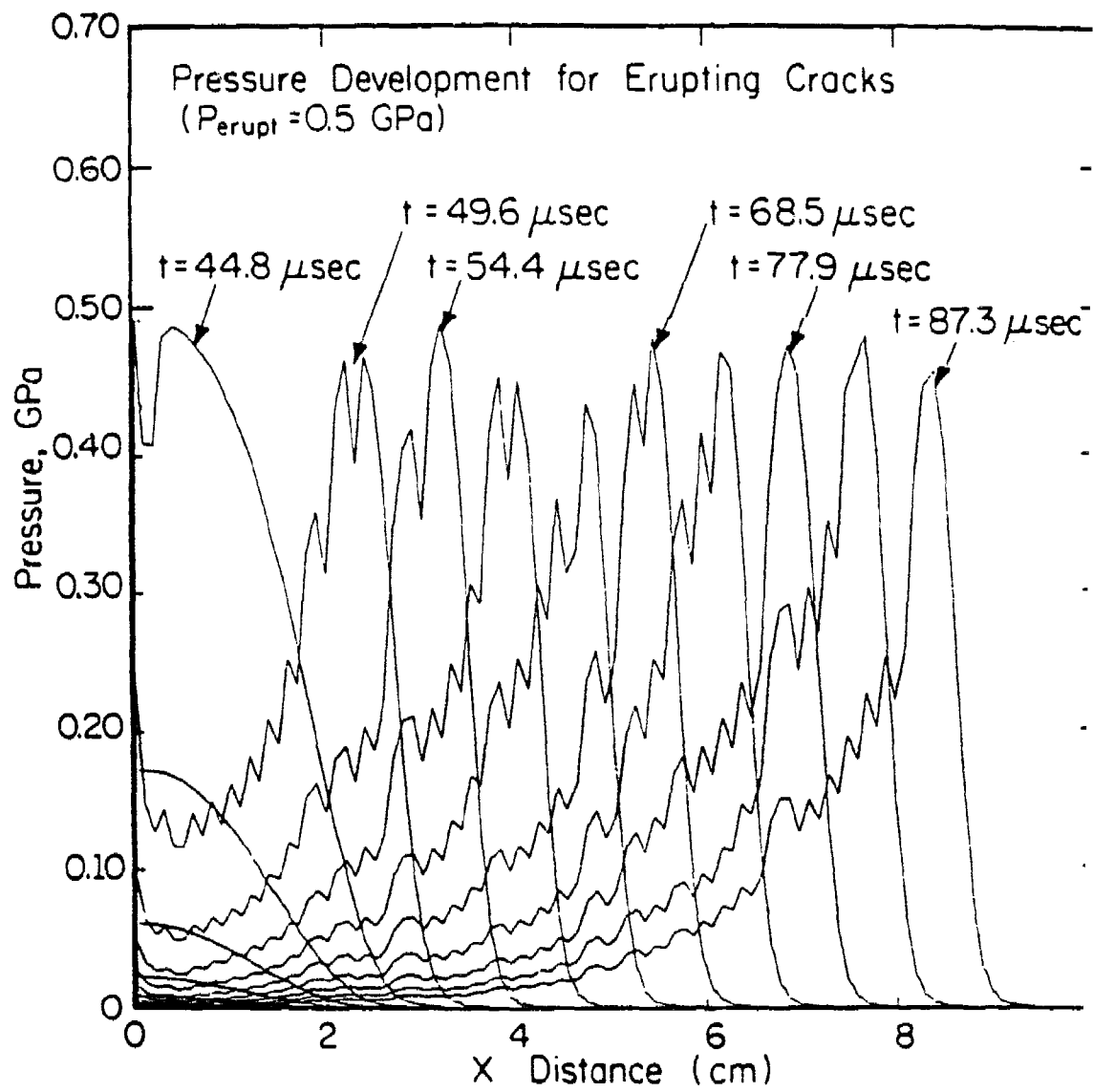
Figure 12. Pressure History for Erupting Cracks

29
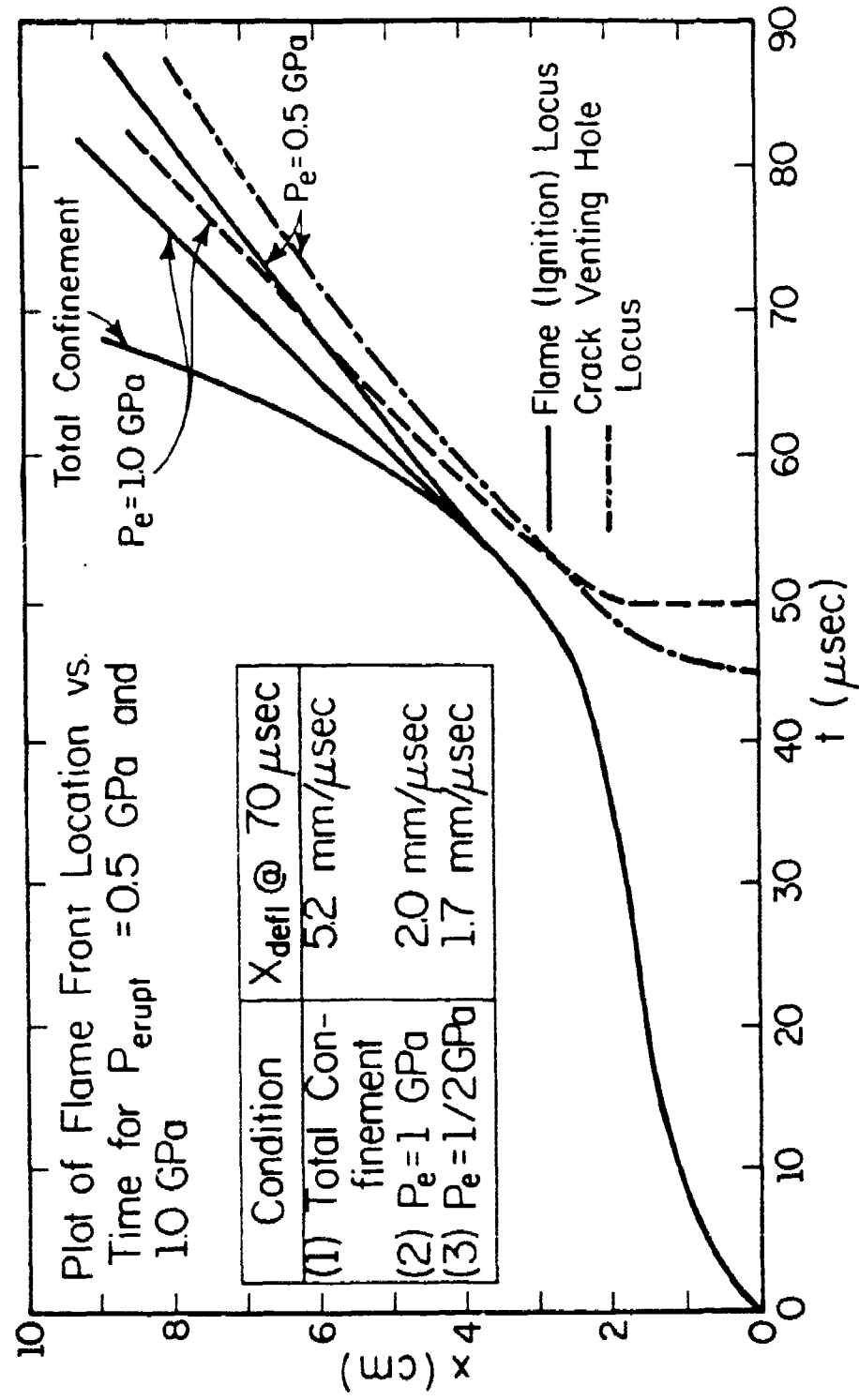
Figure 13. Flame Front Locus for Erupting Cracks for Two Different Critical Pressures (locus of cracks is also shown)

30

SECTION III

THE THREE DIMENSIONAL MODEL

1. INTRODUCTION

In References 1-8, the separated flow approach was used to derive the conservation equations for an unsteady, two-phase reactive system in one space dimension. In this section, the same type of analysis is followed to derive the conservation equations for a three-dimensional domain in order to properly model the dynamic flow processes in partially contained regions. Each phase will be considered as a separate fluid flowing through its own control volume, the sum of the two volumes being equal to the average mixture volume. The conservation equations are then expressed in cylindrical coordinates with interphase mass, momentum and energy transfer terms being included in all three independent directions.

Before work was started on this phase of the project, a thorough search of the fluid-mechanics literature was made. While the search was quite exhaustive, very little work on transient flows was found which could be of help to the analysis of this problem. However, a paper by Markatos and Kirkcaldy (Reference 13), was found in which a numerical model based on a separated flow analysis was used to investigate the transient, three-dimensional reactive flow through the totally confined granulated solid propellant inside a gun cartridge. While this paper did not present sufficient details, it did provide a useful example which allowed us to compare the unsteady, three-dimensional conservation equations derived in this work with those derived independently by other authors.

31

2. ASSUMPTIONS

All of the assumptions stated in Section II, paragraph 2, also apply for the three-dimensional case, with the obvious exceptions of assumptions (b) and (e), which refer to the one-dimensional nature of the equations. It will still be assumed that the gas escaping from the domain through the crack in the wall will leave at the choked velocity. However, the pseudo one-dimensional sink term (β) used to approximate the lost mass, momentum, and energy will not apply here. Instead the choked assumption will comprise the boundary condition at the location of the crack, and the amount of mass, momentum, and energy lost will be found directly from the solution of the conservation equations.

3. THE UNSTEADY, THREE-DIMENSIONAL CONSERVATION EQUATIONS

The unsteady conservation equations are presented below in their complete form. A detailed derivation of these equations, based on the separated flow concept is presented in Appendix C. The gas and particle phase momentum equations in the $\vec{r}$, $\vec{\theta}$ and $\vec{z}$ - direction are presented in generic form for brevity, with Table 3 giving the specific terms for each phase and direction.

The conservation equations are:

Gas Phase Continuity

$$\frac{\partial \rho_1}{\partial t} = - \frac{1}{r} \frac{\partial}{\partial r} (r \rho_1 u_g) - \frac{1}{r} \frac{\partial}{\partial \theta} (\rho_1 v_g) - \frac{\partial}{\partial z} (\rho_1 w_g) + \Gamma \qquad (16)$$

Solid Phase Continuity

32

$$\frac{\partial \rho_2}{\partial t} = -\frac{1}{r}\frac{\partial}{\partial r}(r\rho_2 u_p) - \frac{1}{r}\frac{\partial}{\partial \theta}(\rho_2 v_p) - \frac{\partial}{\partial z}(\rho_2 w_p) - \Gamma \qquad (17)$$

Gas Phase Momenta (3-equations)

$$\frac{\partial(\rho_1\phi_1)}{\partial t} = -\frac{1}{r}\frac{\partial}{\partial r}(r\rho_1 u_g\phi_1) - \frac{1}{r}\frac{\partial}{\partial \theta}(\rho_1 v_g\phi_1) - \frac{\partial}{\partial z}(\rho_1 w_g\phi_1) + S_{\phi_1}$$

Solid Phase Momenta (3-equations)

$$\frac{\partial(\rho_2\phi_2)}{\partial t} = -\frac{1}{r}\frac{\partial}{\partial r}(r\rho_2 u_p\phi_2) - \frac{1}{r}\frac{\partial}{\partial \theta}(\rho_2 v_p\phi_2) - \frac{\partial}{\partial z}(\rho_2 w_p\phi_2) + S_{\phi_2}$$

where ϕ_1 stands for u_g, v_g, or w_g, respectively and ϕ_2 stands for u_p, v_p, or w_p. The terms S_{ϕ_1} and S_{ϕ_2} represent the gas and solid phase source terms, respectively.

TABLE 3. SOURCE TERMS FOR MOMEMTUM EQUATIONS

$$\phi_1 \qquad\qquad\qquad S_{\phi_1}$$

$$u_g \qquad \frac{\rho_1 v_g^2}{r} - \frac{\partial P_1}{\partial r} - D_r + \Gamma u_p \qquad\qquad (18)$$

$$v_g \qquad -\frac{\rho_1 v_g u_g}{r} - \frac{1}{r}\frac{\partial P_1}{\partial \theta} - D_\theta + \Gamma v_p \qquad\qquad (19)$$

$$w_g \qquad -\frac{\partial P_1}{\partial z} - D_z + \Gamma w_p \qquad\qquad (20)$$

$$\phi_2 \qquad\qquad\qquad S_{\phi_2}$$

$$u_p \qquad \frac{\rho_2 v_p^2}{r} - \frac{\partial P_2}{\partial r} + D_r - \Gamma u_p \qquad\qquad (21)$$

$$v_p \qquad -\frac{\rho_2 v_p u_p}{r} - \frac{1}{r}\frac{\partial P_2}{\partial \theta} + D_\theta - \Gamma v_p \qquad\qquad (22)$$

$$w_p \qquad -\frac{\partial P_2}{\partial z} + D_z - \Gamma w_p \qquad\qquad (23)$$

In Equations (18)-(20)

$$P_1 = P_g \phi$$

and in Equations (21)-(23)

$$P_2 = P_p (1-\phi)$$

34

Gas Phase Energy

$$\frac{\partial(\rho_1 E_{gt})}{\partial t} = -\frac{1}{r}\frac{\partial}{\partial r}(r\rho_1 u_g E_{gt} + r\phi u_g P_g) -$$

$$\frac{1}{r}\frac{\partial}{\partial \theta}(\rho_1 v_g E_{gt} + \phi v_g P_g) - \frac{\partial}{\partial z}(\rho_1 w_g E_{gt} + \phi w_g P_g)$$

$$- D_r u_p - D_\theta v_p - D_z w_p - \dot{Q}$$

$$+ r(E^g_{chem} + u_p^2/2 + v_p^2/2 + w_p^2/2) \qquad (24)$$

Solid Phase Energy

$$\frac{\partial(\rho_2 E_{pt})}{\partial t} = -\frac{1}{r}\frac{\partial}{\partial r}(r\rho_2 u_p E_{pt} + r(1-\phi)u_p P_p) -$$

$$\frac{1}{r}\frac{\partial}{\partial \theta}(\rho_2 v_p E_{pt} + (1-\phi)v_p P_p)$$

$$- \frac{\partial}{\partial z}(\rho_2 w_p E_{pt} + (1-\phi)w_p P_p) + D_r u_p$$

$$+ D_\theta v_p + D_z w_p + \dot{Q} + r(E^p_{chem} - u_p^2/2 - v_p^2/2 - w_p^2/2)$$

$$(25)$$

In order to completely describe our system at every instant of time, we need to know the instantaneous values of ρ_g, ρ_p, u_g, u_p, v_g, v_p, w_g, w_p, T_g, T_p, P_g, P_p, and ϕ - - - thirteen variables. Equations (16)-(25) allow us to solve for ten of these variables. We therefore need three additional relations to achieve closure. These equations are:

35

(i)   an equation of state for the gas phase

(ii) an equation of state for the solid phase

(iii) a material stress-porosity relation

The same relations used in the analysis described in Section II (and further described in Appendix A) will be used here as well. Furthermore, the same relations for the gas mass generation Γ and the heat transfer rate $\dot{Q}$, as used in Section II will be used here. The definition of the drag viscous interaction will be assumed to hold true in each direction independently, i.e.,

$$D_r \equiv \frac{\mu_g}{4r_p^2} (u_g - u_p) f_{pg} \quad .$$

(26)

$$D_\theta \equiv \frac{\mu_g}{4r_p^2} (v_g - v_p) f_{pg}$$

(27)

$$D_z \equiv \frac{\mu_g}{4r_p^2} (w_g - w_p) f_{pg}$$

(28)

$$D_{total} \equiv \left[D_r^2 + D_\theta^2 + D_z^2 \right]^{\frac{1}{2}}$$

(29)

In comparing Equations (16)-(25) to the one-dimensional conservation equations (Equations (1)-(6) in Section II), one can see that the main differences (other than the obvious additional terms that account for the

multi-dimensional nature of the new equations) are the addition of the $\frac{\rho_1 u_g^2}{r}$ term in the r-direction momentum equations and the $\frac{\rho_1 u_g v_g}{r}$ term in the θ-direction momentum equations. These terms are the radial acceleration and the Coriolis acceleration terms, respectively, and come from the fact that $\frac{\partial \vec{r}}{\partial \theta} \neq 0$ and $\frac{\partial \vec{\theta}}{\partial \theta} \neq 0$ in a curvilinear coordinate system. [Here, $\vec{r}$ is the unit vector in the radial direction and $\vec{\theta}$ is the unit vector in the azimuthal direction.]

Also on the inspection of Equations (18)-(23) we note that the pressure gradient terms are now written as the gradient of partial pressure (i.e. $\frac{\partial(P\phi)}{\partial r}$) rather than the gradient of pressure (i.e. $\phi\frac{\partial P}{\partial r}$), as is sometimes found in the literature (Reference 13). The specific form of this term has been a subject of debate among fluid dynamicists working in multi-phase flows. We feel that the correct form should be $\frac{\partial(P\phi)}{\partial r}$, since the term represents the pressure <u>force</u> acting on the control volume faces. Since we are considering each phase separately, we should include only the pressure acting on that area of the control volume face which is occupied by the gas phase. Hence, the porosity ϕ (gas volume/total volume) must be included inside the derivative. Naturally, the same reasoning holds true for the solid phase. Therefore, the term (1-ϕ) must be included inside the derivative of the solid phase pressure gradient term.

4. DOMAIN

The first approximation to the actual geometry of current warhead containers would be to model the bomb as a right circular cylinder, as is shown in Figure 14. The figure shows the assumed crack in the outer casing as well as the fragmented explosive inside. To be able to model realistic crack

37

configurations one would have to include the entire 360° cross section of the cylinder in the domain of the model. However, one of the difficulties in tackling this problem is the large amount of computer time and memory which would be required to simulate such cracking. Therefore, in an effort to reduce the size of the domain, it was decided to assume a certain amount of symmetry in setting up this problem. This can be done by assuming that the damage to the casing occurs in such a manner that holes form in a symmetric ring around the casing, as is shown in Figure 15. This subdivides the domain of the cylindrical bomb into symmetric wedges, the flow in each wedge being identical to the flow in all the other wedges. The flow inside the bomb may then be completely described by solving the flow inside a single wedge.

Although such a domain limits the realism of this problem from a geometry standpoint, this assumption still retains the necessary multi-dimensional features of the transient fluid analysis. Also, it is not currently within the scope of this work to analyze the dynamics of the casing fracture, but rather to develop a model of the transient, two-phase reactive fluid mechanics involved in the processes of detonation transition or failure. Clearly the model developed herein, under this specific symmetry assumption, can be extended by simply adjusting the boundary conditions in the θ -direction to include the full domain, once a super-computer with sufficient speed is available.

5. BOUNDARY CONDITIONS AND INITIAL CONDITIONS

Once the domain of the model has been fixed, boundary conditions must be properly specified. The symmetric domain shown in Figure 15 has six boundaries: solid walls at $r = R$, $z = 0$, and $z = L$, and symmetry boundaries

38

at $r = 0$, $\theta = \theta_1$ and $\theta = \theta_2$. Obviously, at each solid wall the normal velocity component must be zero. In addition, symmetry allows us to say that the radial velocity components u_g and u_p must be zero at $r = 0$, and all derivatives with respect to r must also be zero here. Symmetry also implies that v_g and v_p must be zero at θ_1 and θ_2 and that all derivatives with respect to θ must be zero at these two boundaries.

As mentioned in the introduction to this chapter, the velocity at the location of the crack will be assumed to be choked. This assumption forms the last boundary condition needed to solve the finite difference equations. How these boundary conditions are incorporated into the finite difference model is discussed in detail in Section IV, paragraph 4.

The bed of explosive particles is assumed to be initially quiescent and at a prescribed nominal temperature and pressure. Combustion is initiated at time $t = 0$ by assuming that a hot burning zone exists at one end of the domain, with the temperature in this zone enough above the explosive ignition temperature to ignite the particles. The initial value input is given in Section V.

39

3 - DIMENSIONAL MODEL

OPENING

W

$Z=Z_c$

CUT-AWAY VIEW
SHOWING
PARTICLE SIZE
DISTRIBUTION
IN (r, θ, z)

FUSE IGNITED
IN CENTRAL CORE

CLOSED
END

u

v

w

ℓ

40
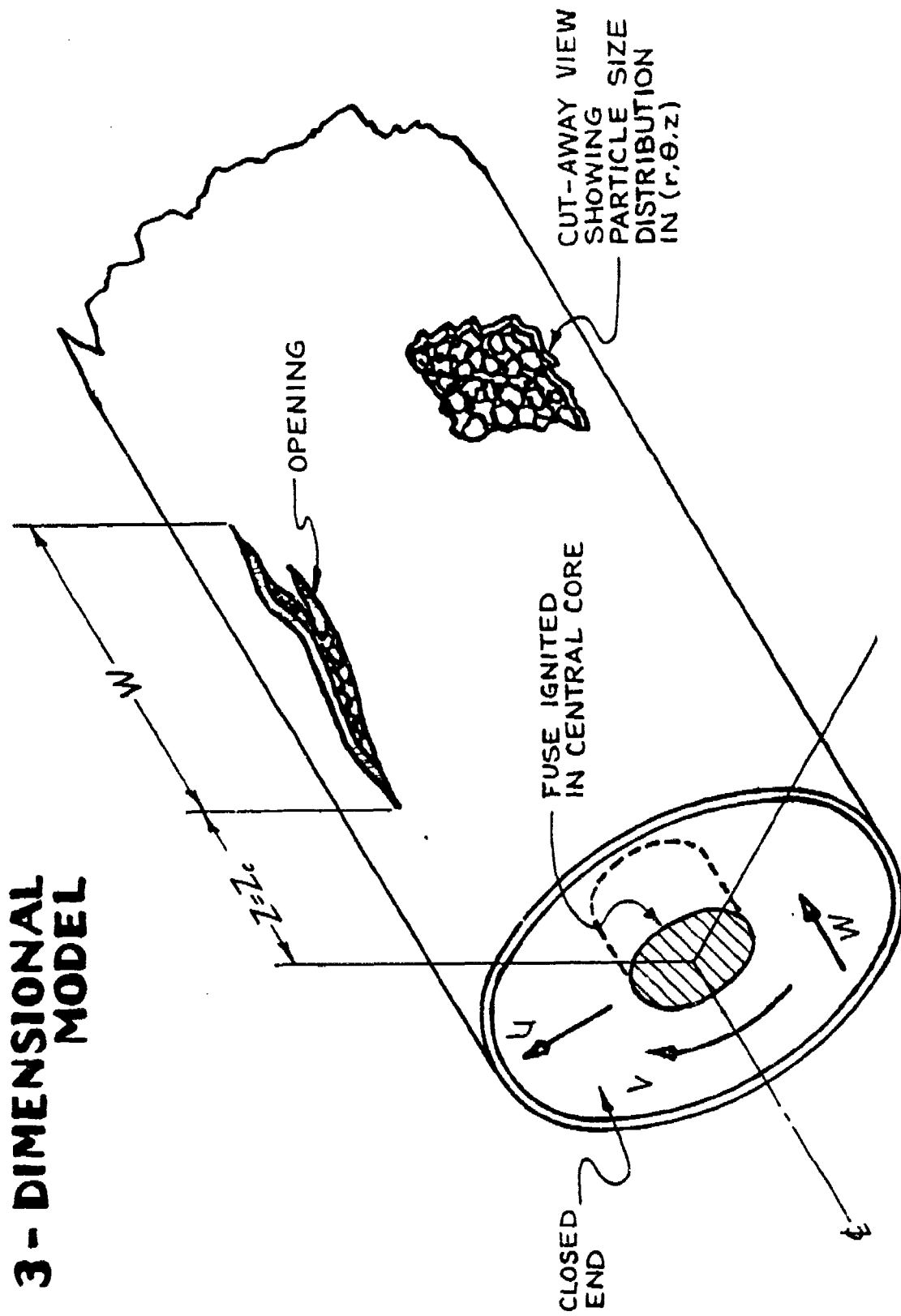
Figure 14.   Schematic of Three-Dimensional Domain Showing Crack in the Casing

3-DIMENSIONAL
WEDGE MODEL
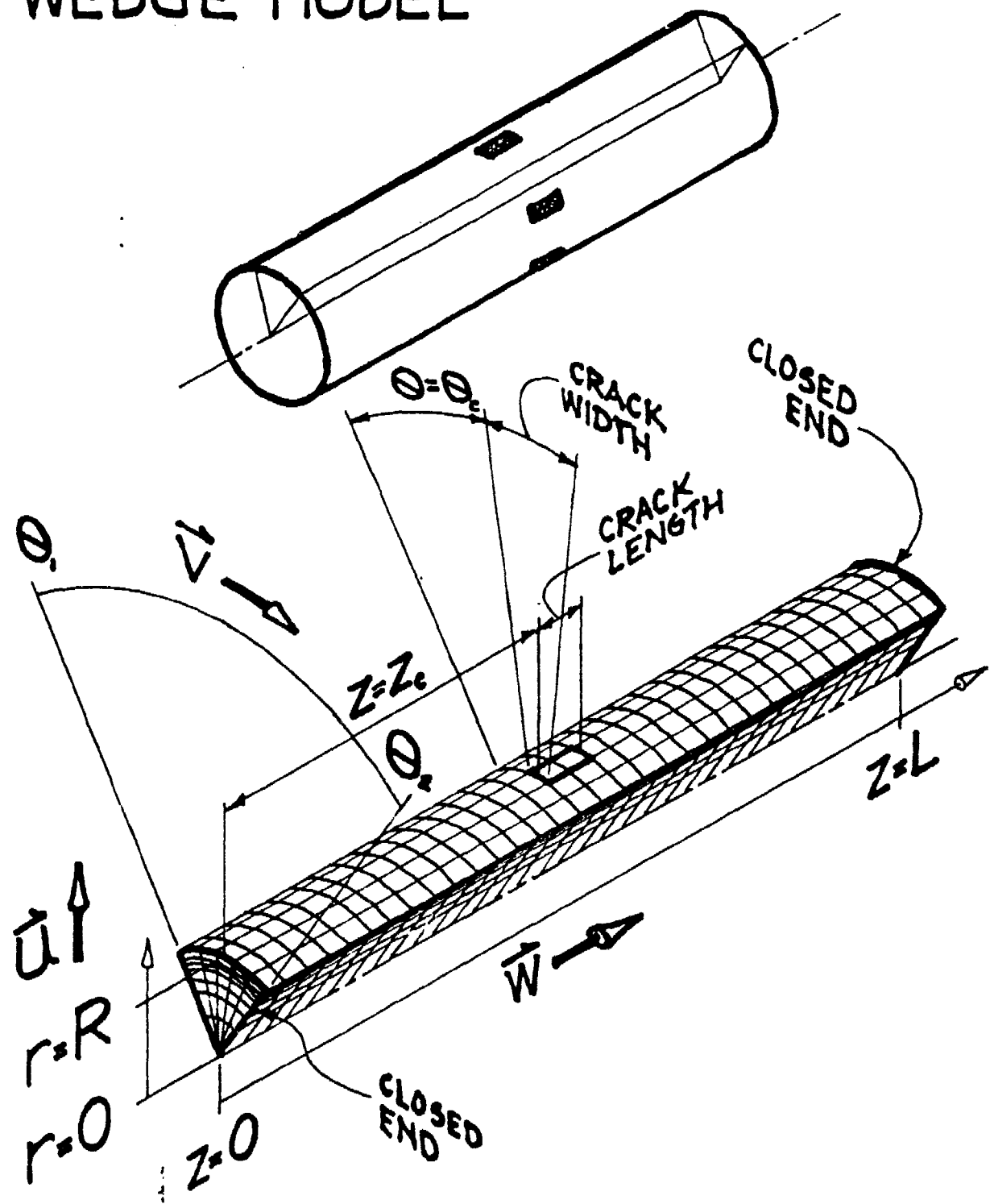
Figure 15.   Schematic of Three-Dimensional Domain
with Symmetric Cracking

41

SECTION IV

THE FINITE DIFFERENCE EQUATIONS

1. INTRODUCTION

The unsteady two-phase conservation equations presented in Section III form a set of coupled, non-linear, hyperbolic partial differential equations. As was the case in the pseudo two-dimensional formulation presented in Section II, these equations also will not have analytical solutions. Futhermore, a Method of Lines (MOL) approach such as the one used in solving the one-dimensional equations would not be feasible for the three-dimensional case due to the great increase in the size of the domain. The high-order ODE solvers used in the Method of Lines require a large number of calculations to be performed when solving the unsteady terms in the conservation equations. Therefore, while such an approach may be feasible for the domain of the one-dimensional case, it would prove to be cost prohibitive for the much larger three-dimensional domain. Instead, a new integration method was developed as part of this research.

In this section, we will detail the development of a new numerical scheme which will be used to integrate Equations (16)-(25). The discretization of the domain into a mesh of grid points is discussed in paragraph 2, while the actual finite difference scheme is discussed in paragraph 3. Paragraph 4 details the finite differencing of the boundary conditions. Finally, stability considerations for the finite difference scheme are discussed in paragraph 5.

2. THE FINITE DIFFERENCE GRID

In applying a finite difference method to the solution of any system of equations, the continuous domain of the problem must be replaced by a mesh of grid nodes, each node representing a location where the values of certain dependent variables are stored. In this analysis, a staggered grid was used to represent the domain. Figure 16 shows a single cylindrical, three-dimensional control volume element employing the staggered grid. All scalar variables are stored in the node at the center of the control volume, while the bulk momentums in the $\vec{r}$ -direction ($\rho_1 u_g$ and $\rho_2 u_p$) are stored at each of the nodes in the $\vec{r}$ -faces of the control volume, the bulk momentum in the $\vec{\theta}$ - direction ($\rho_1 v_g$ and $\rho_2 v_p$) are stored at each of the nodes in the $\vec{\theta}$ -faces, and the bulk momentums in the $\vec{z}$ -direction ($\rho_1 w_g$ and $\rho_2 w_p$) are stored at each of the nodes in the $\vec{z}$ -faces.

There are several reasons why it is advantageous to use the staggered grid instead of the conventional grid. First, as will be shown in paragraph 4, it makes the finite differencing of the boundary conditions considerably easier. It also enables one to get second-order accurate centered space differences while having to span only half the distance required for taking such a difference on a conventional grid. The advantage of this can be illustrated by the following one-dimensional example. Consider the two grids shown in the Figure 17. The upper grid is a conventional grid, while the staggered grid is shown below that.

Now assume one wishes to evaluate the pressure gradient term in the momentum equation. On the conventional grid, this term is evaluated by second order centered difference as:

$$\frac{\partial P}{\partial x} \approx (P_{i+1} - P_{i-1})/2\Delta x$$

If we apply this equation at node i=2, we get for our example,

$$\frac{\partial P}{\partial x} \approx (100-100)/2\Delta x = 0$$

This obviously cannot be true given the pressure field depicted in the figure.

If we now evaluate this finite difference on the staggered grid, we only need to take the difference over a total step of Δx (rather than $2\Delta x$ as before), since values of P_g are available at nodes that are a distance of $\Delta x/2$ and $-\Delta x/2$ from the velocity node (where the momentum equation will be evaluated). Thus at i=2,

$$\frac{\partial P_g}{\partial x} \approx (P_{i+\frac{1}{2}} - P_{i-\frac{1}{2}})/\Delta x$$

or $$\frac{\partial P_g}{\partial x} \approx (100-50)/\Delta x = 50/\Delta x$$

As one can see, the scheme using the staggered grid yields a much more accurate result for this typical example.

Figure 18 shows the r, θ -plane and r, z-plane projections of our wedge-shaped domain with the staggered grid superimposed over it. The continuity equation (Equations (16) and (17)), which are used to solve for ρ_1 and ρ_2 , and the energy equations (Equations (24) and (25)), which are used to solve for E_{gt} and E_{pt}, will be solved at the scalar nodes (denoted by the symbol + in Figure 18) since these are scalar quantities. The $\vec{r}$ -momentum equations (Equations (18) and (19)) will be solved at the $\vec{r}$ -momentum nodes (denoted by the symbol   ), the $\vec{\theta}$ -momentum equations (Equations (20) and (21)) will be solved at the $\vec{\theta}$ -momentum nodes (denoted by the symbol   ), and the $\vec{z}$ -momentum equations (Equations (22) and (23)) will be solved at the $\vec{z}$ -momentum nodes (denoted by the symbol   ).

When employing the staggered grid, the situation may arise where the value of a variable is needed at a location where it is not defined. In this case a simple average will be taken to find the value at the desired point. For example, suppose one needs to know the value of the velocity, u, at the scalar node i=1 shown in the one-dimensional depiction (Figure 19). Since the u values are not stored at i=1, we must average the values stored at i= ½ and i=1 ½, together, to form $\bar{u}_{i=1}$. Thus

$$\bar{u}_i = (u_{i+\frac{1}{2}} + u_{i-\frac{1}{2}})/2$$

Although the necessity for such averaging may complicate the numerical scheme somewhat, it is actually advantageous as far as the accuracy of the calculations is concerned. The averaged value is influenced by the value of the variable at two nodes, while the variable which is read directly from a location where its value is known is influenced only by a single value. In

45

other words, the averaging operation passes information about gradients as well as providing the value needed.

Finally, one will note that in our scheme, momentum rather than velocity is stored at the nodes located in the control volume faces. This was done mainly to reduce the amount of computer storage required for the code.

3. THE FINITE DIFFERENCE EQUATIONS

Once the domain has been discretized, we must next cast the continuous conservation equations (16)-(25) into finite difference form. We will basically be using the leapfrog scheme Reference 14, which means that the unsteady term will be evaluated at time levels $t + \Delta t$ and $t - \Delta t$, while the flux and source/sink terms on the right hand sides of equations (16)-(25) will be evaluated at the current time, t.

The leapfrog scheme was chosen after we reviewed a paper by Williams (Reference 15) in which he successfully used the leapfrog scheme to integrate the unsteady three-dimensional conservation equations for an incompressible, single-phase viscous fluid. The similarity between the equations integrated in Williams paper and the equations handled in this work prompted us to consider a leapfrog-type scheme. While the compressible, two-phase reactive nature of the flow dealt with in this paper resulted in some major differences between the numerical scheme developed by Williams and the scheme developed herein, the usefulness of the work done in Reference 15 in aiding us in our analysis is still acknowledged.

Consider the following shorthand notation (where x is a generalized independent variable and q is a generalized dependent variable):

46

$$\delta_x q \equiv \left[q\ (x+\Delta x/2) - q\ (x-\Delta x/2) \right]/\Delta x \tag{30}$$

$$\overline{q}^x \equiv \left[q\ (x+\Delta x/2) + q\ (x-\Delta x/2) \right]/2 \tag{31}$$

Equation (30) is a difference operator while Equation (31) defines an averaging operator. Furthermore, let us define

$m_{r_1} \equiv \rho_1 u_g$ - gas bulk momentum in the $\vec{r}$-direction

$m_{r_2} \equiv \rho_2 u_p$ - particle bulk momentum in the $\vec{r}$-direction

$m_{\theta_1} \equiv \rho_1 v_g$ - gas bulk momentum in the $\vec{\theta}$-direction

$m_{\theta_2} \equiv \rho_2 v_p$ - particle bulk momentum in the $\vec{\theta}$-direction

$m_{z_1} \equiv \rho_1 w_g$ - gas bulk momentum in the $\vec{z}$-direction

$m_{z_2} \equiv \rho_2 w_p$ - particle bulk momentum in the $\vec{z}$-direction

We can then write Equations (16)-(25) based on our staggered grid in finite difference form as:

Gas Continuity (applied at scalar nodes)

$$\delta_t \overline{\rho_1}^t = -\frac{1}{r} \delta_r (m_{r_1} r) - \frac{1}{r} \delta_\theta (m_{\theta_1}) - \delta_z (m_{z_1}) + \Gamma \tag{32}$$

47

Particle Continuity (applied at scalar nodes)

$$\delta_t \overline{\rho}_2^t = - \frac{1}{r} \delta_r(m_{r_2} r) - \frac{1}{r} \delta_\theta(m_{\theta_2}) - \delta_z(m_{z_2}) - \Gamma \qquad (33)$$

Gas $\vec{r}$ -Direction Momentum (applied at $\vec{r}$ -momentum nodes)

$$\delta_t \overline{m}_{r_1}^t = - \frac{1}{r} \delta_r[r(\overline{m}_{r_1}^r)^2/\rho_1] - \frac{1}{r} \delta_\theta [(\overline{m}_{r_1}^\theta \overline{(m_{\theta_1}/\rho_1^\theta)}^r]$$

$$- \delta_z[\overline{m}_{r_1}^z \overline{(m_{z_1}/\rho_1^z)}^r + (m_{r_1})^2/(\overline{\rho}_1^r r)$$

$$- \delta_r(P_1) - \overline{D}^r (m_{r_1}/\overline{\rho}_1^r - m_{r_2}/\overline{\rho}_2^r)$$

$$+ \overline{\Gamma}^r m_{r_2}/\overline{\rho}_2^r \qquad (34)$$

Particle $\vec{r}$ -Direction Momentum (applied at $\vec{r}$ -momentum nodes)

$$\delta_t \overline{m}_{r_2}^t = - \frac{1}{r} \delta_r[r(\overline{m}_{r_2}^r)^2/\overline{\rho}_2] - \frac{1}{r} \delta_\theta[\overline{m}_{r_2}^\theta \overline{(m_{\theta_2}/\overline{\rho}_2^\theta)}^r]$$

$$- \delta_z[\overline{m}_{r_2}^z \overline{(m_{z_2}/\overline{\rho}_2^z)}^r] + (m_{r_2})^2/(\overline{\rho}_2^r r)$$

$$- \delta_r(P_2) + \overline{D}^r (m_{r_1}/\overline{\rho}_1^r - m_{r_2}/\overline{\rho}_2^r)$$

$$- \overline{\Gamma}^r m_{r_2}/\overline{\rho}_2^r \qquad (35)$$

Gas $\vec{\theta}$ -Direction Momentum (applied at $\vec{\theta}$ -momentum node)

48

$$\delta_t \overline{m}_{\theta_1}^t = -\frac{1}{r}\,\delta_r\big[r\overline{m}_{\theta_1}^\theta\,\overline{(m_{r_1}/\overline{\rho}_1^r)}^r\big] - \frac{1}{r}\,\delta_\theta\big[(\overline{m}_{\theta_1}^\theta)^2/\rho_1\big]$$

$$- \delta_z\big[\overline{m}_{\theta_1}^z\,\overline{(m_{z_1}/\overline{\rho}_1^z)}^\theta\big] - m_{\theta_1}\overline{\overline{(m_{r_1}/\overline{\rho}_1^r r)}}^\theta$$

$$- \frac{1}{r}\,\delta_\theta(P_1) - D\,(m_{\theta_1}/\overline{\rho}_1^\theta - m_{\theta_2}/\overline{\rho}_2^\theta)$$

$$+ \overline{\Gamma}^\theta\,m_{\theta_2}/\overline{\rho}_2^\theta \tag{36}$$

Particle $\vec{\theta}$ -Direction Momentum (applied at $\vec{\theta}$ -momentum nodes)

$$\delta_t \overline{m}_{\theta_2}^t = -\frac{1}{r}\,\delta_r\big[r\overline{m}_{\theta_2}^\theta\,\overline{(m_{r_2}/\overline{\rho}_2^r)}^r\big] - \frac{1}{r}\,\delta_\theta\big[(\overline{m}_{\theta_2}^\theta)^2/\rho_2\big]$$

$$- \delta_z\big[\overline{m}_{\theta_2}^z\,\overline{(m_{z_2}/\overline{\rho}_2^z)}^\theta\big] - m_{\theta_2}\overline{\overline{(m_{r_2}/\overline{\rho}_2^r r)}}^\theta$$

$$- \frac{1}{r}\,\delta_\theta(P_2) + \overline{D}^\theta\,(m_{\theta_1}/\overline{\rho}_1^\theta - m_{\theta_2}/\overline{\rho}_2^\theta)$$

$$- \overline{\Gamma}^\theta m_{\theta_2}/\overline{\rho}_2^\theta \tag{37}$$

Gas $\vec{Z}$ -Direction Momentum (applied at $\vec{Z}$ -momentum nodes)

$$\delta_t \overline{m}_{z_1}^t = -\frac{1}{r}\,\delta_r\big[r\overline{m}_{z_1}^r\,\overline{(m_{r_1}/\overline{\rho}_1^r)}^z\big] - \frac{1}{r}\,\delta_\theta\big[\overline{m}_{z_1}^\theta\,\overline{(m_{\theta_1}/\overline{\rho}_1^\theta)}^z\big]$$

49

$$- \delta_z\left[(\overline{m}_{z_1}^z)^2/\rho_1\right] - \delta_z(P_1) -$$

$$\overline{D}^z(m_{z_1}/\overline{\rho}_1^z - m_{z_2}/\overline{\rho}_2^z) + \overline{r}^z m_{z_2}/\overline{\rho}_2^z \tag{38}$$

Particle $\dot{z}$ -Direction Momentum (applied at $\dot{z}$ -momentum nodes)

$$\delta_t \overline{m}_{z_2}^t = -\frac{1}{r}\,\delta_r\left[r\overline{m}_{z_2}^r \overline{(m_{r_2}/\rho_2)}^z\right] - \frac{1}{r}\,\delta_\theta\left[\overline{m}_{z_2}^\theta \overline{(m_{\theta_2}/\rho_2)}^z\right]$$

$$- \delta_z\left[(\overline{m}_{z_2}^z)^2/\rho_2\right] - \delta_z(P_2)$$

$$- \overline{D}^z(m_{z_1}/\overline{\rho}_1^z - m_{z_2}/\overline{\rho}_2^z) - \overline{r}^z m_{z_2}/\overline{\rho}_2^z \tag{39}$$

Gas Energy (applied at scalar nodes)

$$\delta_t \overline{E}_1^t = -\frac{1}{r}\,\delta_r\left\{rm_{r_1}\left[\overline{E_1/\rho_1}^r + \overline{(P_1/\rho_1)}^r\right]\right\}$$

$$-\frac{1}{r}\,\delta_\theta\left\{m_{\theta_1}\left[\overline{E_1/\rho_1}^\theta + \overline{(P_1/\rho_1)}^\theta\right]\right\}$$

$$-\delta_z\left\{m_{z_1}\left[\overline{E_1/\rho_1}^z + \overline{(P_1/\rho_1)}^z\right]\right\}$$

$$-\dot{Q} - D\,\overline{m}_{r_2}^r/\rho_2 - D\,\overline{m}_{\theta_2}^\theta/\rho_2$$

$$- D\,\overline{m}_{z_2}^z/\rho_2 + r\left[E_{chem}^g + (\overline{m}_{r_2}^r/\rho_2)^2/2\right.$$

$$+\left.(m_{\theta_2}/\rho_2)\,/2 + (m_{z_2}/\rho_2)\,/2\right] \tag{40}$$

50

<u>Particle Energy</u>   (applied at scalar nodes)

$$\delta_t \overline{E}_2^t = -\frac{1}{r}\,\delta_r \left\{ r m_{r_2}\left[\overline{E_2/\rho_2}^{\,r} + (\overline{P_2/\rho_2})^r\right]\right\}$$

$$-\frac{1}{r}\,\delta_\theta \left\{ m_{\theta_2}\left[\overline{E_2/\rho_2}^{\,\theta} + (\overline{P_2/\rho_2})^\theta\right]\right\}$$

$$-\delta_z \left\{ m_{z_2}\left[\overline{E_2/\rho_2}^{\,z} + (\overline{P_2/\rho_2})^z\right]\right\}$$

$$+\dot{Q} + D\,\overline{m}_{r_2}^r/\rho_2 + D\,\overline{m}_{\theta_2}^\theta/\rho_2$$

$$+ D\,\overline{m}_{z_2}^z/\rho_2 + r\left[E_{chem}^p - (\overline{m}_{r_2}^r/\rho_2)^2/2\right.$$

$$\left. - (m_{\theta_2}/\rho_2)\,/2 - (m_{z_2}/\rho_2)\,/2\right] \tag{41}$$

In these equations,

$$D = (\mu_g/4r_p^2)\cdot f_{pg}$$

4. THE BOUNDARY CONDITIONS

Once the domain has been discretized and an integration scheme has been devised, we must next turn to implementing the boundary conditions. As mentioned earlier, there are six different boundaries where the equations must be satisfied. We will consider each boundary separately.

(1)   r = R

Here we have a solid wall, which means that the normal velocity components (u_g and u_p) must be zero. Figure 18 shows that at this boundary, we have only $\vec{r}$ -momentum nodes. Since only the $\vec{r}$ -momentum equations are evaluated at these nodes, this boundary condition can easily be met by initializing the value of the $\vec{r}$ -momentum variables stored at these nodes to zero and ordering the code to skip calculating the change in the $\vec{r}$ -momentum (i.e. skip evaluating Equations (34) and (35)) when r = R. This will cause the values of the $\vec{r}$ -momentum to remain at zero, thus satisfying the boundary condition.

One must also be able to evaluate Equations (32), (33) and (36)-(41) at nodes which are not directly on the boundary, but are a distance of $\Delta r/2$ in from the wall at r = R. The evaluation of these equations at these particular nodes is affected by the wall boundary in the evaluation of the $\vec{r}$ -direction flux term (i.e. the first term on the right hand side in Equations (32)-(41)).

The problem and its solution are perhaps best described by an example. Consider attempting to evaluate the $\vec{r}$ -flux term in Equation (40) (i.e. $\delta_r \{ m_{r_1} r [(\overline{E_1/\rho_1}^r) + (\overline{P_1/\rho_1}^r)] \}$) at the scalar node adjacent to the boundary at r = R as shown in Figure 20. Evaluating the flux term as described by Equation (30), we can see that we must find the values of E_1/ρ_1 and P_1/ρ_1 at $i + \frac{1}{2}$ and $i - \frac{1}{2}$. However, since E_1, ρ_1, and P_1 are all scalar quantities, their values are not known at these points and must therefore be found by interpolation as the averaging operators in the flux term indicate. This creates an apparent problem when one tries to average the values at (i) and (i+1) to get the value at (i+$\frac{1}{2}$), since (i+1) lies outside the domain.

52

However, one will note that the quantity $(E_1/\rho_1 + P_1/\rho_1)$ is always multiplied by the momentum in the $\vec{r}$-direction to find the flux, and since the $\vec{r}$-momentum at the wall at $r = R$ is always zero, these variables can have any finite values at $(i+1)$. Once the average has been taken and the result multiplied by the $\vec{r}$-momentum at $(i+\frac{1}{2})$(which is, of course, zero), the flux through the wall in the $\vec{r}$-direction will have the correct value of zero. This is why these nodes are refered to as false exterior nodes. They lie outside the domain and are initialized to some arbitrary value, at which they remain throughout the run. They are used purely to fulfill the requirements of the numerical method and the griding scheme.

(2) $r = 0$

The symmetry boundary conditions requires that u_p and u_g must be equal to zero at $r = 0$ and that all derivatives with respect to r must be equal to zero. Again, we can note from Figure 21 shown below that there are only $\vec{r}$-momentum nodes at $r = 0$. The first boundary condition is again met by initializing the values of the gas and particle phase momenta at these nodes to zero and instructing the code to skip solving the $\vec{r}$-momentum equations whenever $r = 0$. Note that this procedure also avoids the singularity that occurs in the $1/r$ terms as $r \to 0$. Since we have only $\vec{r}$-momentum nodes at $r=0$, and since the code skips solving these equations at that point, the singularity never arises.

The symmetry condition can be met by using reflection points about the z-axis at $r=0$, and continuously updating the values of the variables stored at these nodes to match the nodes directly across the z-axis. However, referring to Figure 21, we can see that again the only interaction between the equations evaluated at nodes which are a distance of $\Delta r/2$ from the boundary at $r=0$ and

53

the symmetry boundary at r=0 is in the $\vec{r}$ -direction flux term, just as in paragraph 1. Performing the same analysis which we performed in paragraph (1), we again see that the values of the variables at these symmetry nodes can be completely arbitrary. Once the averaging is performed and the result is multiplied by the $\vec{r}$ -momentum (which is, of course, zero), the flux through the boundary at r=0 will have its proper value of zero. It is therefore not strictly necessary that the values at the reflection points be continuously updated to enforce the symmetry condition, although it would be perfectly proper to do so. Note that the only reason that this is possible is because we are using a staggered grid and our equations have no space derivatives higher than first order.

(3) z = 0 (solid wall)

Here we again have a solid wall, leading to the boundary condition that the velocity components w_g and w_p must be zero. This boundary condition is imposed in the same manner that the boundary conditions on the radial velocity components u_g and u_p were imposed in paragraph (1). Again false exterior nodes are used to facilitate the numerical scheme at the nodes which are at a distance of $\Delta z/2$ from the boundary. Figure 22 shows the details.

(4) z = L (far wall)

The same boundary conditions that applied in (3) apply here

(5) $\theta = \theta_1$ (wedge symmetry)

Here we again utilize symmetry with the boundary condition being that tangential velocity components, v_g and v_p at these nodes are zero. This condition is enforced in the same manner that the symmetry condition in

54

paragraph (2) is enforced.   (See Figure 23 for details.)

(6) $\theta = \theta_2$ (wedge symmetry)

The same conditions that applied in paragraph (5) apply here.

Open vent (r = R)

Finally, we must consider the boundary conditions at r = R at the location of the prescribed holes in the outer wall. Since the fluid and particle momentum at the wall in this case will no longer be zero, the scheme which was devised in paragraph (1) will not apply. Instead, we will have to use one-sided interpolations to determine the necessary values at r = R.

As stated before, the gas will be assumed to be leaving the hole at the choked gas velocity, which is a function of the local pressure and temperature below the hole. Choked flow means that the gas velocity is equal to the local sound speed. The speed of sound in the non-ideal gas we are using here, as is derived in Appendix B, is given by:

$$a = [\frac{C_{v_g} (1+2b_1\rho_g) + R (1+b_1\rho_g^2)}{C_{v_g}\rho_g(1+b_1\rho_g)} P_g]^{\frac{1}{2}} \qquad (B.9)$$

In addition to the speed of sound, it will be necessary to know the value of several other variables of the fluid at the wall. These may be found via a Taylor Series expansion about the node nearest the wall. Referring to Figure 24, the general dependant variable W defined at location (i) may be approximated at $(i+\frac{1}{2})$ as:

55

$$W_{i+\frac{1}{2}} \approx W_i + \frac{\Delta r}{2} \frac{\partial W}{\partial r} \Big|_i \tag{42}$$

Since we are adjacent to the wall, the derivative $\frac{\partial W}{\partial r}$ cannot be approximated as a centered second-order finite difference. Instead, we can write this term as a one-sided second order finite difference:

$$\frac{\partial W}{\partial r} \Big|_i \approx \frac{3W_i - 4W_{i-1} + W_{i-2}}{2\Delta r} \tag{43}$$

Therefore, our approximation becomes

$$W_{i+\frac{1}{2}} \approx \frac{7W_i - 4W_{i-1} + W_{i-2}}{4} \tag{44}$$

If the hole is assumed to be larger than one node in the $\vec{r}$- or $\vec{\theta}$-direction, it is assumed that the velocity at the node at the center of the hole is choked, and that the velocities at the remaining hole nodes constitute a linear profile so that the u velocity is zero at the edge of the hole. (See Figure 25)

The velocity of the particles leaving the domain through the hole is evaluated by calculating the drag force on the particles at the hole location:

$$\frac{\partial(\rho_2 u_p)}{\partial t} \approx F_D \tag{45}$$

where $F_D = D_r(2\pi r_p^2)$

then

$$\partial(\rho_2 u_p) \approx F_D dt \tag{46}$$

56

Integrating both sides, we get:

$$\int_{t-\Delta t}^{t+\Delta t} d(\rho_2 u_p) = \int_{t-\Delta t}^{t+\Delta t} F_D dt \qquad (47)$$

Since we assume in our discretization that all properties remain constant over the time step Δt, $F_D \neq F_D(t)$. Then

$$\int_{t-\Delta t}^{t+\Delta t} d(\rho_2 u_p) = F_D \int_{t-\Delta t}^{t+\Delta t} dt \qquad (48)$$

or

$$(\rho_2 u_p)^{t+\Delta t} - (\rho_2 u_p)^{t-\Delta t} = F_D \cdot 2\Delta t \qquad (49)$$

and finally,

$$(\rho_2 u_p)^{t+\Delta t} = F_D \cdot 2\Delta t + (\rho_2 u_p)^{t-\Delta t} \qquad (50)$$

Once a value for the particle momentum at the hole is known, the rest of the terms needed for evaluating the numerical scheme can be found via the one-sided interpolation described above.

5. STABILITY

The numerical solution of partial differential equations by finite difference methods always presents a problem called stability. A finite difference scheme, while providing an accurate representation of the original analytic equation and boundary conditions, may still yield unsatisfactory results due to oscillations and explosive growth of the output caused by

57

instabilities inherent to the differencing scheme being used. Most textbooks on numerical methods treat this topic in great detail. In this section, we will look at several sources of instability inherent to the scheme presented in paragraph 3 and how they can be controlled.

In any explicit differencing scheme, there exists a bound on the maximum size of the time step. Our conservation equations can be shown to be hyperbolic partial differential equations. If the size of the time step exceeds this bound, oscillations will set in and the output will soon become unstable. This limiting value can be calculated via the Von Neumann approach (see, for instance, Richtmeyer and Morton, Reference 16). However, for the system of ten coupled, nonlinear equations with source terms which form our finite difference scheme, the evaluation of the Von Neumann stability criteria would in itself constitute a formidable task. It was therefore decided to defer calculating the optimum time step and simply run the model with a suitable constant time step, Δt, which must be determined by trial and error. Once the suitability of the scheme has been proven, then a concentrated effort can be made to determine the formula for the optimum allowable time step.

A second source of instability is caused by the fact that centered time differencing, rather than forward time differencing was used to represent the unsteady terms in Equations (16)-(25). Centered time differencing was chosen because Kurihara (Reference 14) has shown that it provides less damping of the kinetic energy than other methods of time differencing. The centered-time difference scheme can be represented as:

$$(W^{t+1} - W^{t-1})/2\Delta t = F\ (r,\theta,z)^t + S_\phi^t \tag{51}$$

where W is some generalized conserved quantity, $F(r,\theta,z)$ represents the flux terms and S_ϕ represents the source terms. Solving for W^{t+1}, we get

$$W^{t+1} = 2\Delta t \left[F(r,\theta,z)^t + S_\phi^{\ t} \right] + W^{t-1} \qquad (52)$$

Since the first term on the right-hand side is added to the value of W at time level t-1, there is a possibility that W at time level t+1 may be less than the value of W at time level t, even if $2\Delta t \left[F(r,\theta,z)^t + S_\phi^{\ t} \right]$ is a positive quantity. Once this occurs, the solution begins to oscillate until eventually separate solutions form at odd and even time steps.

This oscillation is controlled by adding in a step which averages the conserved variables over adjacent time steps, as was suggested by Williams (Reference 15). Thus, one writes

$$W^{*t-1} = (W^t + W^{t-1})/2 \qquad (53)$$

In this work, the variables were averaged at each adjacent time step to control this oscillation. It was therefore decided that a time step of 3/2 Δt rather than $2\Delta t$ should be used, since this averaging process effectively reduces the size of the time step. Thus, we assume

$$W^{t+1} = (3/2)\ \Delta t \cdot F(r,\theta,z)^t + W^{*t-1} \qquad (54)$$

To show the effect of this procedure it will be useful to consider one of the computational results. Figure 26 shows a comparison of the flame front locus versus time using time steps of 3/2Δt and 2Δt, respectively. This is

59

compared with the flame front history from the one-dimensional model described in Section II. In all cases the walls are impermeable. The three-dimensional calculation was in this case uniformly initiated to make the comparisons meaningful. As can be seen, the use of $3/2\Delta t$ as the time step yields results which are much closer to the results from the previous one-dimensional model, a result which is fairly accurate.

Another source of instability results from the nature of the equations being differentiated. Equations (16)-(25) represent a set of nonlinear, hyperbolic equations. The numerical integration of such equations can become unstable due to explosive growth of the total energy of the system. This instability is caused by aliasing, in which waves that are too short to be resolved by the grid are misinterpreted as waves of longer wavelength. Figure 27 illustrates this phenomenon.

The solid line in Figure 27 denotes the actual waveform. However, since this continuous wave has been discretized, the code senses only the amplitude at each node. It therefore incorrectly interprets the wave as having a waveform shown by the dashed line. Miyakoda (Reference 17) has shown that high frequency waves produced by convective terms in the governing equations can in this manner produce non-physical increases in the total energy of the system. However, Arakawa (Reference 18) has shown that if the convective terms in the total derivative form, as they are in Equations (32)-(41), aliasing will be controlled. The preceeding discussion on aliasing and its control is condensed from the paper by Williams (Reference 15) and the reader is referred there for further information on the subject. More on aliasing can be found in the notes by Wilhelmson (Reference 19).

Another common source of instability in the finite differencing of inviscid hyperbolic equations stems from the formation of shock waves in the

60

computational domain. The presence of a shock can cause near infinite gradients to occur at the front of the wave. These steep gradients quickly cause the governing equations to become unstable.

This type of instability is caused by the fact that the second derivative viscous terms, which are found in the complete Navier-Stokes equations, are not included in the pseudo-inviscid equations used here. The viscous nature of the real flow would tend to smear the shock discontinuity over a finite (albeit small) distance, thus decreasing the severity of the gradient across the front.

Control of this instability in an inviscid set of equations can be achieved by adding viscous-like artificial diffusion terms to the right hand side of Equations (32)-(41) which take the form of second derivatives. The text by Ames (Reference 20) presents sufficient background. These terms act to smooth out the sharp discontinuities which occur when a shock forms in the domain. The artificial viscosity term used in this work is similar to that used in Hyman's Predictor-Corrector Method described by Sod (Reference 21). For the explicit scheme used here, it was necessary to lag the evaluation of the artificial viscosity terms (i.e. evaluate them based on the values of the variables at the previous time step) to ensure stability (Wilhelmson, class notes Reference 19). Since no journal articles were found which described the application of artificial viscosity to three-dimensional problems, one-dimensional strategies were used in applying these diffusion terms to Equations (32)-(41). One-dimensional artificial viscosity terms were added to the equations where numerical experiments showed them to be necessary.

During the development of the computer code, it was found that the solutions to the momentum equations quickly became unstable unless an unacceptably small time step was used (typically 10^{-9} seconds). The root of

· 61

this instability was found to be in the interaction between the pressure gradient and drag terms. As the pressure front moves through undisturbed regions of the bed, the strong gradients across the front induce rapid increases in the gas velocity. The difference between the gas and particle velocities would then give rise to strong drag which acts to retard the motion of the gas. Realistically, the drag should continuously adjust itself as the relative velocity between the phases changes. However, since we have discretized this process, the model assumes that the drag remaining constant over the entire time step. If the drag is large enough, this assumption gives rise to the situation where the drag not only causes the flow to slow down, but actually reverses its direction. This is physically impossible, since once the relative velocity between the phases becomes zero, the drag would be zero and there would be no force to retard the flow any further and cause it to become negative.

Once the gas velocity becomes negative, the drag begins acting in the same direction as the pressure gradient, causing the velocity to again increase sharply, again becoming positive. This in turn again causes large drag values which cause the gas velocity to become negative. This oscillation between positive and negative velocities at adjacent time steps grows until the scheme becomes completely unstable.

This problem was solved by using a predictor/corrector strategy when evaluating the momentum equations (Equations (34)-(39)). For each direction (radial, azimenthal, and axial), the solid and gas phase momentum equations were solved exactly as shown in Equations (34)-(39), with all of the terms on the right-hand side being evaluated at the current time level, t. This predicted a temporary new value for the momenta at the next time level, t+1. These temporary values were then averaged with the current values of the gas

62

and solid phase momentum to give the average momentum over the time step, Δt. Next the average phase velocities over the time step were found by dividing out the appropriate phase density. Finally, the corrector step was performed by re-evaluating the momentum equation for each phase, again evaluating the right-hand side at the current time level (just as in the predictor step) except for the drag, which was evaluated based on the average phase velocities. The strategy in schematic form is, then:

$$(1) \quad (W_1)_{i,j,k}^{t+1*} = F_1(r,\theta,z)_{i,j,k}^{t} + S_{\phi_1}^{t} + (W_1)_{i,j,k}^{t-1} \qquad (55)$$

$$(W_2)_{i,j,k}^{t+1*} = F_2(r,\theta,z)_{i,j,k}^{t} + S_{\phi_2}^{t} + (W_2)_{i,j,k}^{t-1} \qquad (56)$$

$$(2) \quad (\overline{W}_1^{t})^{*}{}_{i,j,k} = [(W_1)_{i,j,k}^{t+1*} + (W_1)_{i,j,k}^{t}]/2 \qquad (57)$$

$$(\overline{W}_2^{t})^{*}{}_{i,j,k} = [(W_2)_{i,j,k}^{t+1*} + (W_2)_{i,j,k}^{t}]/2 \qquad (58)$$

$$(3) \quad (\overline{V}_1^{t})^{*}{}_{i,j,k} = (\overline{W}_1^{t})^{*}{}_{i,j,k} / \rho_1^{t} \qquad (59)$$

$$(\overline{V}_2^{t})^{*}{}_{i,j,k} = (\overline{W}_2^{t})^{*}{}_{i,j,k} / \rho_2^{t} \qquad (60)$$

$$(4) \quad (W_1)_{i,j,k}^{t+1} = F_1(r,\theta,z)_{i,j,k}^{t} + S_{\phi_1}'^{t} - D[(\overline{V}_1^{t})^{*}{}_{i,j,k} - (\overline{V}_2^{t})^{*}{}_{i,j,k}]$$

63

$$(W_2)_{i,j,k}^{t+1} = F_2(r,\theta,z)_{i,j,k}^t + S_{\phi_2}^{'t} + D \left[(\overline{V}_1^t)_{i,j,k}^\star - (\overline{V}_2^t)_{i,j,k}^\star \right]$$

(62)

Here W_1 and W_2 represent $\rho_1 u_g$ and $\rho_2 u_p$, $\rho_1 v_g$ and $\rho_2 v_p$, or $\rho_1 w_g$ and $\rho_2 w_p$, respectively. F_1 and F_2 represent the flux terms on the right-hand sides of the appropriate gas and solid phase momentum equations, respectively, while S_{ϕ_1} and S_{ϕ_2} represent the gas and solid phase source terms. S'_{ϕ_1} and S'_{ϕ_2} represent all the gas and particle phase source terms, except for the drag. Finally, $D = (\mu_g/4r_p^2) \, f_{pg}$ from the drag relation.

Figure 28 shows the improvement in stability caused by the use of the predictor/corrector strategy on the gas phase $\dot{z}$-momentum equation. The momentum is plotted for a single node versus number of integrations. Note that the kink at six integrations is caused by the particles at the adjacent node igniting and not by instability.

Typical 3-Dimensional Volume Cell
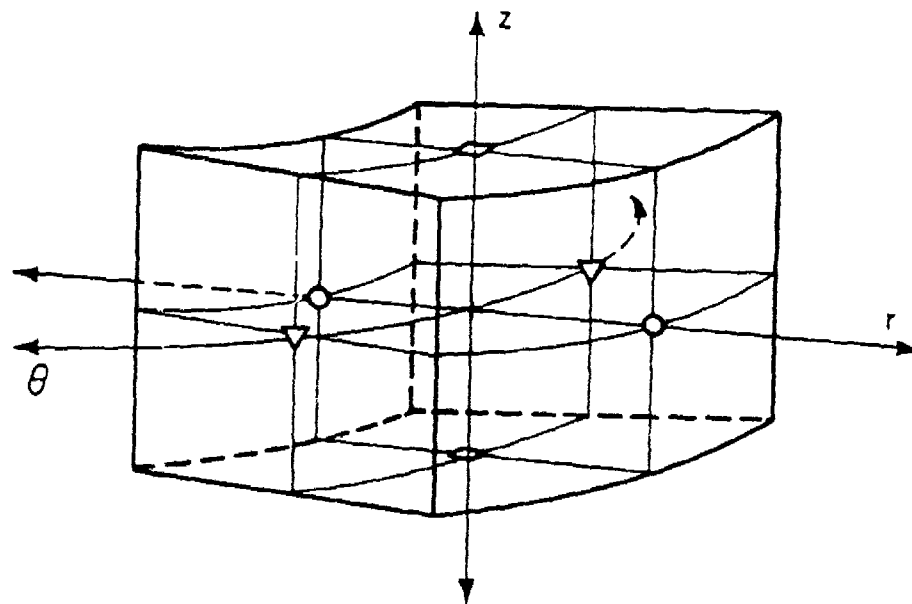
□ Axial Velocity ($\vec{w}$) Node

▽ Azimuthal Velocity ($\vec{v}$) Node

○ Radial Velocity ($\vec{u}$) Node

+ Pressure, Temperature, Density, Porosity Node

Figure 16. Single Three-Dimensional Volume Cell
Utilizing the Staggered Grid
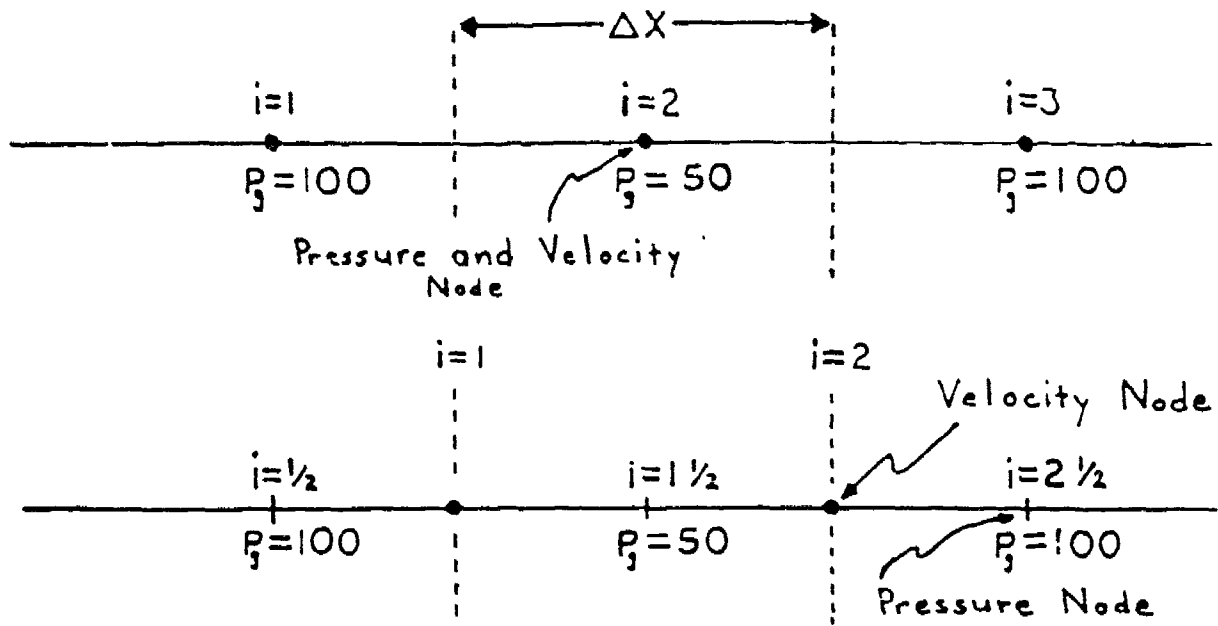
Figure 17. Comparison of Conventional and Staggered Grids

"false" exterior nodes

• – $\vec{r}$–momentum

▼ – $\vec{\theta}$–momentum

■ – $\vec{z}$–momentum
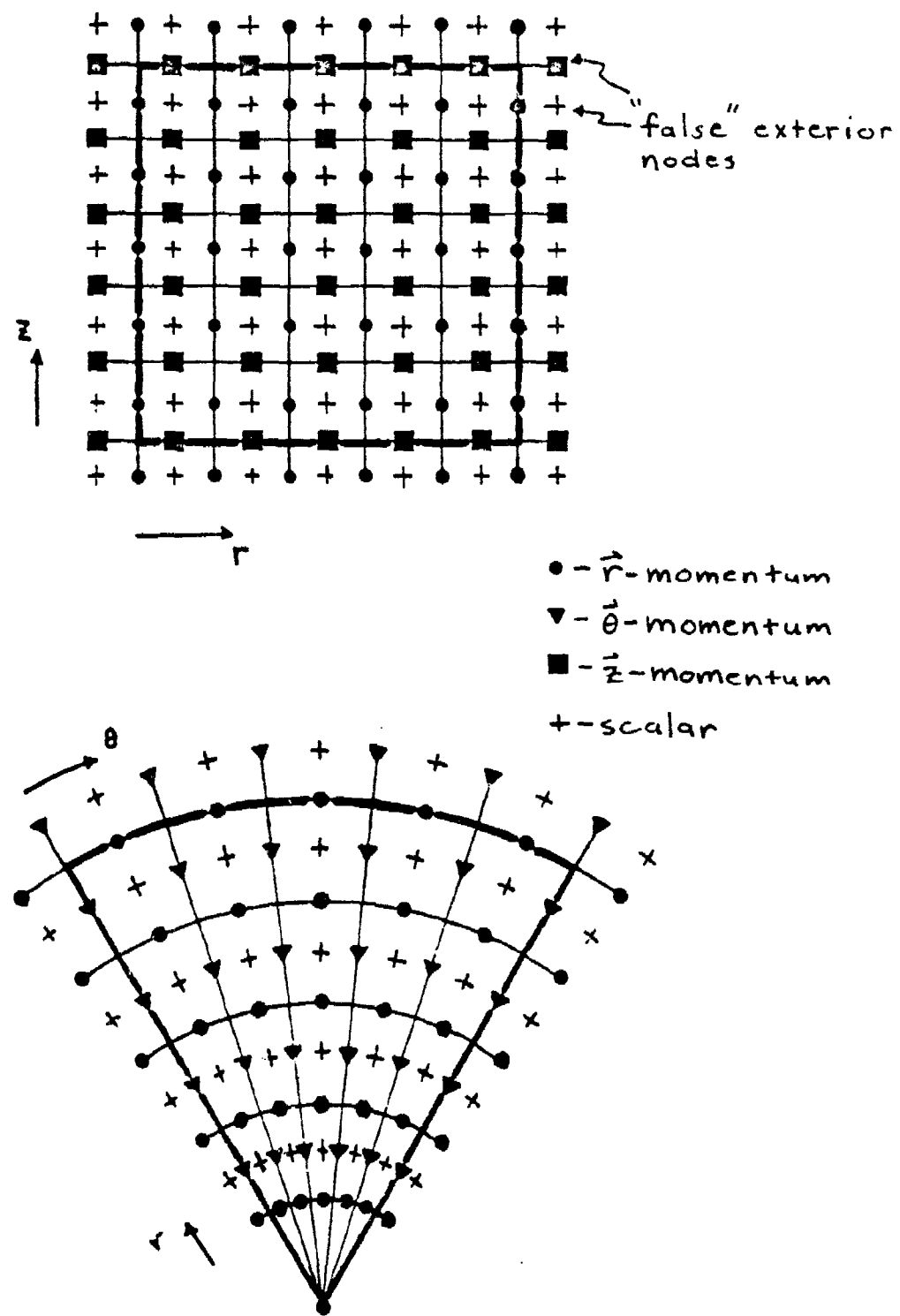
+ – scalar

Figure 18.   Staggered Grid Layout for the Wedge-Shaped Domain
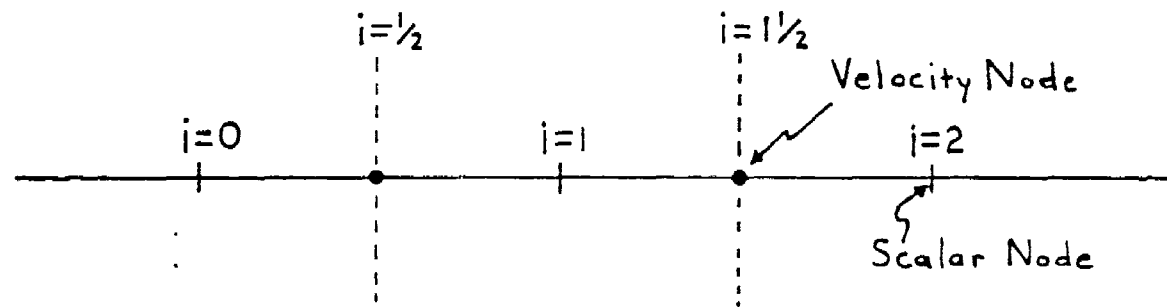
Figure 19. Determination of the Velocity, u at a
Scalar Node
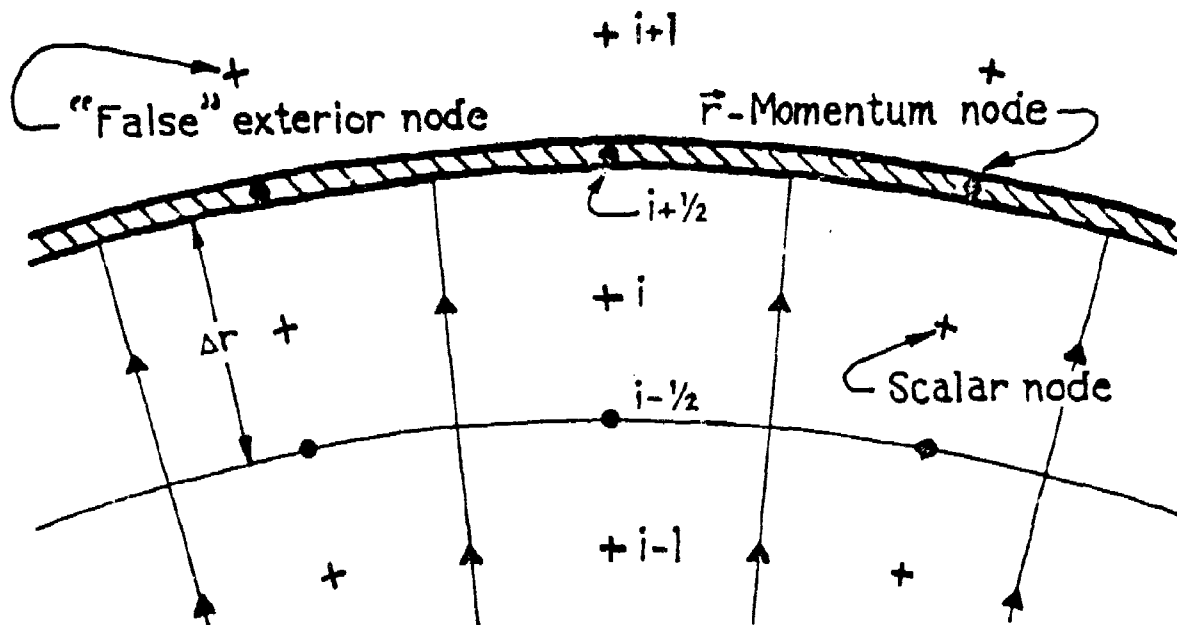
Figure 20. Evaluation of Flux Term at the Boundary r=R
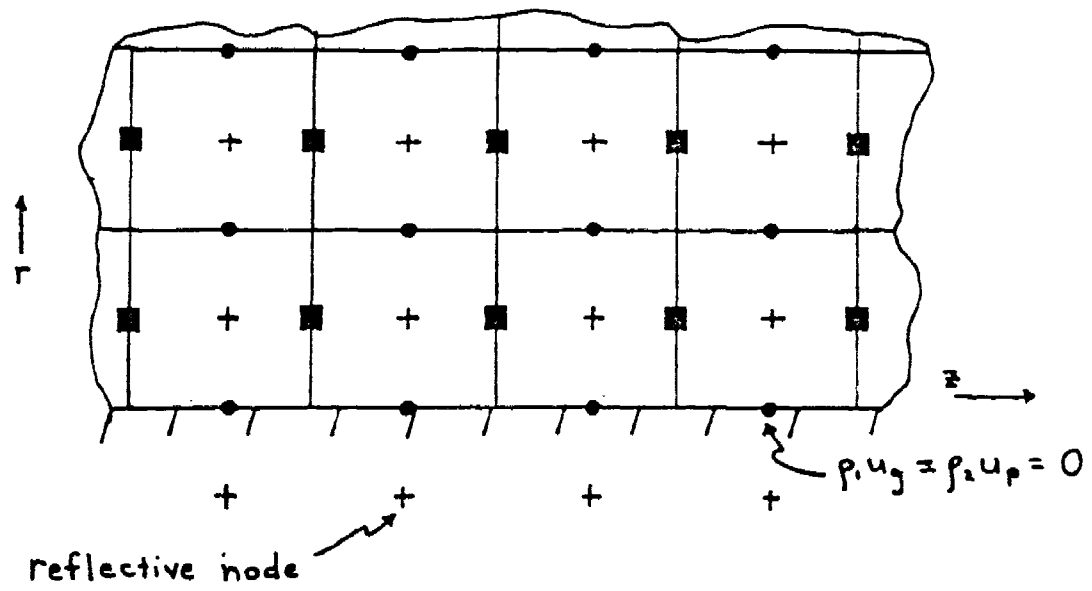
Figure 21.   Evaluation of Flux Term at
   the Boundary r=0 ,
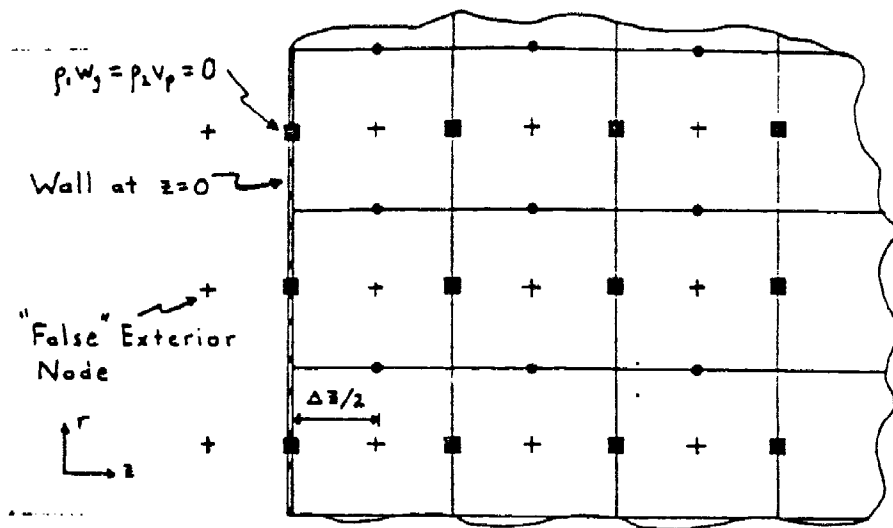
Figure 22. Evaluation of the Flux Term at the Boundary z=0
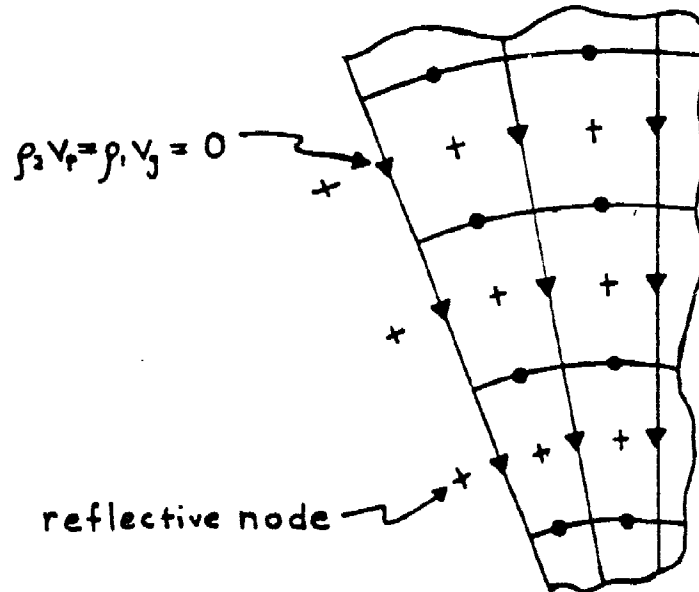
Figure 23. Evaluation of the Flux Term at the Boundary $\theta=\theta_1$
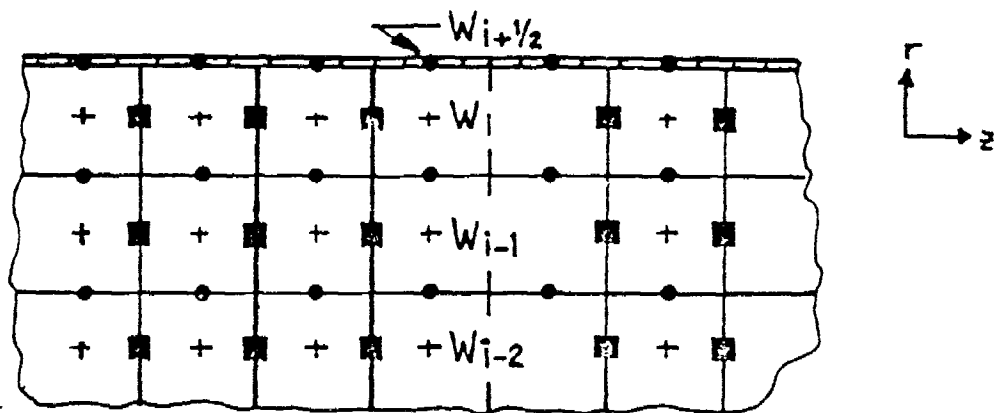
Figure 24. Determination of the Value
of W at i + 1/2
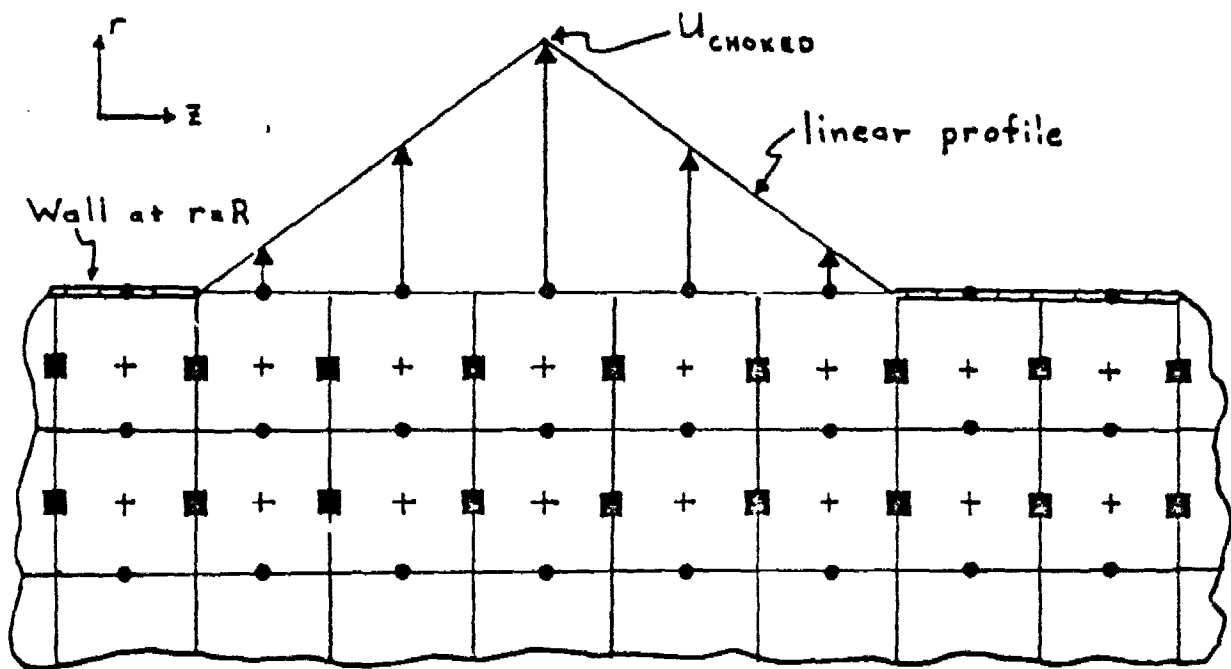

Figure 25. Prescribed Radial Velocity Profile for
Holes Larger Than One Node

71
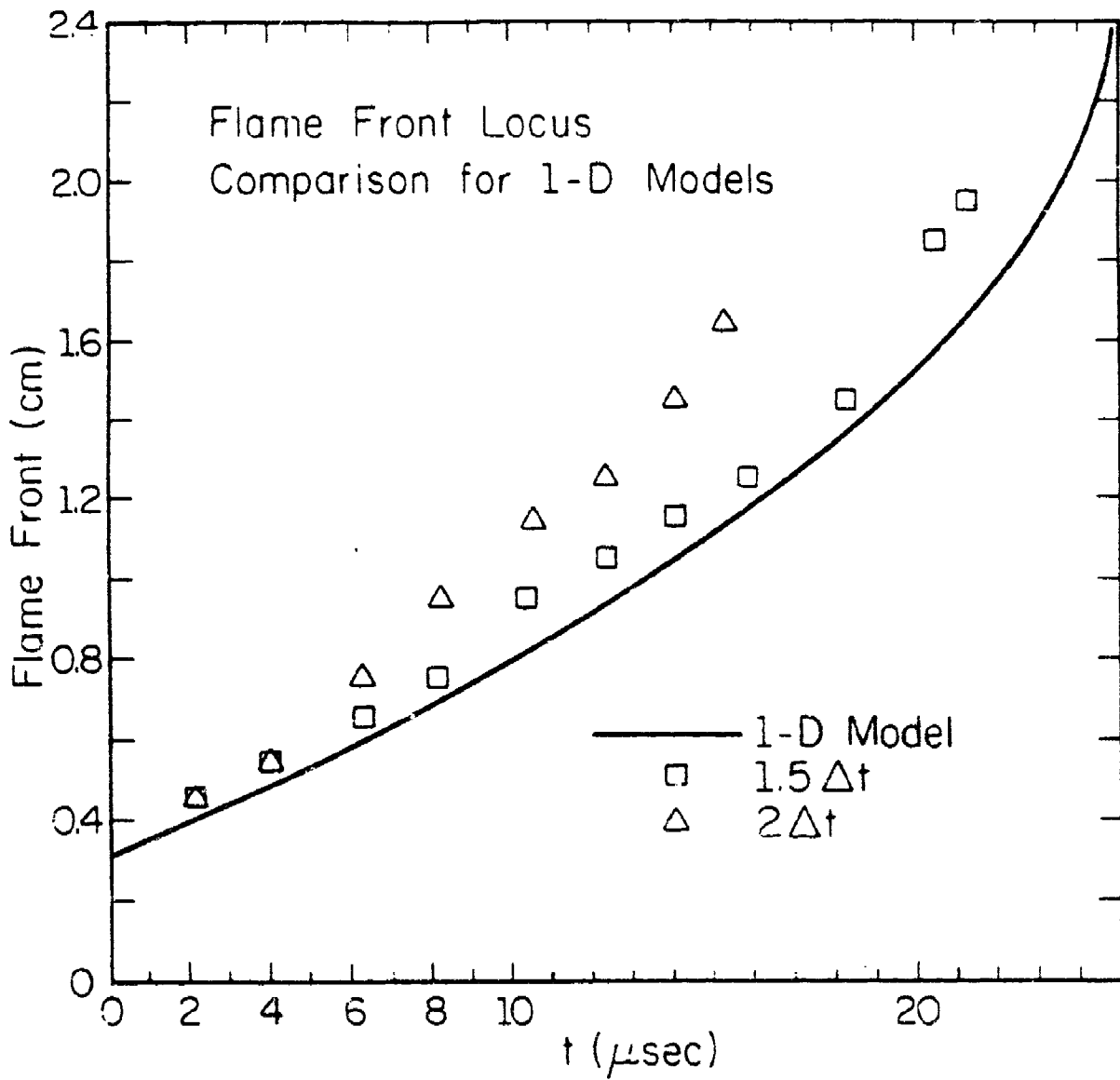
Figure 26.   Comparison of Flame Front Locus
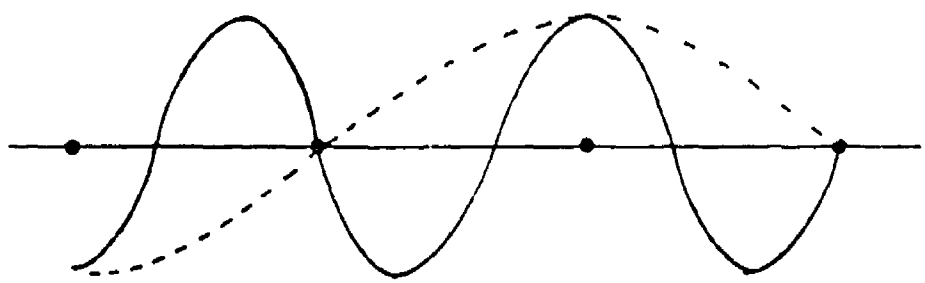
Figure 27. Aliasing of a Wave Having a Wavelength Which Is
Too Short to Resolve on the Given Grid
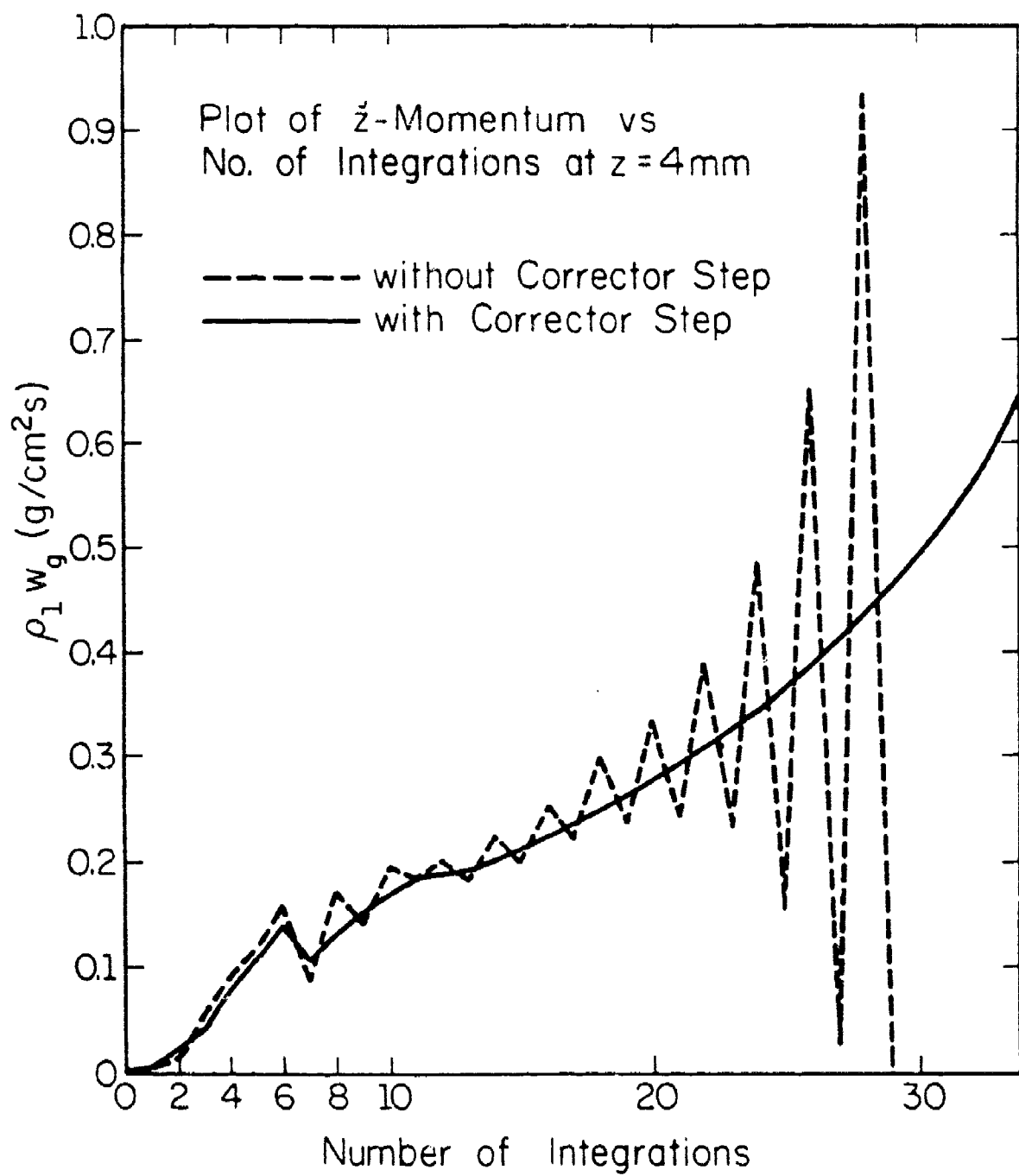
Figure 28. Comparison of z-Momentum Showing Improvement in Stability Caused by Predictor Corrector Strategy

74

SECTION V

RESULTS

1. INTRODUCTION

The numerical scheme described in the previous chapter was incorporated
into a FORTRAN-V computer code. In this chapter some initial calculations are
presented which clearly show that unsteady multi-dimensional flow can be
modeled by this code. While the output presented here is still of a
preliminary nature, it nonetheless shows the suitability and potential of our
model for predicting the rapid transients encountered in this type of work.

As was shown by the one-dimensional model in Section II, a totally
confined bed of small energetic particles exhibits rapid localized increases
in pressure, temperature, velocity, and density (see Figure 4). Pressure can
increase by five orders of magnitude in less than 0.1 milliseconds. One
should therefore expect difficulty in developing a three-dimensional depiction
capable of simulating such severe transients. Since the inclusion of multi-
dimensional effect# and the partial confinement boundary condition greatly
complicates the problem, it was decided to defer the inclusion of the mass
loss through the container walls (the alternate boundary condition) until the
ability of the model to simulate the totally confined multi-dimensional flame
spreading was proven. Paragraph 2 discusses the input for the baseline case
in which a totally confined bed was initiated in such a manner that the flame
spreading would be two-dimensional, while Paragraph 3 presents the results for
this case. Paragraph 4 presents the currently available results for the more
complex partially confined case.

2. BASELINE CASE DISCUSSION

All the test cases reported in this section modeled granular beds of
explosive with a fixed bed radius of 0.5 cm and lengths ranging from 3 cm to 6
cm. Although these dimensions are obviously smaller than those of actual
explosive-containing warheads, they are sufficiently large for us to study the
developing transients which appear during the early portion of the event.
Also, while the code is capable of modeling three-dimensional flame spreading,
only two-dimensional flame spreading results will be shown here for ease of
data presentation. (Contour plotting only allows three parameters, one
dependent and two independent variables, to be plotted.)

Initiation of the granulated explosives was achieved by assuming, as
before, that a prescribed high-temperature profile exists at one end of the
bed (see Figure 29).

The temperature at several prescribed points in the profile was assumed
to be above the bulk ignition temperature of the solid, thus allowing the
particles to ignite at time $t = 0$. In this manner the user can control the
initial spatial domain in which the flame spreading will take place. One-
dimensional flame spreading (no variation of the parameters in the $\bar{r}$ -
direction or $\bar{\theta}$ -direction) can be produced by assuming a profile one shown in
Figure 29, where the gas and particle temperatures vary only in the z-
direction. Two-dimensional flame spreading in the $\bar{r}$ and $\bar{z}$ -directions can be
produced by assuming gas and particle initial temperature profiles which decay
to the ambient temperatures in both the $\bar{r}$ and the $\bar{z}$ -direction. Finally, full
three-dimensional flame spreading can be produced by assuming an initial
profile which varies in all (r-, θ-, and z-) directions.

76

Input parameters for the two-dimensional baseline (no vent) case are given in Table 4:

TABLE 4: INPUT PARAMETERS

Bed Length, L	$3 \text{ cm} \leq z \leq 6 \text{ cm}$
Bed Radius, R	0.5 cm
Bed Angle, θ	5°
Particle Radius, r_{p_o}	$100 \text{ } \mu m \leq r_{p_o} \leq 200 \text{ } \mu m$
Porosity, ϕ	0.30
Particle Density, ρ_{p_o}	1.675 g/cm^3
Ambient Gas Temperature, T_{g_o}	300 K
Ambient Particle Temperature, T_{p_o}	300 K
Initial Gas Pressure, P_{g_o}	100 kPa
Particle Ignition Energy, E_{ign}	$4.6206 \times 10^9 \text{ ergs/g}$
Space Increment, Δz	1 mm
Space Increment, Δr	1 mm
Angular Increment, $\Delta \theta$	5°
Initial Gas Viscosity, μ_{g_o}	$1.8 \times 10^{-4} \text{ dyne-sec/cm}^2$
Prandtl Number, Pr	0.7
Gas Constant, R'	296.79 ergs/K gmole
Specific Heats, C_{v_g} & C_{v_p}	$1.51 \times 10^7 \text{ ergs/g K}$
Particle Chemical Energy, E_{chem}	$5.74 \times 10^{10} \text{ ergs/g}$
Burning Rate Index, n	1.0
Burning Rate Coefficient, a	0.001
Gas Equation of State Constant, b_1	4.0
Number of Nodes	5 x 1 x 60
Number of Variables in Storage	20

3. RESULTS FOR THE TWO-DIMENSIONAL SIMULATIONS

Figures 30-46 show the pressure, temperature, radial velocity and axial velocity profiles for the gas at various times. The explosive is 6 cm long, composed of 200 μm sized particles. The grid dimensions were 5 by 1 by 60 nodes, and the bed was initiated in such a manner that the flame spreading was two-dimensional (in the $\hat{r}$- and $\hat{z}$ -direction).

Figures 30-33 show the rapid increase in the gas pressure at the initiated end of the bed, as well as the forward motion (along the $\hat{z}$ -axis) of the pressure front as time increases. (Note that the scale on the pressure axis changes on each figure.) Particularly interesting is the peak forming at the head of the pressure wave at t = 46.3 μsec. This is indicative of a shock forming in the granular explosive bed.

Calculations were not possible after about 50 μsec (350 integrations) due to the rapidly developing shock described above. This was caused by the fact that we are using a constant time step, rather than a time step which adjusts itself to the rapidly changing bed conditions. As the shock forms, pressure gradients across the front of the wave become very steep and much smaller time steps are needed to allow the differencing scheme to adjust to these strong gradients. The instability was caused, then, not by the finite differencing scheme, but by the simplification of assuming a constant time step.

Most interesting of all is to observe that as time increases, gradients in the radial direction vanish entirely and the flow, which was initially two-dimensional, becomes totally one-dimensional (with gradients occurring only in the axial direction). This is exactly what the experiments of Bernecker and Price Reference 9 have shown to occur when totally confined explosives are initiated in a multi-dimensional manner. Figures 38-43 show this phenomena more clearly.

Figures 34-37 show the gas temperature profiles at various times during the burn. One can clearly see the gradients in the radial direction during the early stages, as well as the disappearance of these gradients during the latter stages.

Figures 38-43 show the decay of the radial gradients most dramatically, since the disappearance of these gradients forces the radial velocity to be zero. In Fig. 38 we see a very prominent radial velocity profile at t = 13.3 μsec. The radial velocity here is positive, meaning that the direction of the flow is outward from the boundary at r = 0. Since there is an impermeable wall at r = R, we know that the gas must eventually reflect off of this wall and reverse its direction.

In Figure 39 we see that the location of the peak radial velocity has moved downstream (in the z-direction) and the velocity behind the peak is negative, as expected, due to the reflection of the flow in that region from the wall. The reverse flow, though difficult to see in Figure 39 because of the manner in which the figure is plotted, is more clearly evidenced by the trough behind the velocity peak shown in Figure 40. In Figure 41 we again see the reverse flow trough, noting that it has now moved farther downstream. This means that a portion of the flow which was positive in Figure 40 (at t = 34.47 μsecs) has reflected off the wall at r = R and is now heading back toward the center of the bed by the time t = 39.96 μsec. We can also observe the slight peak at z = 1 cm where a trough had occurred in the previous figure. This indicates that the reverse flow from Figure 40 has again reflected, this time from the boundary at r = 0, and is now again heading in the positive $\dot{r}$ -direction. One should also note the overall reduction in the magnitude of the velocities, indicating that the flow is indeed damping out.

79

(Note the change in scale on the radial velocity axis as compared to the previous figures.) Figures 42 and 43 show this behavior continuing until, at time t = 46.36 μsec, there is practically no radial velocity in the bed. (Note again that the scale on the radial velocity axis changes in these figures.)

Figures 44-47 show the developing axial velocity profiles. Again we note the initially two-dimensional profile decaying to a one-dimensional profile.

In Figure 48 the location of the flame front is plotted in r, z-space at various times during the event. We can note that initially the flame front location varies in both the $\vec{r}$ and $\vec{z}$ -directions. As time progresses, the variation of the flame front location as one moves in the $\vec{r}$ -direction becomes less and less, until at time t = 47.7 μsec no variation in the radial direction is predicted. Clearly, the flame front has become one-dimensional.

These results illustrate two key facts. First, the fact that the numerical scheme described in Section IV was able to handle the rapid flow transients indicates its suitability for use in analyzing dynamic two-phase, multi-dimensional flows. Secondly, the results also show that the model developed in Section III predicts behavior which is at least in qualitative agreement with data from experiments involving accelerating reaction fronts in granular beds of explosive solids.

One may ask at this point if a multi-dimensional flame spreading model is only of limited use, since, in the presence of total confinement, the flame spreading will eventually asymptote to a one-dimensional process. One must realize that while the predictions presented in Figures 30-46 show that multi-dimensional effects last only 50 μsec for our example baseline case, such an amount of time represents a significant percentage of the total duration of

typical DDT events, which may take only 100-200 μsec. Hence, this transient two-dimensional stage will indeed have a significant effect on a prediction of the detonation run-up length.

Figures 49-51 show the gas pressure, axial velocity, and flame front profiles in a bed which was initiated in a purely one-dimensional manner, and compare them to the results from the same bed initiated in a two-dimensional manner. In both of these case the initial particle size was fixed at a 100 μm radius. Figure 49 shows the gas pressure profile at t = 19.5 μsec for the case in which the initiation was one-dimensional compared with the two-dimensional case at r = R/2, again at t = 19.5 μsec. One can see the obvious difference in the two profiles. Figures 50 and 51 provide similar comparisons of the axial velocity and the flame front locus, respectively. Again, the profiles are markedly different for the two different types of initiation. Therefore, we can conclude that while the multi-dimensional effects eventually decay they still have a significant effect on the results.

4. PARTIAL CONFINEMENT CASE

Once the capabilities of the code had been shown for the baseline (no vent) case, calculation was made to test the model's ability to simulate flow with partial confinement. Again a 3 cm long bed of particles with an initial radius of 100 μm was modeled. A crack 3 mm (3 nodes) in width was assumed to exist around the entire circumference of the bomb. This latter condition was imposed to cause the flow inside the domain to effectively remain two-dimensional. The crack was located a distance of ℓ_0=1.55 cm from the initiated end (z=0). A uniform profile was used to assure that the initial flame spreading one-dimensional, in order to make the multi-dimensional effects caused by the hole located at a fixed radius to be more apparent.

Figure 52 shows the predicted gas pressure profile at t=21.48 usecs. One can see that behind the hole the profile is indeed one-dimensional. The small "indentation" in the profile at z=1.55 cm indicates the location of the hole. The flow at this point is still largely one-dimensional because the pressure front has only just reached the hole.

Figure 53 shows the gas pressure profile at a time 1.5 usecs later. By then the effect of the hole is very apparent. The pressure is severely diminshed at the crack itself, while downstream of the hole (i.e., in the positive $\vec{z}$ -direction) one can see strong gradients in the $\vec{r}$ -direction, indicating that the flow is multi-dimensional. It is especially interesting to note that downstream of the hole the pressure is higher at the wall than at the centerline. This is caused by the fact that downstream of the hole, the radial velocity at r=R (i.e. the solid wall) must again be equal to zero. The radial velocity components, induced by the gas flowing out of the hole, must decelerate again to zero at the wall, thus increasing the pressure.

Figure 54 shows a plot of the radial velocity profile shortly after the pressure wave has reached the hole. One can see that, due to the one-dimensional initiation, the radial velocity is zero everywhere except at the hole. In Figure 55, the pressure signals from the hole have propagated down to r=0 and upstream of the hole, inducing radial velocity components in these regions.

In Figure 56 one can see that the velocity profile is even more prominent, with a dimple in the profile upstream of the crack. This indicates that the radial flow induced by the hole has reflected from the solid wall at r=R and is flowing back toward the centerline.

For this partially confined case, the calculations were continued until the flame front reached the end of the bed at t=23.2 usec, at which point the calculations were automatically shut off. This is somewhat significant in that when the code was run for the identical input conditions, except with total confinement, the formation of a shock wave prevented further computations after a time of 19.0 μsec. In other words, the existence of the hole sufficiently weakened the formation of a $\overset{\star}{z}$ -direction shock so that the scheme remained stable for the same spatial griding.

The results presented in this section clearly indicate that the model and code developed in this study has the capabilities needed for calculating partially confined, unsteady multi-dimensional flows. The potential for carrying out calculations for (more realistically) larger domains, with different vent openings and for explosives with different granulation is very clear.

5. SUMMARY AND RECOMMENDATIONS

Two models were developed to predict the behavior of unsteady two-phase reactive flows in a partially confined region. A pseudo two-dimensional model was applied for a wide variety of cases and the results indicated that partial confinement does have a significant quenching effect on a forming detonation wave.

Since the pseudo two-dimensional formulation required many major simplifying assumptions, it was decided that a three-dimensional unsteady model should be developed to provide a more realistic fluid mechanics simulation. The conservation equations were derived in cylindrical coordinates and a new numerical scheme was devised to integrate these

83

equations. At the time of this publication, preliminary calculations of this model indicates that it will provide stable, physically meaningful results which are consistent with the very limited experimental evidence available.

Time constraints on the publication of this analysis prevents a larger number of calculations from being performed with this multi-dimensional model.

To conclude, the following proposed improvements are recommended for future work.

(1) Derivation of an Optimal Time Step:

In order to be able to predict the formation of a steady-state detonation wave within the fragmented explosive bed, stability of the numerical differencing model must be maintained in spite of the presence of a shock wave within the computational domain. To achieve this, the time step must be sensitive to the instantaneous conditions inside the bed. A Von Neumann-type stability analysis (Reference 16) may be necessary to determine the formula for the optimum time step.

(2) Incorporation of Improved Constitutive Relations:

As noted in Appendix A, the applicability of the data required for the constitutive relations under the wide range of conditions imposed by this problem is questionable. The incorporation of the new gas equation of state being developed by Wang and Krier Reference 22 and the Mie-Grunniesen solid phase porosity-pressure relation should help improve the accuracy of the model.

(3) Devising Alternate Forms of Initiation:

The use of a prescribed temperature to ignite the particles, while proving satisfactory for initiating the bed, is not always

84

realistic. Explosive warheads which are to be modeled are often initiated by means of a shock from an exploding fuse. Clearly, at time t=0, not only temperature but high local pressure should be modeled.

(4) Application of New Generation Computer Technology:

The CDC CYBER-175 computer currently in use at the University of Illinois at Urbana-Champaign was employed to run the code shown in Appendix D. While this is one of the fastest and largest mainframe computers on the market it is not totally adequate for all the aspects of this type of work. Though we have been able to demonstrate the capabilities of the code for predicting multi-dimensional flame spreading in small domains using the CYBER-175, the storage and processing requirements for applying this code to larger domains (with full three-dimensional flame spreading) would necessitate the use of an even more powerful computer.

The code requires that the values of ten primary variables be stored at two time levels, as well as the values of twelve secondary variables at one time level, at each node. The core memory of the CYBER-175 allows the user 131,000 words of storage. Leaving enough memory for the code itself, this restricts the maximum computational domain to 3500 nodes. Given the size of the space increments needed to assure proper resolution (approximately 1×10^{-3}m), this limits us to calculating cases representing relatively small domains. Of course, infinite storage is available by using off-line memory, but only at an increased cost to the user.

85

This problem may be solved by the utilization of the new generation super-computers, such as the CRAY-1. The increase in core memory (1-4 million words for the CRAY-1) offered by such a computer would allow us to perform calculations for much larger domains. Furthermore, the increased computational speed of these computers will help keep the computational costs to a minimum.
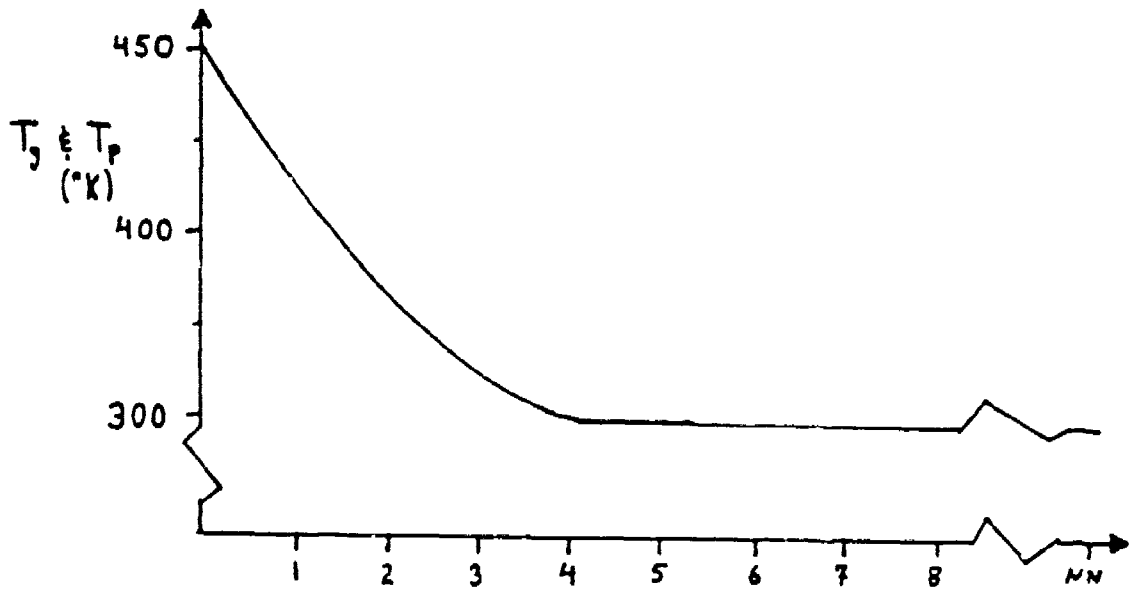
Figure 29. Prescribed Temperature Profile Used for
Bed Initiation
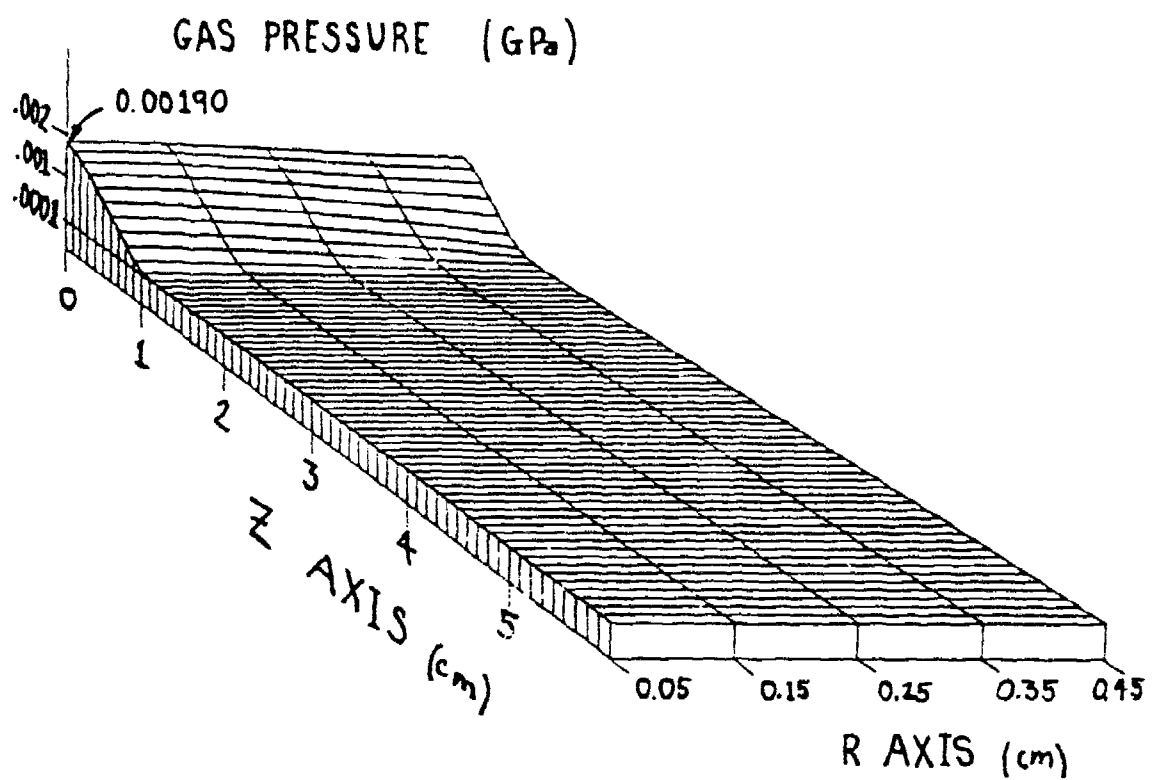
Figure 30. Gas Pressure Profile at t = 13.28 μsec
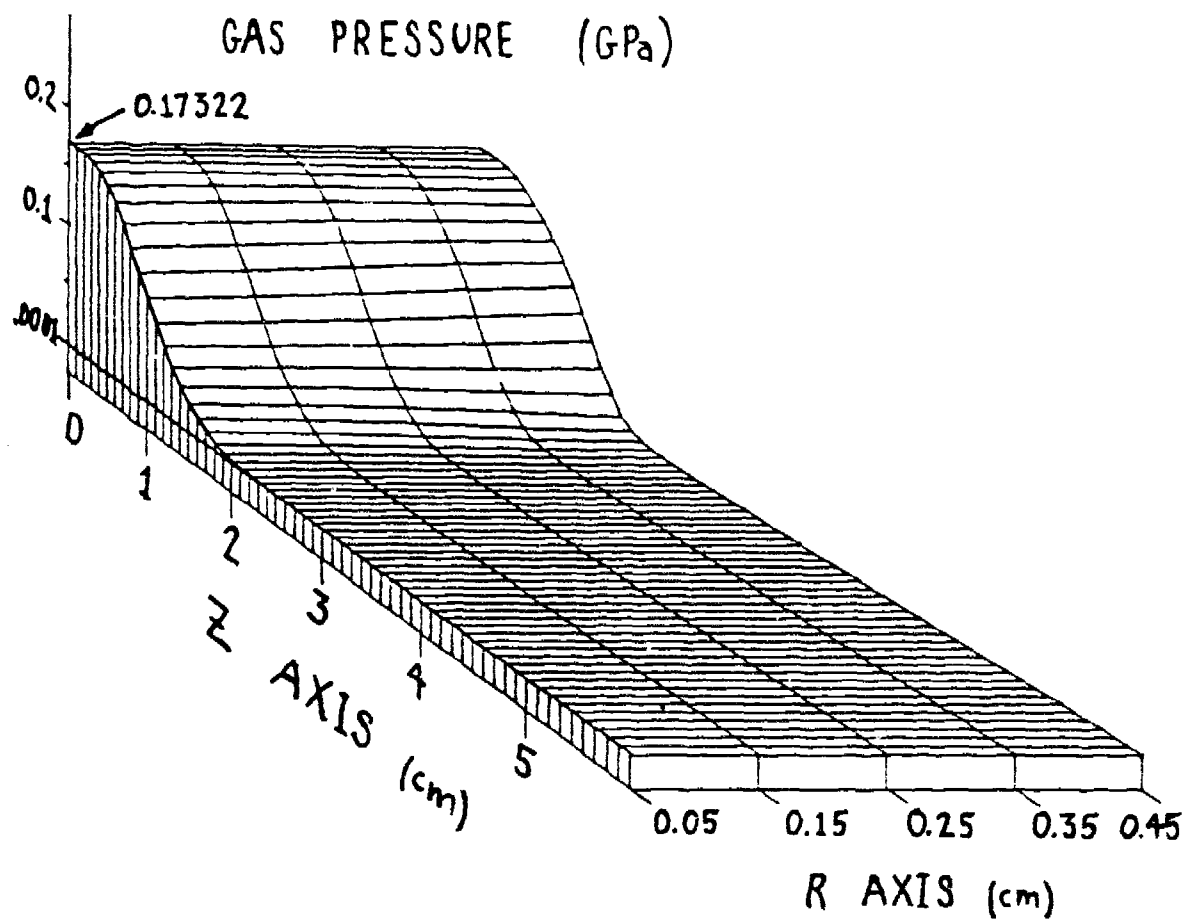
Figure 31. Gas Pressure Profile at t = 34.47 μsec
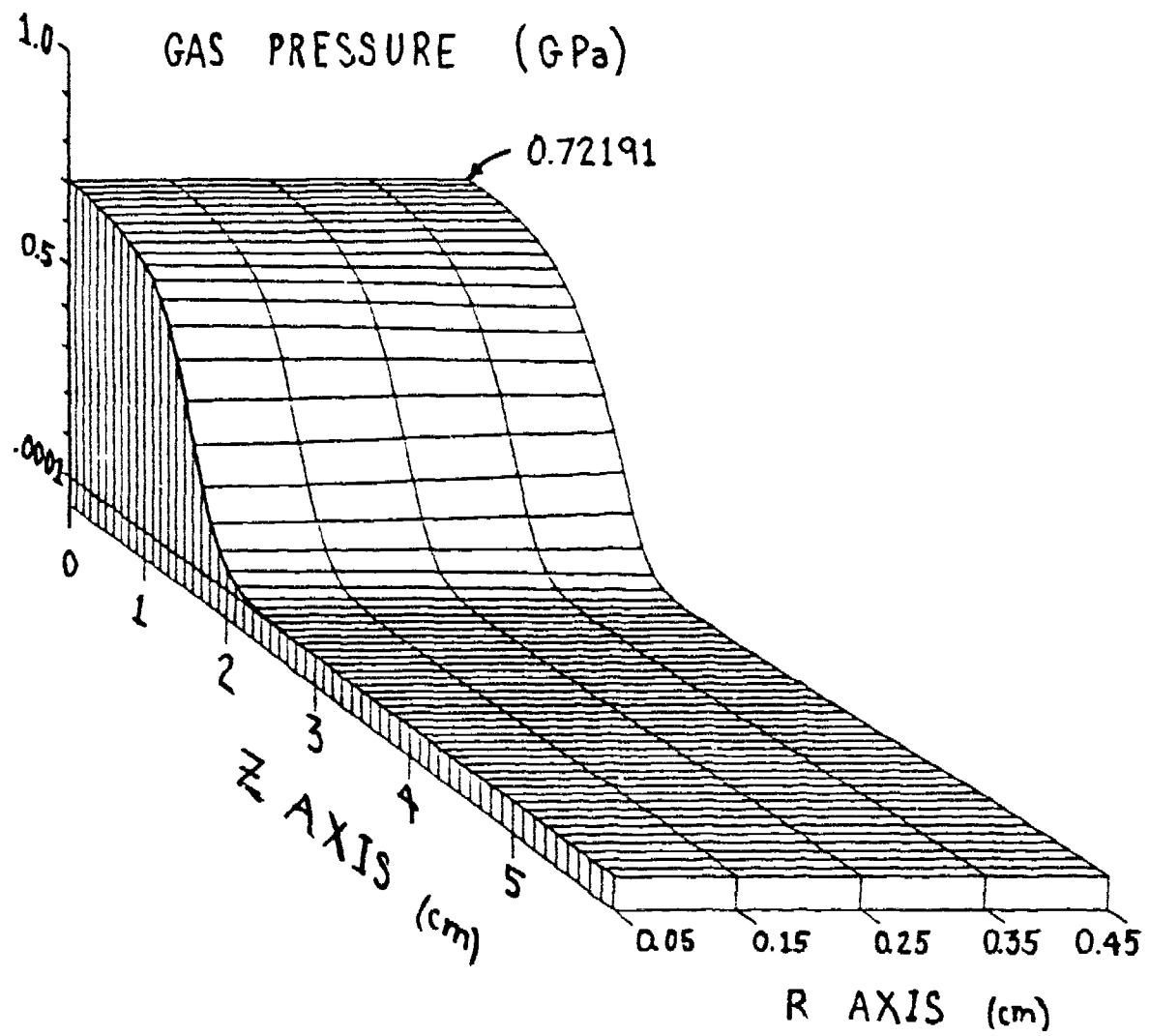
Figure 32.   Gas Pressure Profile at t = 39.96 μsec
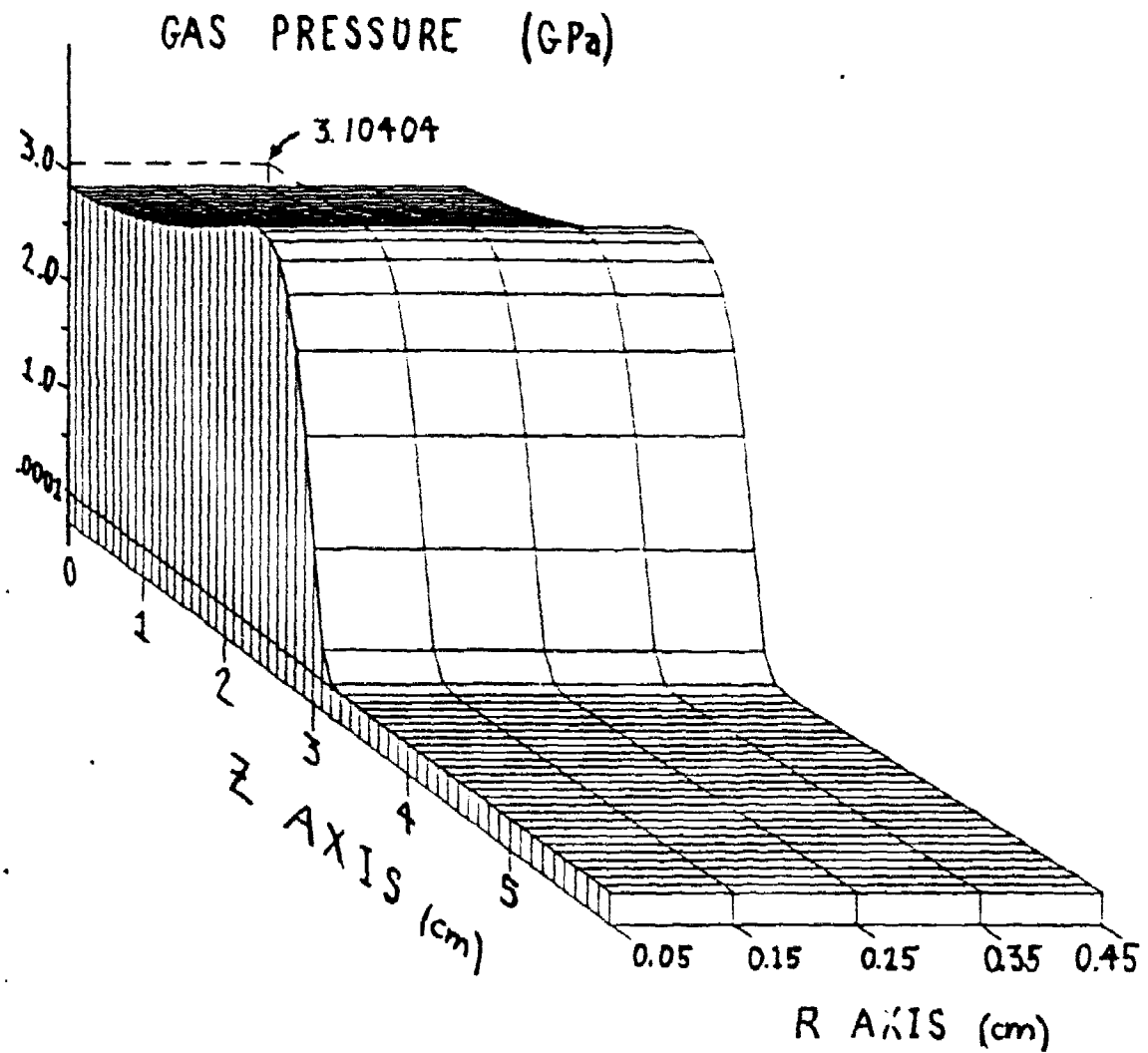
Figure 33. Gas Pressure Profile at t = 46.36 μsec
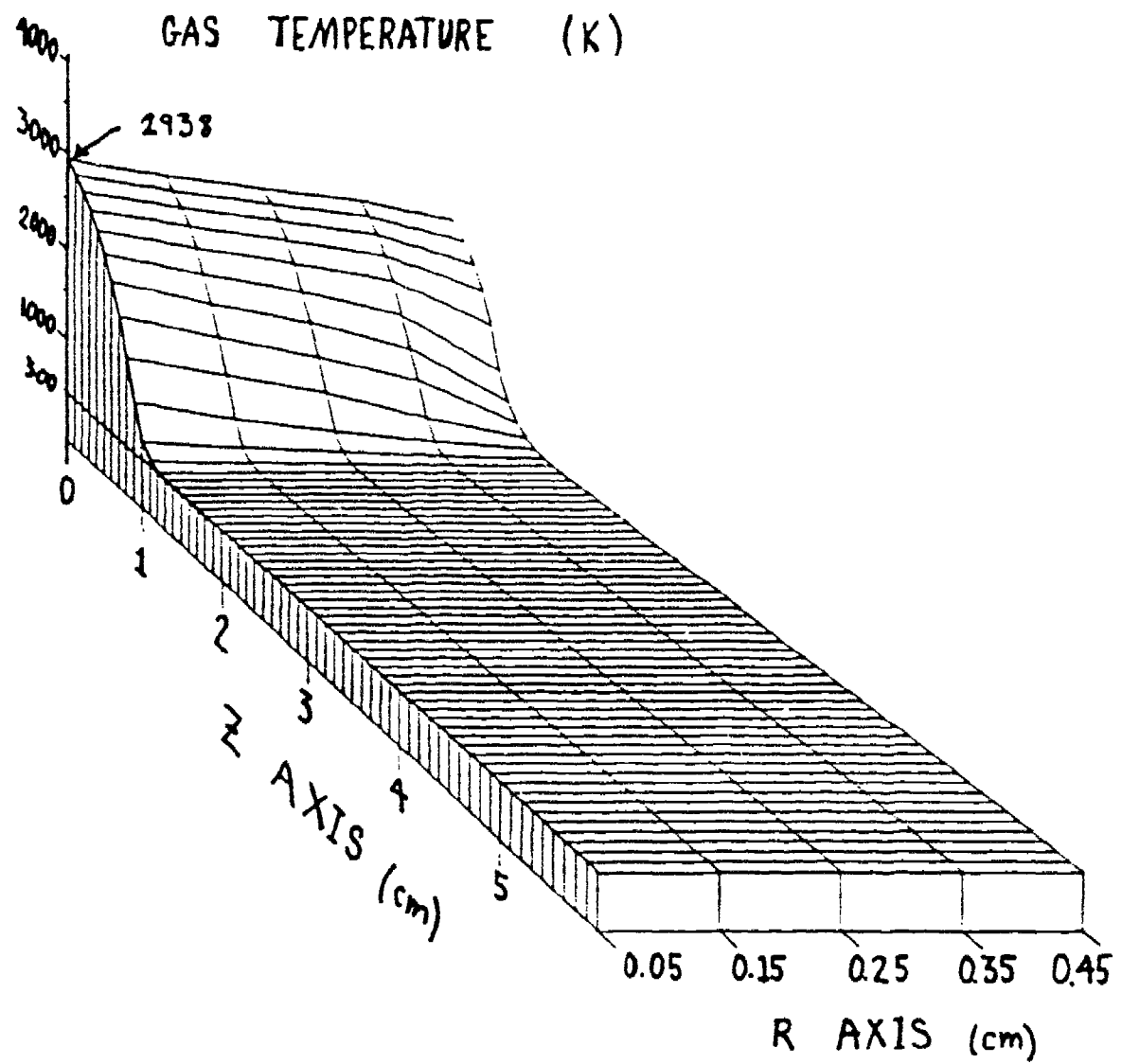
Figure 34.   Gas Temperature Profile at t = 13.28 μsec
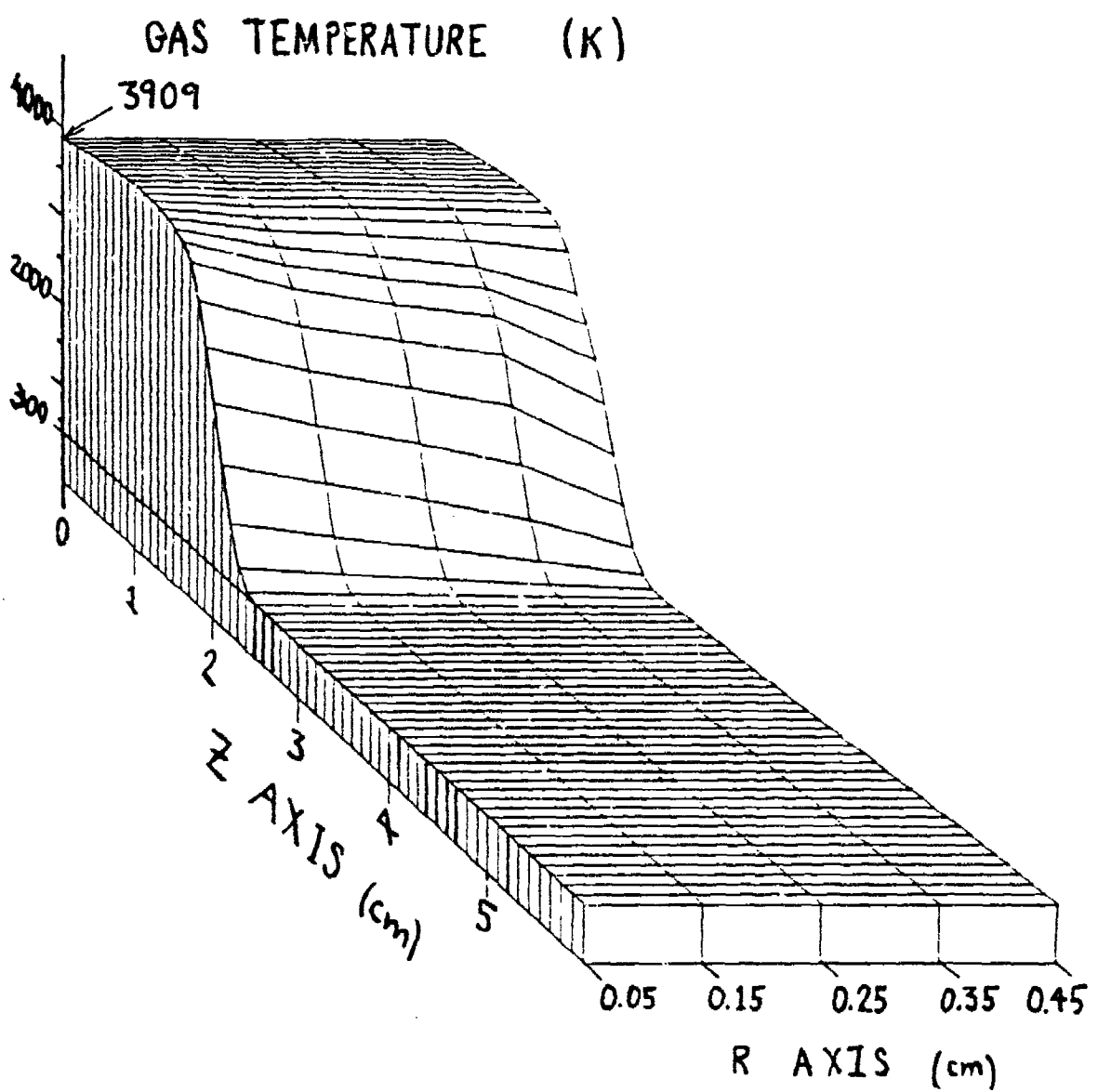
Figure 35. Gas Temperature Profile at t = 34.47 μsec
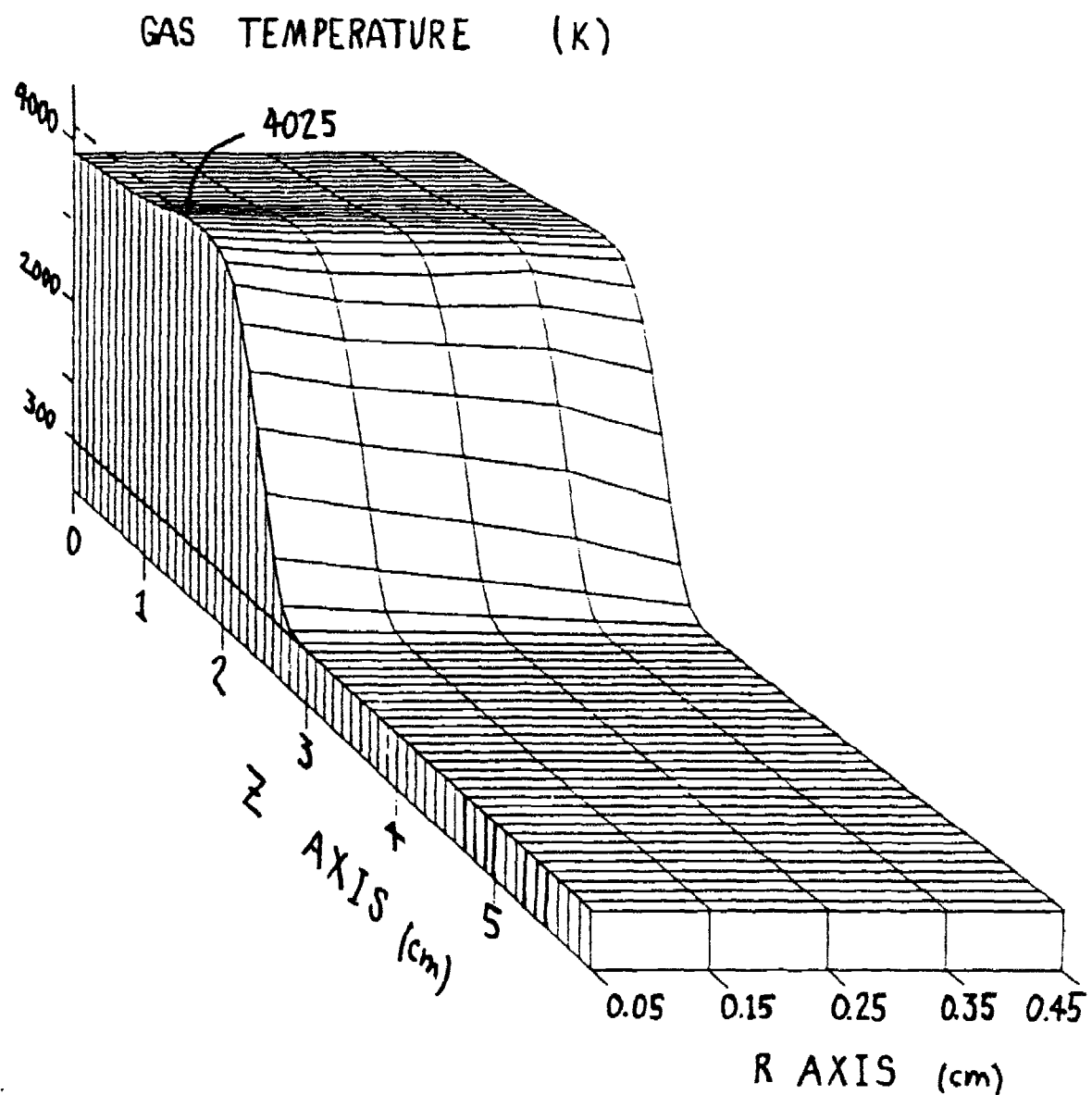
GAS TEMPERATURE (K)

Figure 36. Gas Temperature Profile at t = 39.96 μsec

94
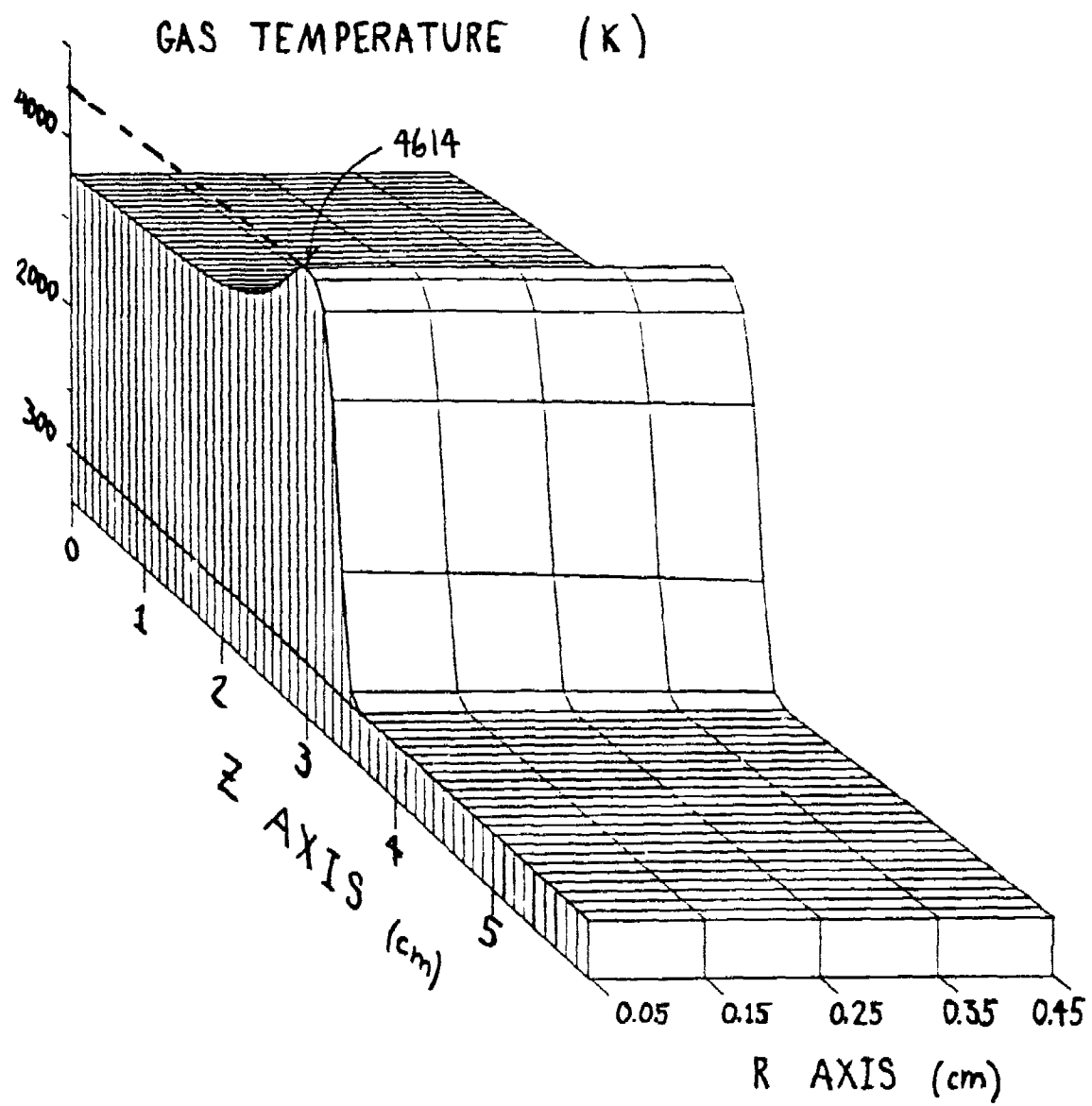
Figure 37.   Gas Temperature at t = 46.36 μsec
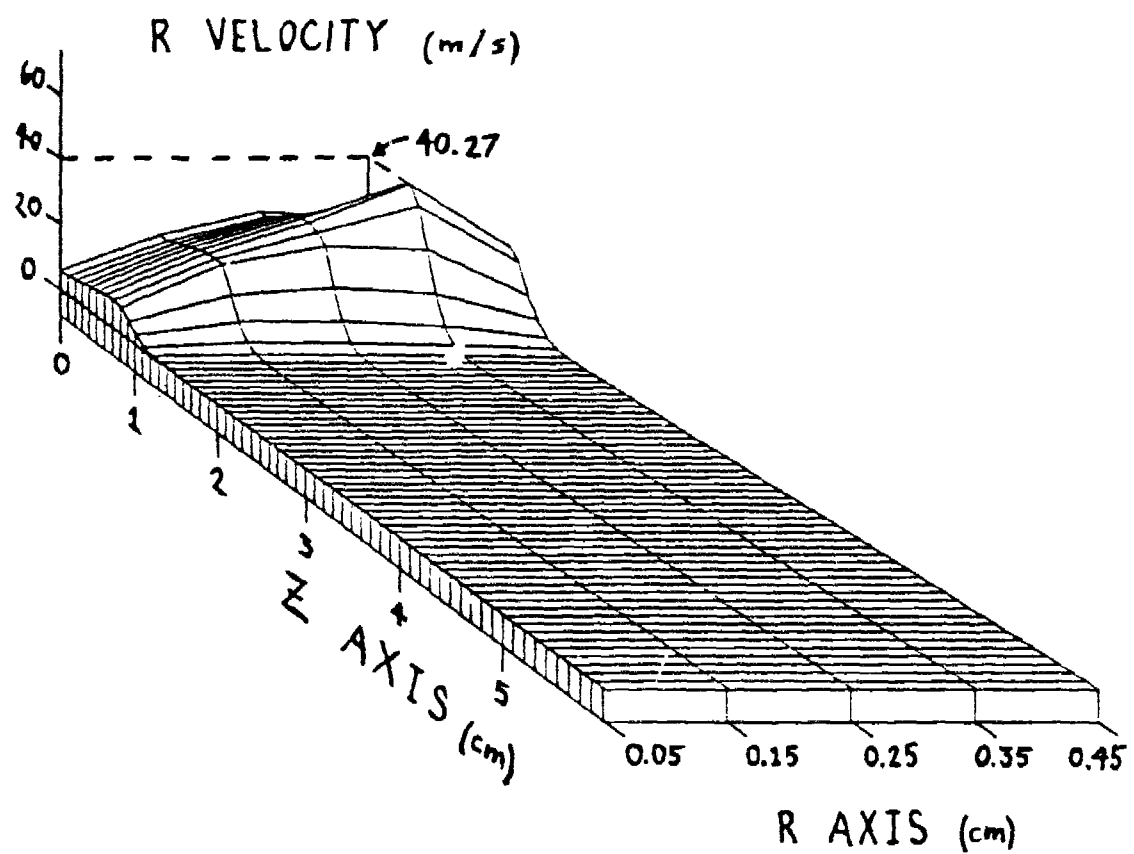
Figure 38. Gas Radial Velocity Profile at t = 13.28 μsec

R VELOCITY (m/s)

59.58

Z AXIS (cm)

R AXIS (cm)

0.05   0.15   0.25   0.35   0.45
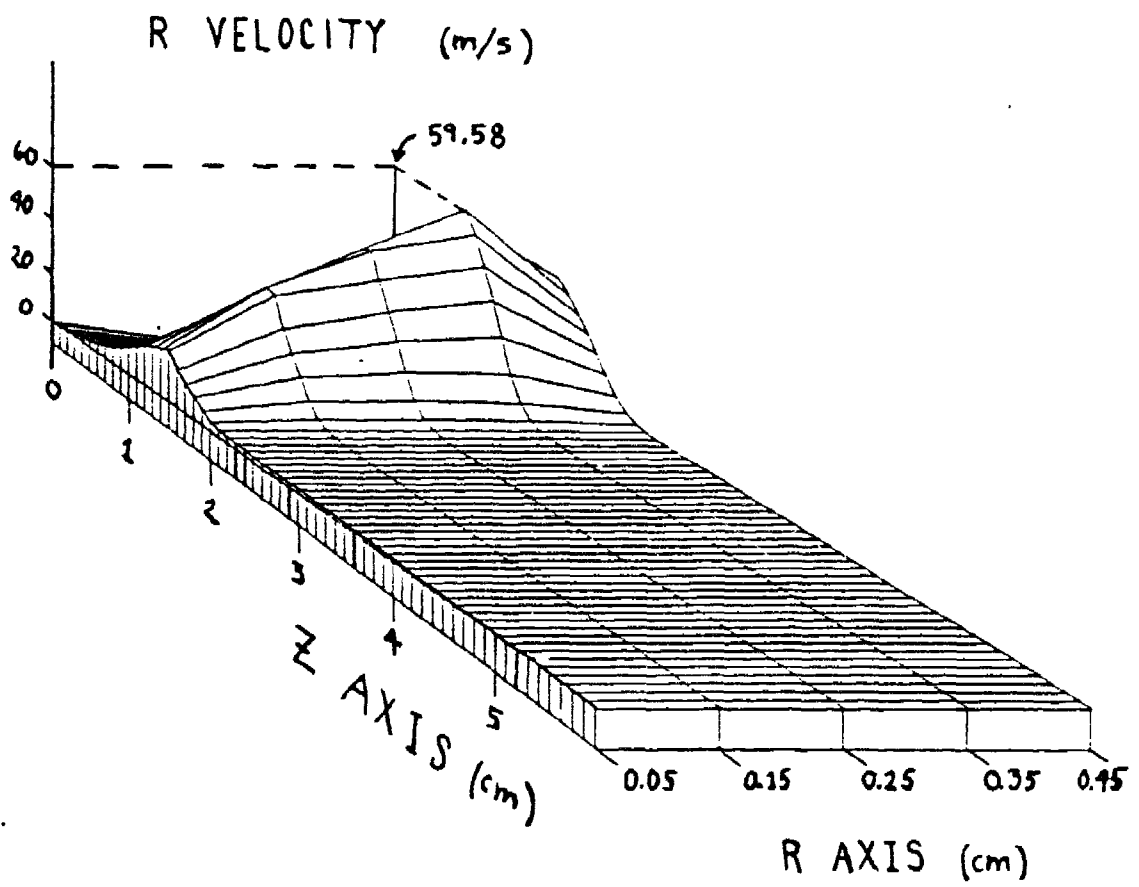
Figure 39.   Gas Radial Velocity Profile at t = 28.06 μsec
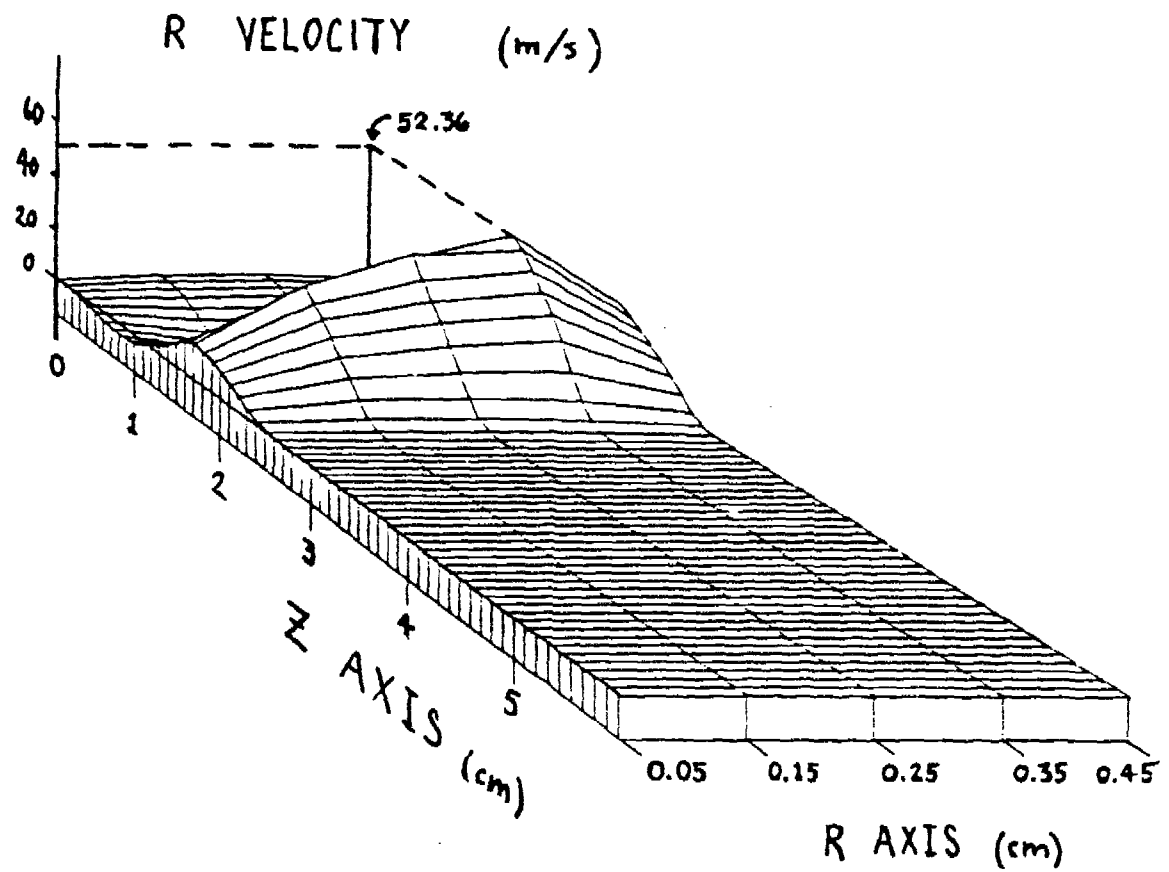
Figure 40. Gas Radial Velocity Profile at t = 34.47 μsec
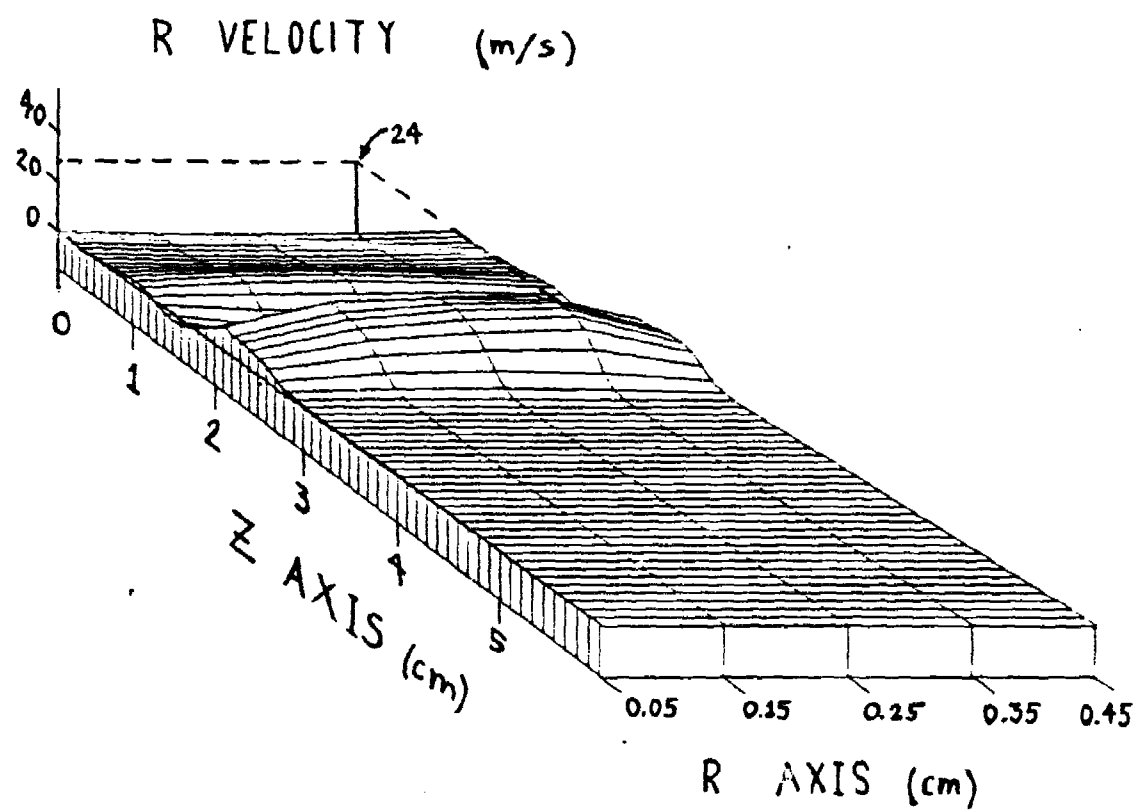
Figure 41. Gas Radial Velocity Profile at t = 39.96 µsec

99
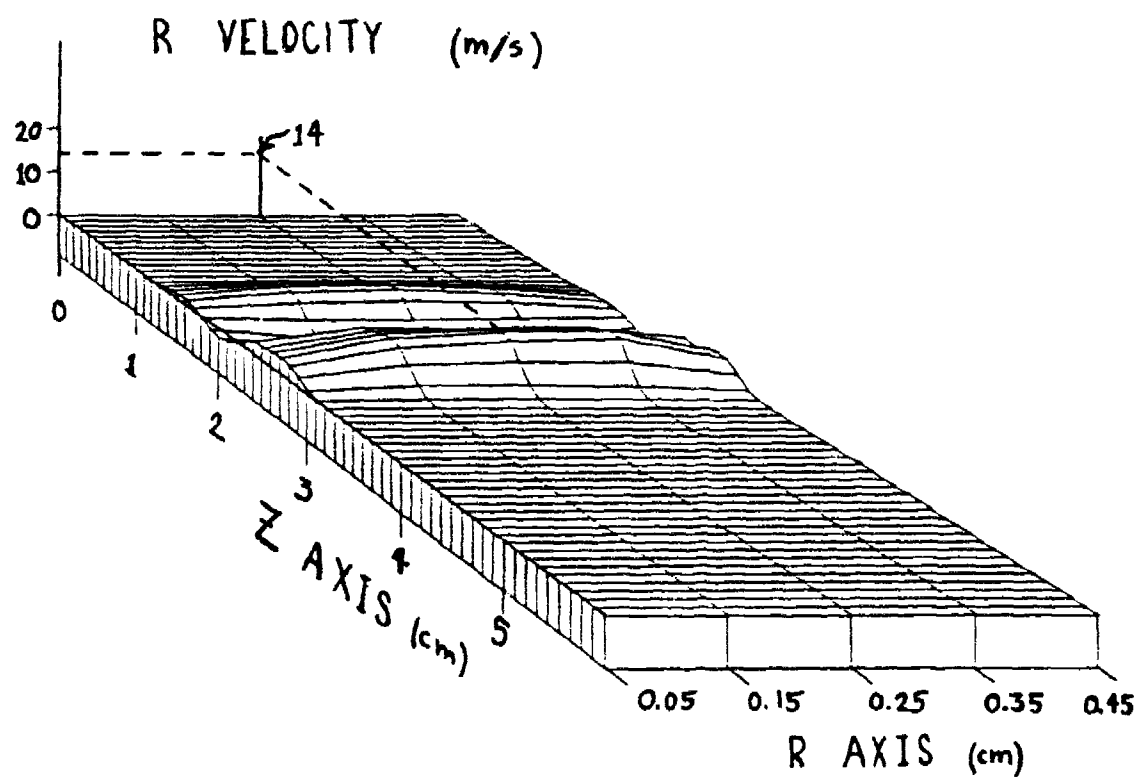
Figure 42.   Gas Radial Velocity Profile at t = 42.70 μsec
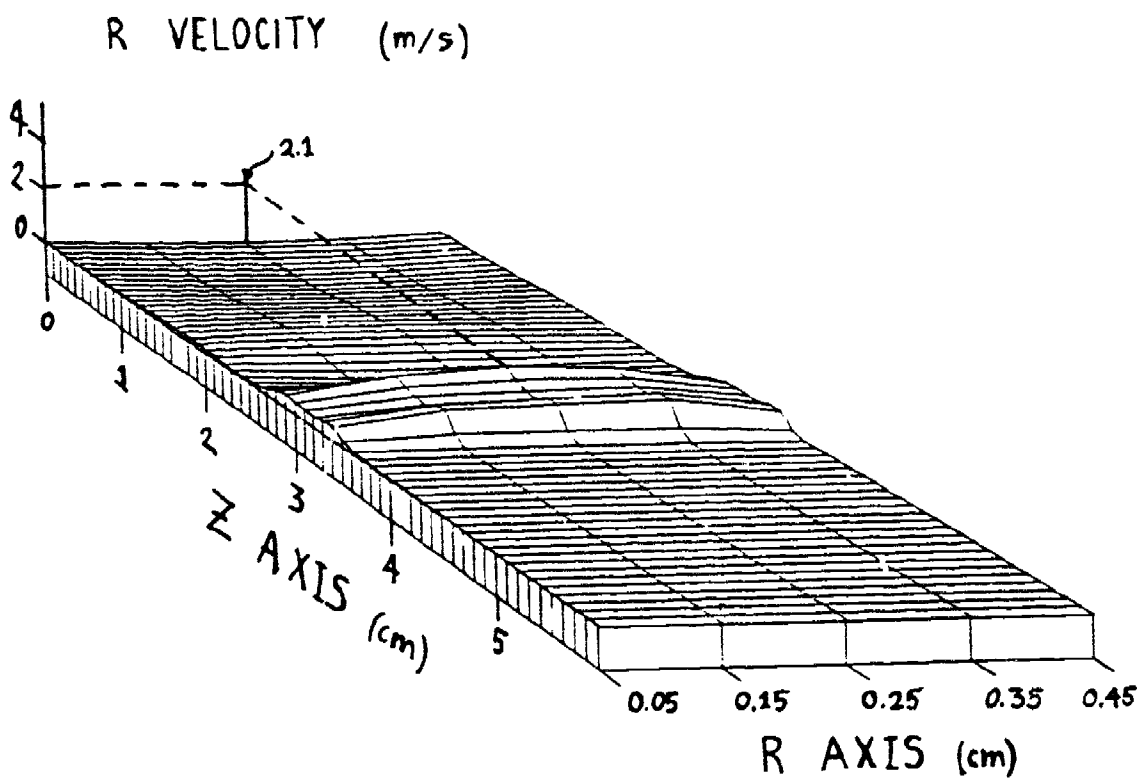
Figure 43. Gas Radial Velocity Profile at t = 46.36 μsec
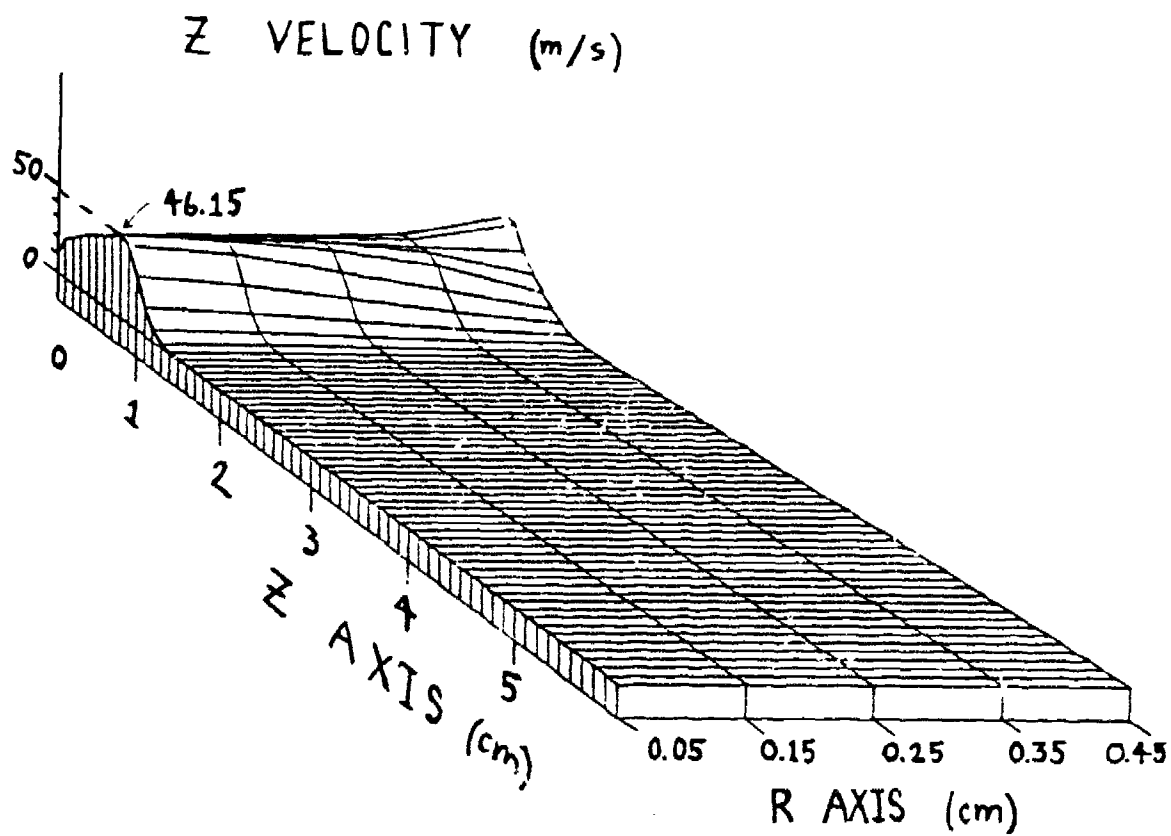
Z VELOCITY (m/s)

Figure 44. Gas Axial Velocity Profile at t = 13.28 μsec
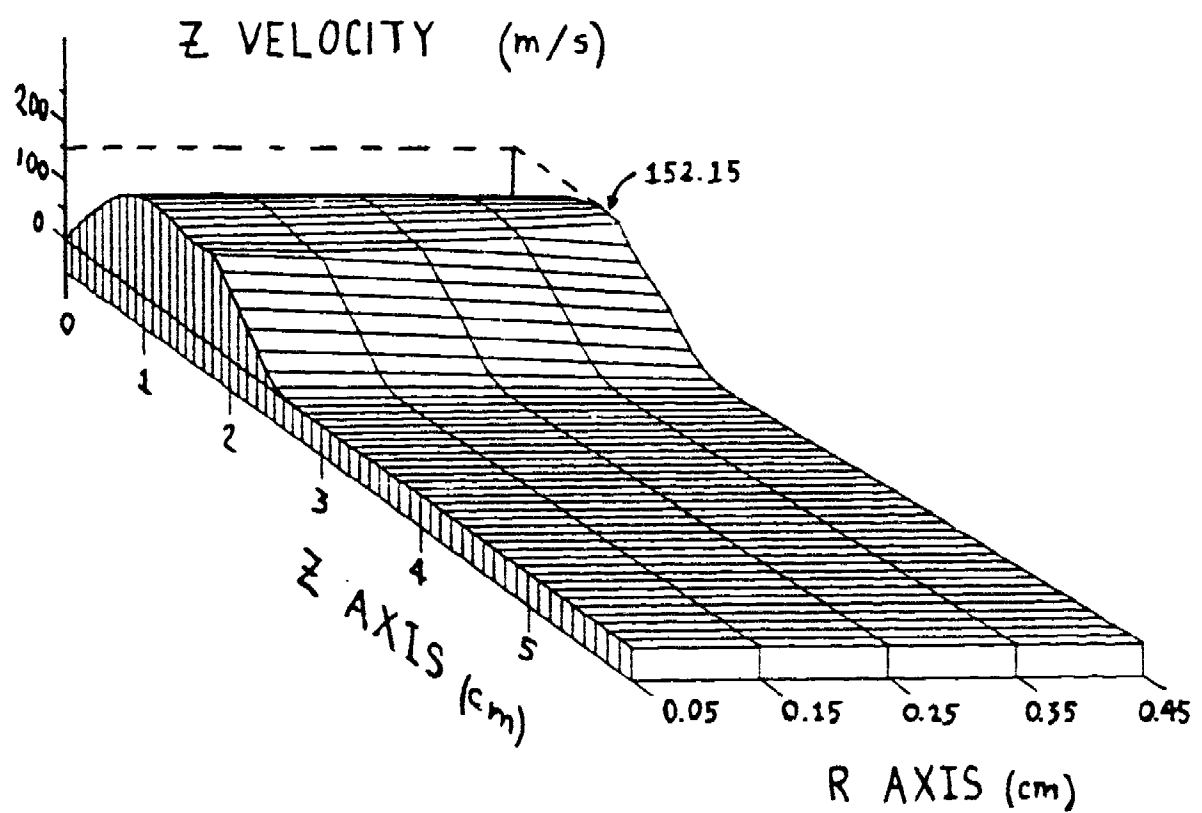
Figure 45. Gas Axial Velocity Profile at t = 34.47 μsec
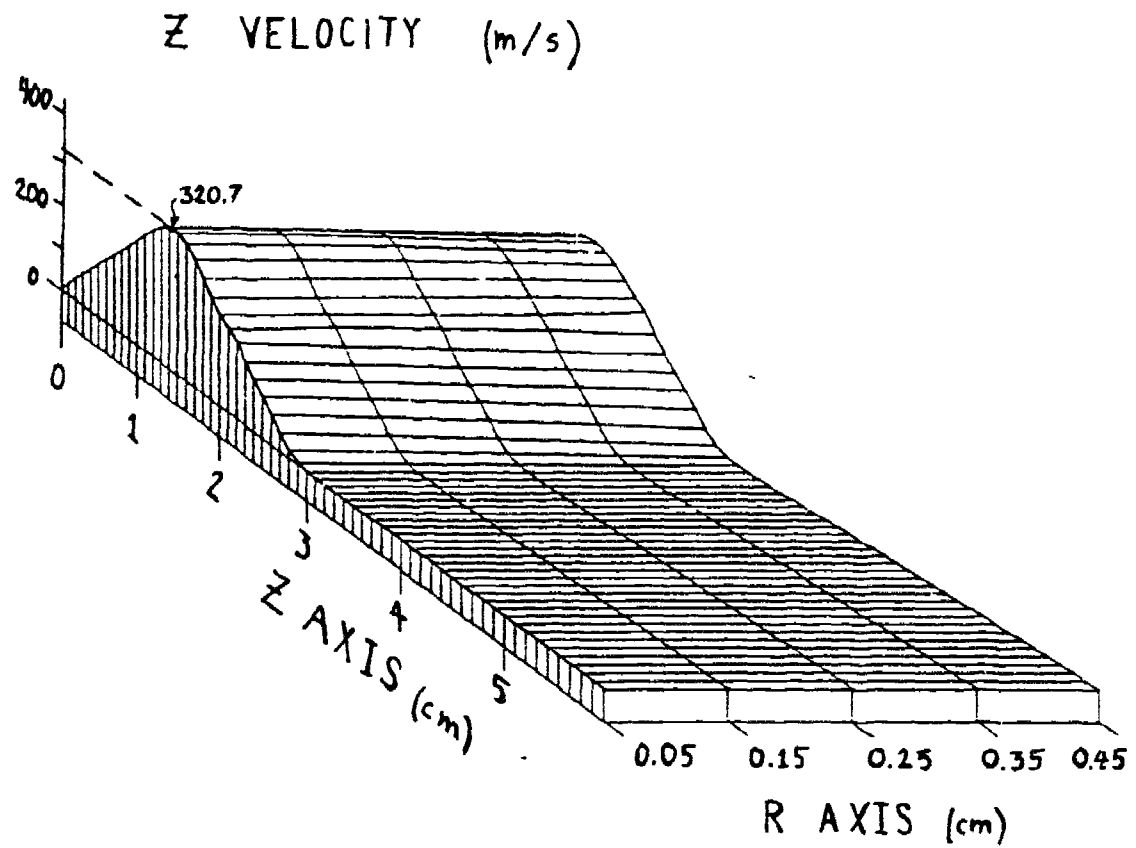
Figure 46. Gas Axial Velocity Profile at t = 39.96 μsec
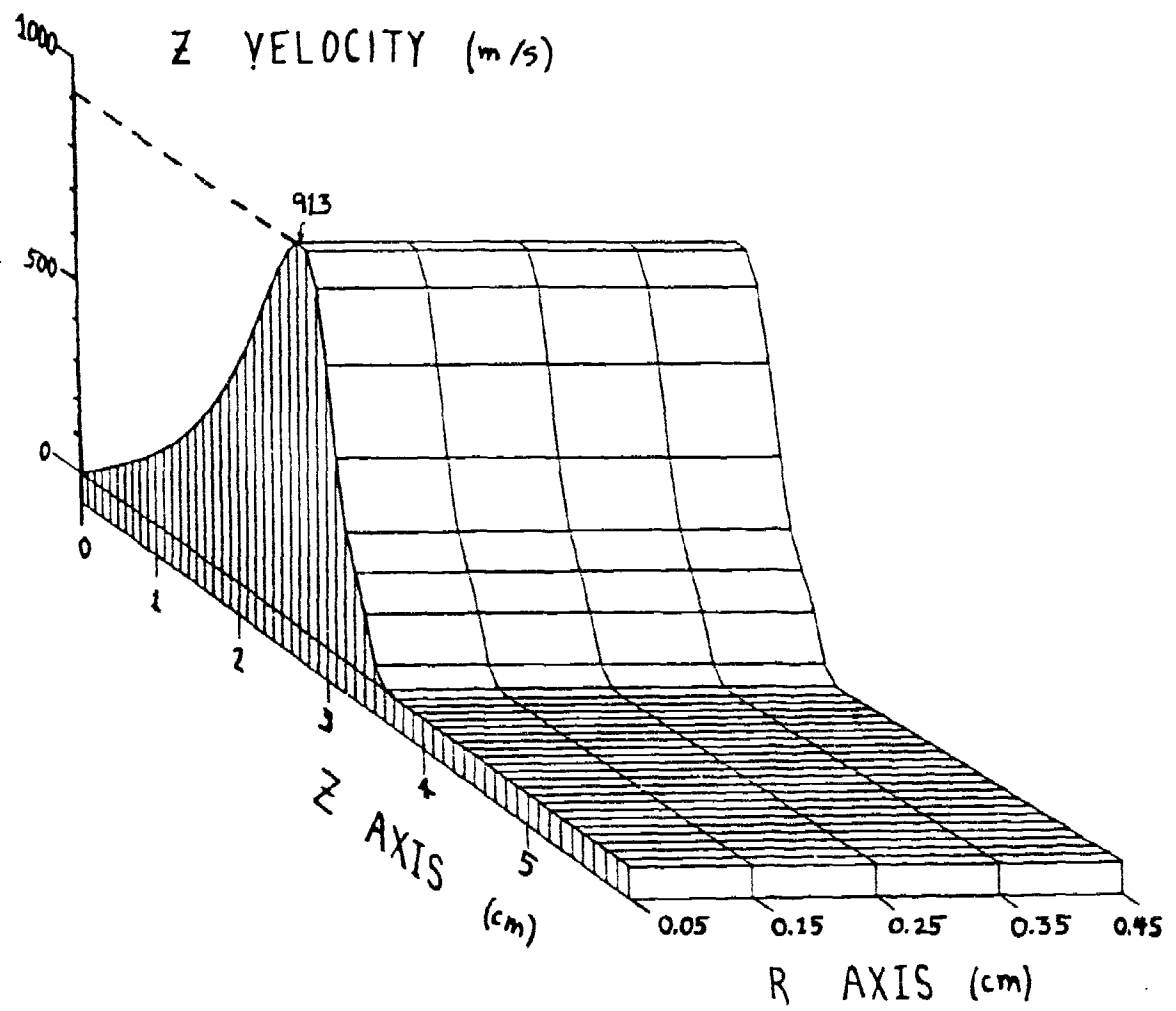
Figure 47. Gas Axial Velocity at t = 46.36 μsec
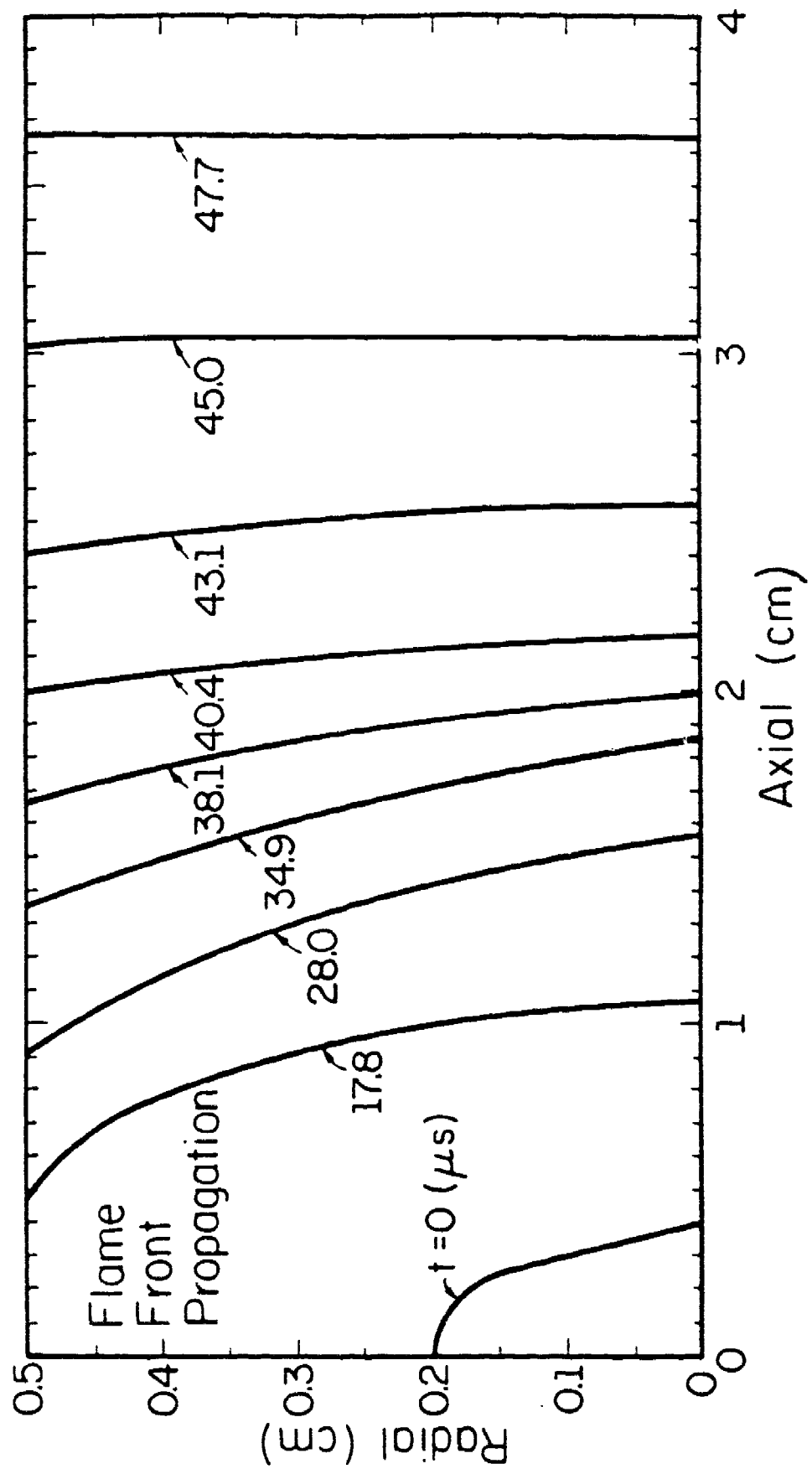
Figure 48. Flame Front Locus Showing Transition from Two-Dimensional Flame
Spreading to One-Dimensional Flame Spreading
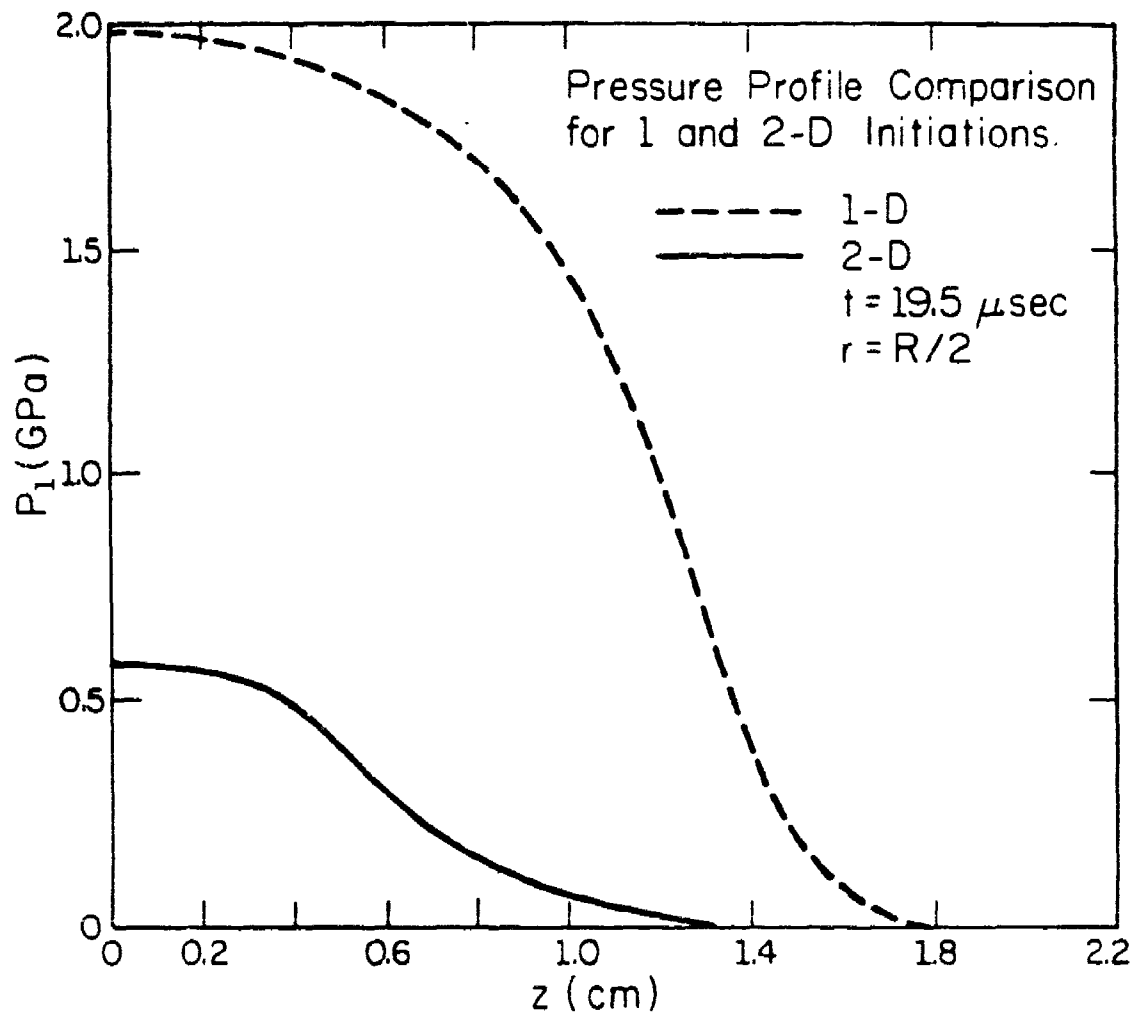
Figure 49. Comparison of Pressure Profiles for One- and Two-Dimensional Initiations
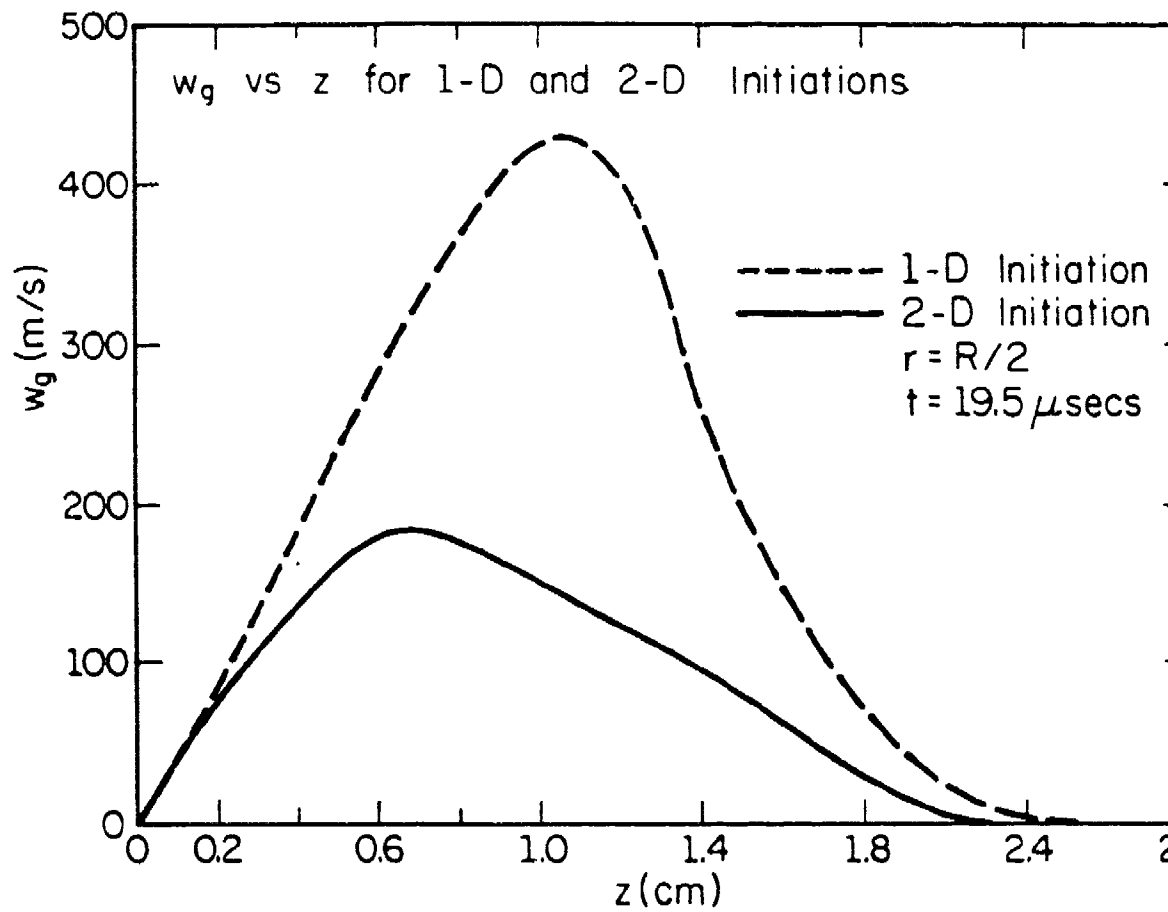
Figure 50. Comparison of the Axial Velocity Profiles for
One- and Two-Dimensional Bed Initiations
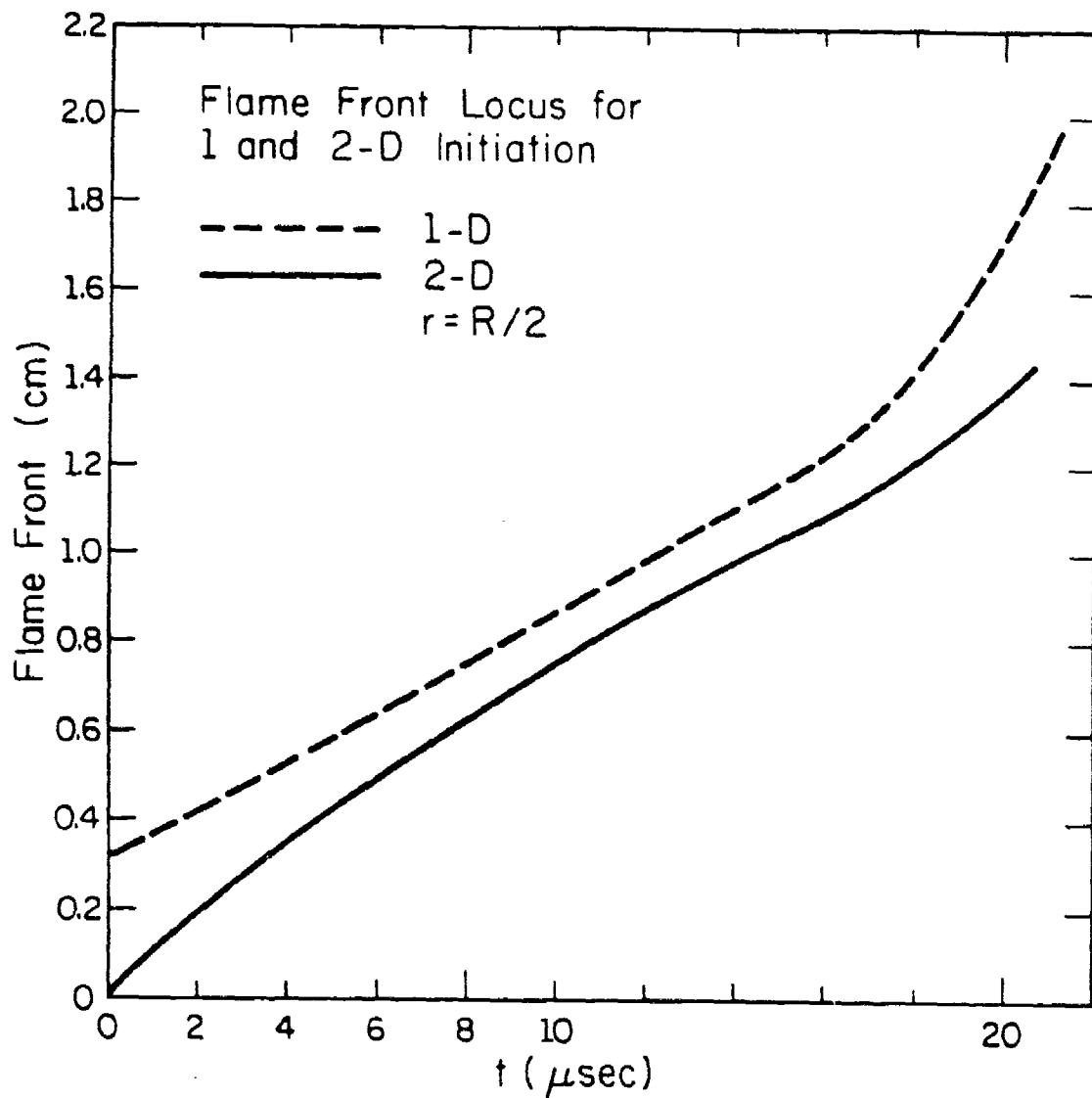
Figure 51. Comparison of the Flame Front Locus for One-
and Two-Dimensional Initiations

109
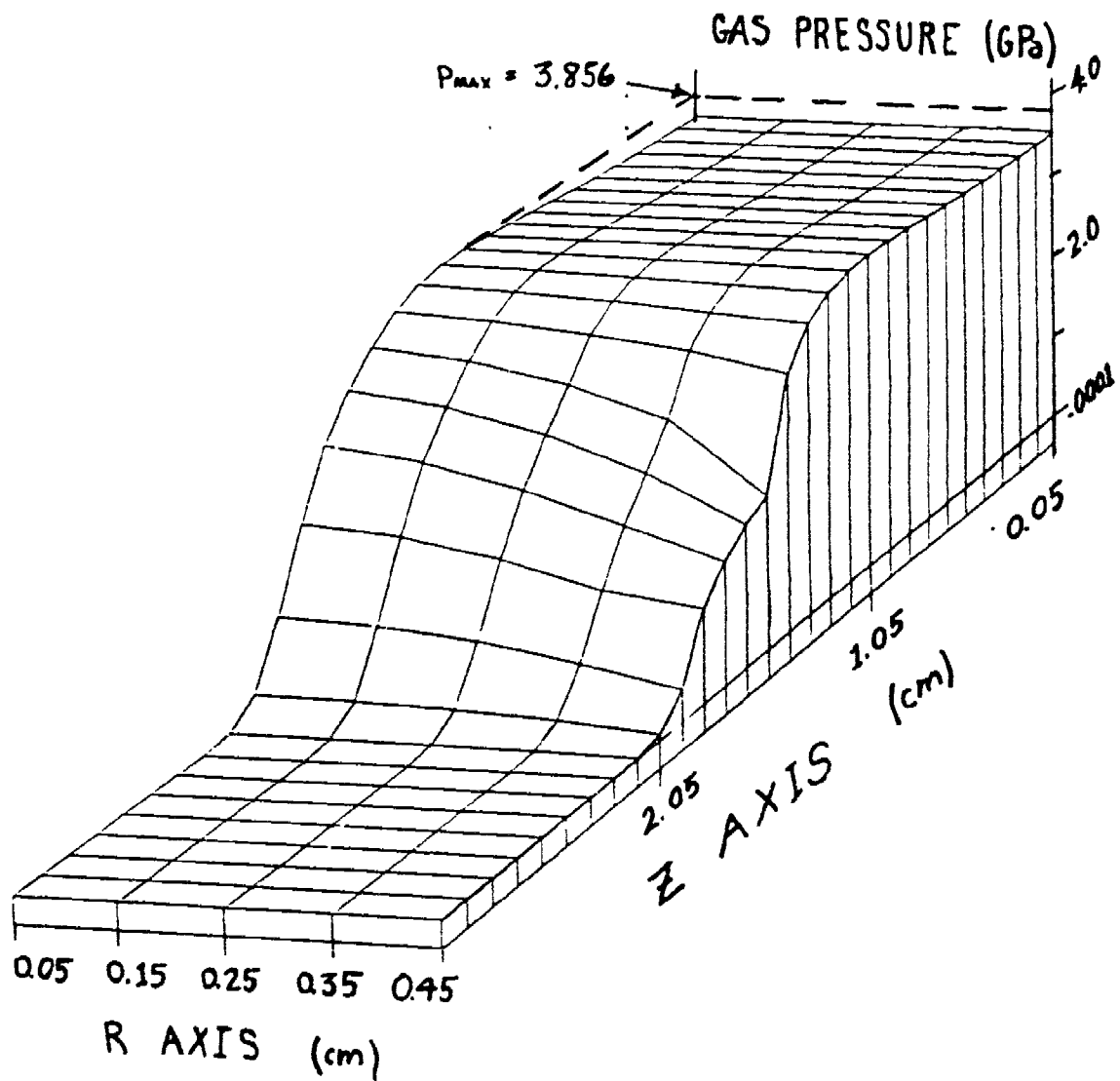
Figure 52.   Gas Pressure Profile at t = 21.48 μsec

GAS PRESSURE (GPa)

$P_{MAX} = 4.386$ →
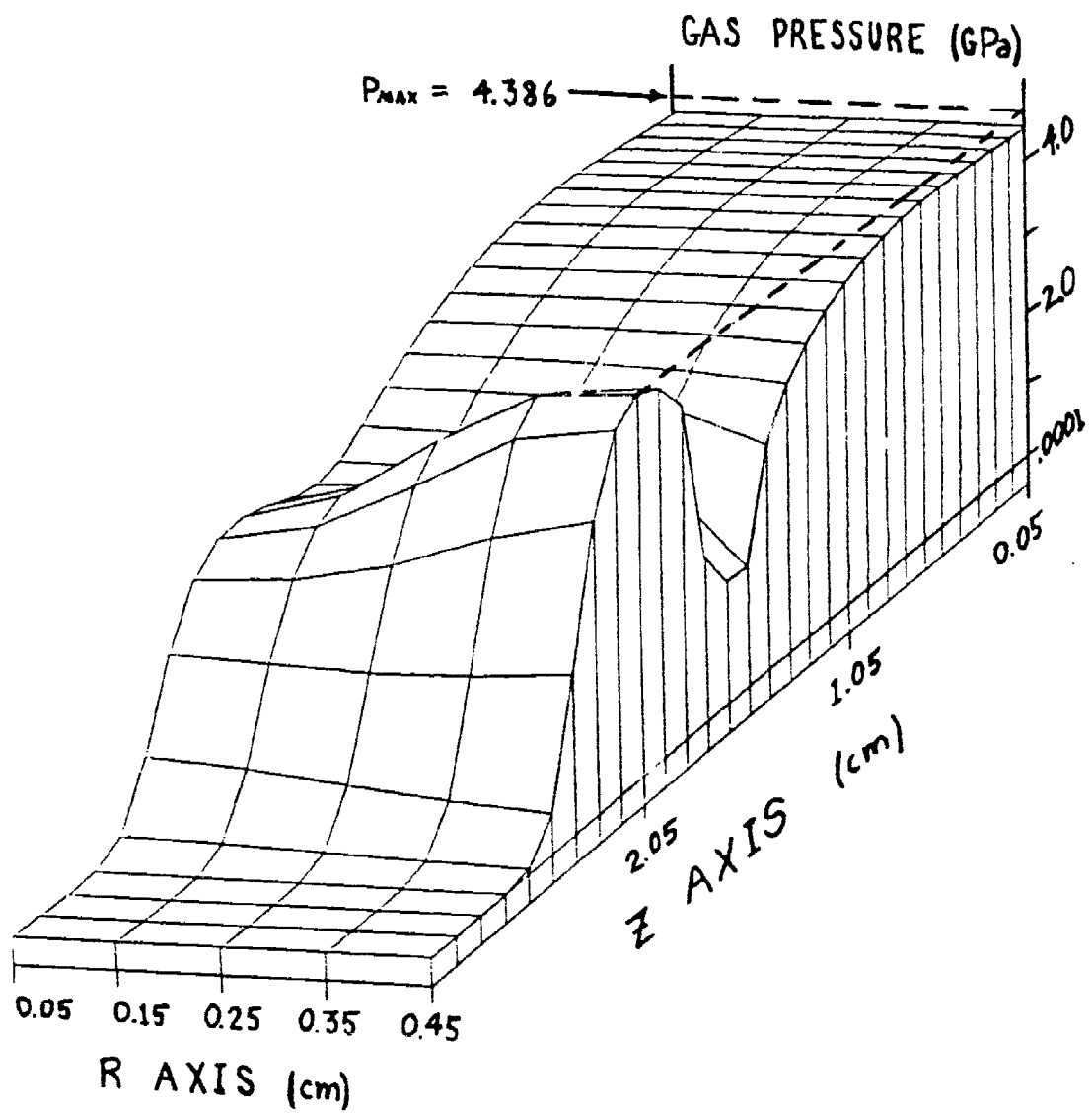
Figure 53.   Gas Pressure Profile at t = 22.97 μsec

111
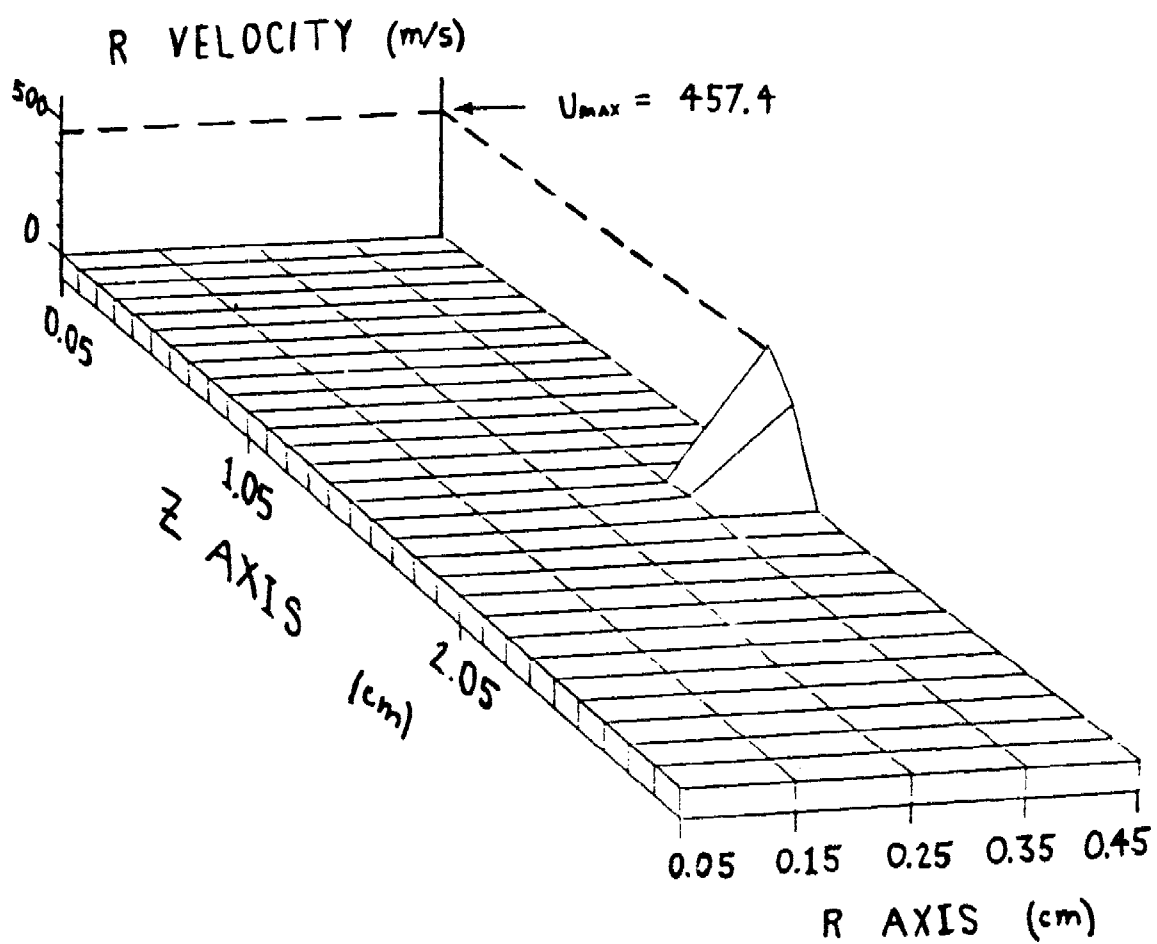
Figure 54. Gas Radial Velocity Profile at t = 18.51 μsec
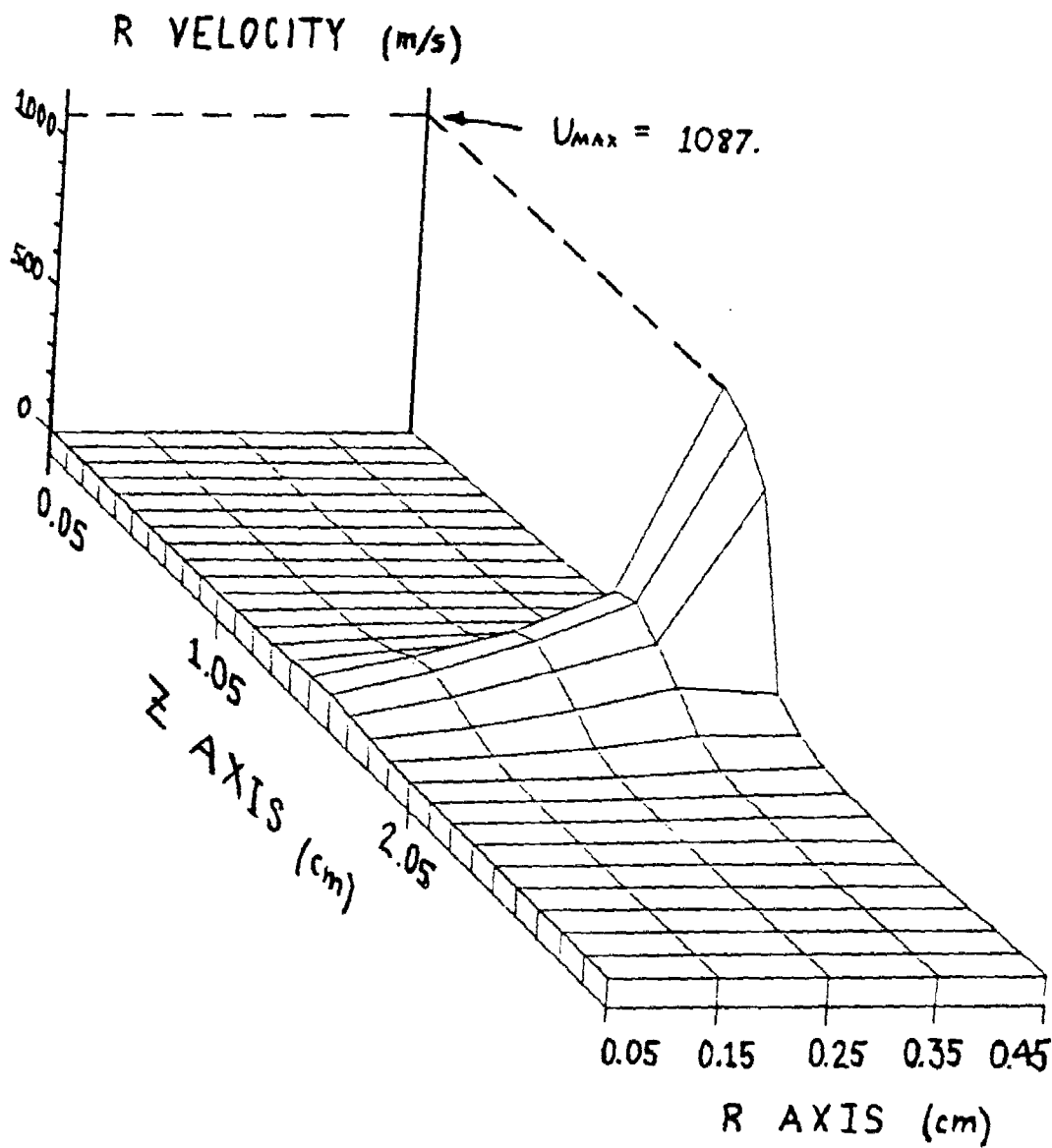
Figure 55.   Gas Radial Velocity Profile at t = 21.48 μsec

113
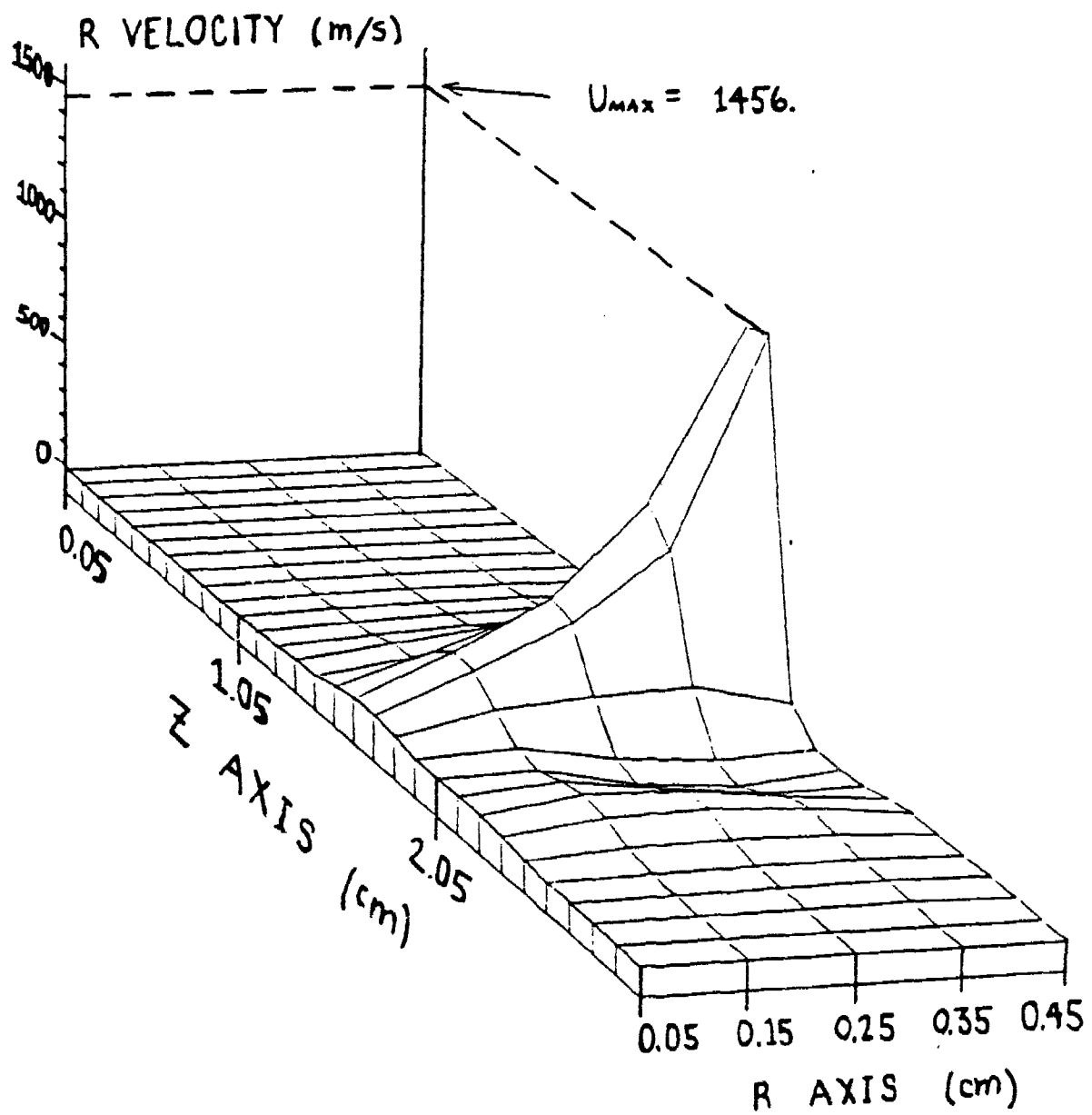
Figure 56.   Gas Radial Velocity Profile at t = 22.97 μsec

114

References

(1)   Krier, H., Van Tassel, W. F., "Combustion and Flame Spreading Phenomena
       in Gas Permeable Explosive Material", *International Journal of Heat and
       Mass Transfer*, Vol. 8, p. 1377-1386, 1975.

(2)   Krier, H. and Gokhale, S., "Vigorous Ignition of Granulated Propellant
       Beds by Blast Impact", *International Journal of Heat and Mass Transfer*,
       Vol. 19, pp 915-923, 1976.

(3)   Krier, H., Rajan, S., and Van Tassel, W. F., "Flame Speading and
       Combustion in Packed Beds of Propellant Grains", *AIAA Journal*, Vol. 14,
       pp 301-309, 1975.

(4)   Dimitstein, M., "A Separated-Flow Model for Predicting the Pressure
       Dynamics in Highly Loaded Beds of Granulated Propellant", MSE Thesis,
       Dept. of Aero/Astro Engineering, University of Illinois at Urbana-
       Champaign 1976.

(5)   Krier, H., Dimitstein, M., and Gokhale, S., "Reactive Two Phase Flow
   Models Applied to the Prediction of Detonation Transition in Granulated
       Solid Propellant", Technical Report AAE 76-3, UILU-Eng 76-0503, UIUC,
       Dept. of Aero/Astro Engineering, July 1971.

(6)   Krier, H., Gokhale, S., and Hughes, E. D., "Modeling of Convective Mode
       Combustion Through Granulated Solid Propellant to Predict Possible
       Detonation Transition", AIAA paper 77-857, Presented at the 19th,
       AIAA/SAE, Propulsion Conference, Orlando, FL, July 1977.

(7)   Krier, H., and Kezerle, J. A., *Seventeenth Combustion Symposium*, The
       Combustion Institute, pp 23-24, 1979.

(8)   Butler, P. B., Lembeck, M. F., and Krier, H., "Modeling of Shock
       Development and Transition to Detonation Initiated by Burning in Porous
       Propellant Beds", *Combustion and Flame*, Vol. 46, pp 75-93, 1982.

(9)   Bernecker, R. R., and Price, Donna, "Studies in the Transition from
       Deflagration to Detonation in Granular Explosives-II Transitional
       Characteristics and Mechanics Observed in 91/9 RDX/Wax", *Combustion and
       Flame* 22, pp 119, 1974.

(10)   Copperthwaite, M. and W. H. Zwisher, "TIGER Computer Code
       Documentation", Rept. PYV-1281, Stanford Research Institute, 1974.

(11)   Krier, H., M. R. Dahm, and P. B. Butler, "Modeling the Burn-to-Violent
       Reaction to Simulate Impact Damaged GP Warheads", *Proceedings of the
       First Symposium on the Interactions of Non-Nuclear Munitions with
       Structures*, U.S. Air Force Academy, Colorado, pp 37, May 1983.

(12)   Gary, J., "The Method of Lines Applied to a Simple Hyperbolic
       Equation", *Journal of Computational Physics*, Vol. 22, No. 2, pp 131-

149, October 1976.

(13) Markatos, N. C. and D. Kircaldy, "Analysis and Computation of Three-Dimensional, Transient Flow and Combustion Through Granulated Propellants", _International Journal of Heat and Mass Transfer_, Vol. 26, No. 7, pp 1037-1053, 1983.

(14) Kurihara, Y. "On the Use of Implicit and Iterative Methods for the Time Integration of the Wave Equation", Monthly Weather Report, Vol. 93, No. 1, pp 33, June 1965.

(15) Williams, G. "Numerical Integration of the Three-Dimensional Navier-Stokes Equations for Compressible Flow", _Journal of Fluid Mechanics_, Vol. 37, Part 4, pp 727-750, 1969.

(16) Richtmeyer, R. D. and K. W. Morton, _Difference Methods for Initial Value Problems_, New York: Interscience Publishers, 1967.

(17) Miyakoda, K. "Contribution to the Numerical Weather Prediction: Computation with Finite Difference", _Jap. J. Geophys_, 3, pp 75, 1962.

(18) Arakawa, A., "Computation Design for Long Term Numerical Integration of the Equations of Fluid Motion, Two-Dimensional Incompressible Flow. Part 1", _Journal of Computational Physics_, 1, pp 119, 1966.

(19) Wilhelmson, R., ATMOS 405-A, Numerical Methods in Fluid Dynamics; Lecture Notes, University of Illinois, Dept. of Atmospheric Sciences, Fall 1983.

(20) Ames, W. F., _Nonlinear Partial Differential Equations in Engineering_, New York: Academic Press, 1965.

(21) Sod, Gary A., "A Survey of Several Finite Difference Methods for Systems of Nonlinear Hyperbolic Conservation Laws", _Journal of Computational Physics_, 27, pp 1-37, 1978.

(22) Krier, H., S. Y. Wang, and P. B. Butler, "Non-Ideal Equations of State for Deflagration-to-Detonation Transition Dynamics in Porous HMX Propellants or Explosives", in preparation.

(23) Jacobs, S. J., Private Communications with H. Krier and S. S. Gokhale, White Oak Laboratory, Silver Springs, MD, March 1978.

(24) Wallis, G. B., _One-Dimensional Two-Phase Flow_, New York: McGraw-Hill Book Company, 1969.

(25) Kuo, K. K., and Nydegger, C. C., _Journal of Ballistics_, 2(1): 1-25, 1978.

APPENDIX A

CONSTITUTIVE RELATIONS

To totally describe the process occurring in the combusting explosive media, we must be able to find the instantaneous values of ρ_g, ρ_p, u_g, u_p, T_g, T_p, P_g, P_p and ϕ. The six conservation equations allow us to solve for six of these variables. In addition to these equations, three constitutive relations are needed for closure:

(i) An Equation of State for the Gaseous Products Phase:

In this work we utilized a non-ideal equation of state for hard spheres suggested by S. J. Jacobs (Reference [23]). This equation of state was written as:

$$P_g = \rho_g R' T_g \ (1 + b_1 \rho_g) \tag{A-1}$$

Ideally, the coeficient b_1 should be a function of the density. However, in this analysis, b_1 was considered a constant.

While offering good correlation with experimental values at relatively low pressures, there is some question about the accuracy of this equation of state at the extremely high pressures (10-20 GPa) which can be achieved in a bed of combusting particles. Work is currently being performed by Krier and Wang (Reference [22]) to develop an equation of state which is valid at these extreme pressures.

(ii) An Equation of State for the Solid Particle Phase:

117

Here, the Tait equation of state was used to predict the density of the solid particles:

$$\rho_p = (\frac{3P_p}{K_o} + 1)^{1/3} \rho_{p_o} \qquad \text{(A-2)}$$

(iii) A Relation for Predicting the Porosity, ϕ:

Since no relationship for the porosity of a packed bed of particles which is reliable under the range of conditions imposed by this problem is known, this condition was replaced by an equilibrium condition which states that at each instant of time, the particle pressure is equal to the gas pressure. The porosity is then predicted for each new time step by taking the value of ρ_2 predicted by Equation (2) and dividing it by the solid phase density from the previous time step. While this procedure does introduce some error into the prediction of ϕ, this error will be quite small since the time steps used in this model are quite small and the density of the solid phase will not change much between adjacent time steps.

In addition to these equations, relations are needed to solve for the heat transfer, drag, and burning rate.

(iv) A Relation for the Interphase Heat Transfer Term, $\dot{Q}$:

The relations used to find the heat transfer between the hot gases and the particles were:

$$\dot{Q} = h_{pg}(T_g - T_p) \cdot \frac{3(1-\phi)}{r_p} \qquad \text{(A-3)}$$

$$h_{pg} = \frac{k_g}{r_p} (1 + 0.2 \ Re_r^{0.7} \ Pr^{0.33}) \qquad \text{(A-4)}$$

where the gas thermal conductivity is defined as:

$$k_g = \mu_g(R' + C_{v_g})/Pr \qquad\qquad (A-5)$$

and the interphase viscosity is given by:

$$\mu_g = \mu_{g_0}(T_g/T_{g_0})^{0.65} \qquad\qquad (A-6)$$

The Reynolds Number used in this work is given by Wallis [24] for two-phase flow as:

$$Re_r = 2\ r_p \rho_1 |(u_p - u_g)|/\mu_g \qquad\qquad (A-7a)$$

For the three dimensional model described in Section II, a variation of this form of the Reynolds Number was used:

$$Re_r = 2r_p\rho_1 |(u_p^2 + v_p^2 + w_p^2)^{0.5} - (u_g^2 + v_p^2 + w_p^2)^{0.5}|/\mu_g$$
$$(A-7b)$$

(v) A Relation for the Gas-Particle Drag, D:

The relation used for the interphase drag in this work are given as:

$$D = \mu_g[(u_g - u_p)/(4r_p^2)]\cdot f_{pg} \qquad\qquad (A-8)$$

$$f_{pg} = (\frac{1-\phi}{\phi})^2 (276 + 5[\frac{Re}{1-\phi}]^{0.87}) \qquad\qquad (A-9)$$

119

This relation was derived experimentally by Kuo and Nydegger (Reference [25]) for steady flow in a packed bed of spheres at constant porosity for Reynold's number ranging from 460 to 14,600. The problem being considered here is unsteady and has Reynold's numbers which greatly exceed this range. However, at the present time there does not appear to be any relationship in use which is any more reliable.

(vi) A Relation for the Gas Production Rate, Γ:

$$\Gamma = \frac{3}{r_p} (1 - \phi) \rho_p \dot{r} \qquad (A\text{-}10)$$

where r_p is the instantaneous particle radius and $\dot{r}$ is the surface burning rate given by:

$$\dot{r} = a \, P_g^{\,n} \qquad (A\text{-}11)$$

While some of the relations used in this work were applied under conditions which lay outside their stated domain, this should not detract anything from the reliability of the results obtained herein. Rather, the development of constitutive relations which are tailored to the extreme range of conditions encountered in this type of work will merely help to fine tune the previous results.

APPENDIX B

THE SPEED OF SOUND IN A NON-IDEAL GAS

In Section II we formulated a partial confinement model which assumed that the gas escaped from each damaged control volume at the choked velocity. We must then determine the speed of sound in the non-ideal gas which is produced in the burning particles. Recall that our non-ideal equation of state had the form:

$$P = \rho R'T(1 + b_1\rho) \qquad \text{(B-1)}$$

Recall also that the First Law gives us:

$$de = \delta Q - pdv \qquad \text{(B-2)}$$

If we use

$$de = C_v dT \qquad \text{(B-3)}*$$

and the Second Law

$$ds = \frac{\delta Q}{T} \qquad \text{(B-4)}$$

we can re-write (B.2) as

$$C_v dT = Tds - pdv \qquad \text{(B-5)}$$

Combining the above equations yields the result

$$ds = C_v \frac{dT}{T} - \frac{R'}{\rho} (\rho + b_1 \rho^2) \frac{d\rho}{\rho} \tag{B-6}$$

Equation (B-6) can be rearranged as

$$T = \frac{P}{R'(\rho + b_1 \rho^2)}$$

After some mathematical manipulation, we can show that

$$\frac{dT}{T} = \frac{dP}{P} - \frac{(1 + 2b_1\rho)}{(1 + b_1\rho)} \frac{d\rho}{\rho} \tag{B-7}$$

Substituting this into (B.6), we get

$$ds = C_v \frac{dP}{P} - \left[\frac{C_v(1+2b_1\rho) + R'(1+b_1\rho)^2}{(1 + b_1\rho)} \right] d\rho/\rho \tag{B-8}$$

Recalling that the speed of sound is given by

$$a^2 = \left(\frac{\partial P}{\partial \rho} \right)_s$$

Equation (B-8) gives us that

$$a = SQRT \left[\frac{C_v(1+2b_1\rho) + R'(1+b_1\rho)^2}{C_v\rho(1+b_1\rho)} P \right] \tag{B-9}$$

*That Equation (B-3) holds true for the non-ideal equation of state used here can easily be shown by writing the internal energy as

$$de = \left(\frac{\partial e}{\partial T}\right)_V dT + \left(\frac{\partial e}{\partial v}\right)_T dv$$

and applying the First and Second Laws of Thermodynamics and using Maxwell's relations.

DERIVATION OF THE CONSERVATION EQUATIONS

In Section III, the ten conservation equations for the unsteady, three dimensional separated flow model were presented in their finished form. In this appendix, the key steps in deriving these equations will be presented.

Gas Phase Continuity

Consider a three dimensional cylindrical control volume element with sides of finite length dr, dθ, and dz. Mass is flowing through the volume in the $\vec{r}$, $\vec{\theta}$, and $\vec{z}$ directions. Performing a mass balance on this control volume:

Mass increase in C.V. in time t = net mass flux through C.V. in time t + mass generated in C.V. in time t

$$\frac{\partial(\rho_g V_g)}{\partial t} = (\dot{m})_r - (\dot{m})_{r+dr} + (\dot{m})_\theta - (\dot{m})_{\theta+d\theta} + (\dot{m})_z - (\dot{m})_{z+dz} + \Gamma_c V_T$$

$$(C-1)$$

Here, V_g = volume of gas phase and V_T = total volume of control cell. Using a Taylor Series to expand the flux terms about r+dr, θ+dθ, and z+dz, we get

$$\frac{\partial(\rho_g V_g)}{\partial t} = \dot{m}_r - \left\{ \dot{m}_r + \frac{\partial \dot{m}_r}{\partial r} dr + \frac{\partial^2 \dot{m}_r}{\partial r^2} dr^2 + - - - - \right\}$$

$$+ \dot{m}_\theta - \left\{ \dot{m}_\theta + \frac{\partial \dot{m}_\theta}{\partial \theta} d\theta + \frac{\partial^2 \dot{m}_\theta}{\partial \theta^2} d\theta^2 + - - - - \right\}$$

$$+ \dot{m}_z - \left\{ \dot{m}_z + \frac{\partial \dot{m}_z}{\partial z} dz + \frac{\partial^2 \dot{m}_z}{\partial z^2} dz^2 + - - - - \right\}$$

$$+ \Gamma V_T$$

124

or

$$\frac{\partial(\rho_g V_g)}{\partial t} = - \left\{ \frac{\partial \dot{m}_r}{\partial r} dr + \frac{\partial^2 \dot{m}_r}{\partial r^2} dr^2 + - - - - \right\}$$

$$- \left\{ \frac{\partial \dot{m}_\theta}{\partial \theta} d\theta + \frac{\partial^2 \dot{m}_\theta}{\partial \theta^2} d\theta^2 + - - - - - \right\}$$

$$- \left\{ \frac{\partial \dot{m}_z}{\partial z} dz + \frac{\partial^2 \dot{m}_z}{\partial z^2} dz^2 + - - - - - \right\}$$

$$+ \Gamma V_T \qquad\qquad (C-2)$$

For a cylindrical control volume $V_g = r dr d\theta dz \phi$. Since the volume of the control cell is invariant with time, it may be pulled out of the time derivative on the left hand side. Dividing by V_g, we get

$$\frac{\partial(\rho_g \phi)}{\partial t} = - \frac{1}{r d\theta dz} \left\{ \frac{\partial \dot{m}_r}{\partial r} + \frac{\partial^2 \dot{m}_r}{\partial r^2} dr + - - - - \right\} \qquad (1)$$

$$- \frac{1}{r dr dz} \left\{ \frac{\partial \dot{m}_\theta}{\partial \theta} + \frac{\partial^2 \dot{m}_\theta}{\partial \theta^2} d\theta + - - - - \right\} \qquad (2)$$

$$- \frac{1}{r dr d\theta} \left\{ \frac{\partial \dot{m}_z}{\partial z} + \frac{\partial^2 \dot{m}_z}{\partial z^2} dz + \right\} + \Gamma \qquad (C-3)$$

Now consider the first group of terms (1) on the right-hand side (R.H.S.) of Equation (C-3):

$$- \frac{1}{r d\theta dz} \left\{ \frac{\partial \dot{m}_r}{\partial r} + \frac{\partial^2 \dot{m}_r}{\partial r^2} dr + - - - - \right\}$$

Now:

125

$$\dot{m}_r = \rho_g A_r u_g$$

$$A_r = rd\theta dz\phi$$

Therefore, we get:

$$-\frac{1}{rd\theta dz} \left\{ \frac{\partial}{\partial r} (\rho_g rd\theta dz\phi u_g) + \frac{\partial^2}{\partial r^2} (\rho_g rd\theta dz\phi u_g) \, dr + - - - - \right\}$$

Since $d\theta$ and dz are not functions of r, they may be pulled out of the derivative. Therefore, we get:

$$-\frac{1}{r} \left\{ \frac{\partial}{\partial r} (\rho_1 ru_g) + \frac{\partial^2}{\partial r^2} (\rho_1 ru_g) \, dr + - - - - \right\}$$

By defining

$$\dot{m}_\theta = \rho_g A_\theta v_g$$

$$A_\theta = drdz\phi$$

and

$$\dot{m}_z = \rho_g A_z W_g$$

$$A_z = rdrd\theta\phi$$

and performing the same analysis on groups (2) and (3), we finally get:

$$\frac{\partial(\rho_1)}{\partial t} = -\frac{1}{r} \left\{ \frac{\partial}{\partial r} (r\rho_1 u_g) + \frac{\partial^2}{\partial r^2} (r\rho_1 u_g) \, dr + - - - - \right\} \quad (1)$$

126

$$- \frac{1}{r} \left\{ \frac{\partial}{\partial \theta} (\rho_1 v_g) + \frac{\partial^2}{\partial \theta^2} (\rho_1 v_g) \, d\theta + - - - - \right\} \quad (2)$$

$$- \left\{ \frac{\partial}{\partial z} (\rho_1 w_g) + \frac{\partial^2}{\partial z^2} (\rho_1 v_g) \, dz + - - - - \right\} \quad (3)$$

$$+ \Gamma \qquad\qquad\qquad\qquad (C-4)$$

If we now take $\lim dr \to 0$, all of the higher order terms in group (1) approach zero. Similarly, if we take $\lim d\theta \to 0$ and $\lim dz \to 0$, all the higher order terms in groups (2) and (3) go to zero. Finally then, we are left with:

$$\frac{\partial \rho_1}{\partial t} = - \frac{1}{r} \frac{\partial}{\partial r} (r \rho_1 u_g) - \frac{1}{r} \frac{\partial}{\partial \theta} (\rho_1 v_g) - \frac{\partial}{\partial z} (\rho_1 w_g) + \Gamma \quad (C-5)$$

Gas Phase Momentum Equations

Since velocity is a vector function, the momentum equations must be derived in vector form. Consider again a cylindrical control volume. Performing a momentum balance on this control cell:

Momentum increase net momentum net pressure interphase
in C.V. in time t = flux through + stress on C.V. + drag and
                     C.V. in time t   faces   momentum generated
                                                   by combusting particles

$$\frac{\partial}{\partial t} (\rho_g V_g \vec{V}) = (\dot{m}_r \vec{V})_r - (\dot{m}_r \vec{V})_{r+dr} + (\dot{m}_\theta \vec{V})_\theta - (\dot{m}_\theta \vec{V})_{\theta+d\theta}$$

$$(\dot{m}_z \vec{V})_z - (\dot{m}_z \vec{V})_{z+dz} + (P_g A_r)_r - (P_g A_r)_{r+dr}$$

127

$$+ (P_g A_\theta)_\theta - (P_g A_\theta)_{\theta+d\theta} + (P_g A_z)_z - (P_g A_z)_{z+dz}$$

$$- \overline{D} V_g + r \vec{V} V_T \qquad\qquad (C\text{-}6)$$

where

$$\vec{V} = u_g \vec{r} + v_g \vec{\theta} + w_g \vec{z}$$

$$\overline{D} = D_r + D_\theta + D_z$$

Again performing a Taylor Series Expansion as before, we get:

$$\frac{\partial}{\partial t} (\rho_g V_g \vec{V}) = - \left\{ \frac{\partial}{\partial r} (\dot{m}_r \vec{V}) \, dr + \frac{\partial^2}{\partial r^2} (\dot{m}_r \vec{V}) \, dr^2 + - - \right\} \quad (4)$$

$$- \left\{ \frac{\partial}{r\partial\theta} (\dot{m}_\theta \vec{V}) \, rd\theta + \frac{\partial^2}{(rd\theta)^2} (\dot{m}_\theta \vec{V})(rd\theta)^2 + - - \right\} \quad (5)$$

$$- \left\{ \frac{\partial}{\partial z} (\dot{m}_z \vec{V}) dz + \frac{\partial^2}{\partial z^2} (\dot{m}_z \vec{V}) \, dz^2 + - - \right\} \quad (6)$$

$$- \left\{ \frac{\partial}{\partial r} (P\vec{A})_r dr + \frac{\partial^2}{\partial r^2} (P\vec{A})_r dr^2 + - - \right\} \quad (7)$$

$$- \left\{ \frac{\partial}{r\partial\theta} (P\vec{A})_\theta rd\theta + \frac{\partial}{(r\partial\theta)^2} (P\vec{A})_\theta (rd\theta)^2 + - - \right\} \quad (8)$$

$$- \left\{ \frac{\partial}{\partial z} (P\vec{A})_z dz + \frac{\partial}{\partial z^2} (P\vec{A})_z dz^2 + - - \right\} \quad (9)$$

$$- \overline{D} V_g + r V_g \vec{V} \qquad\qquad (C\text{-}7)$$

Let us consider each term separately.

Term 4:

$$\frac{\partial(\dot{m}_r \vec{V})}{\partial r} = \frac{\partial}{\partial r}\left[\dot{m}_r(u_g\vec{r} + v_g\vec{\theta} + w_g\vec{z})\right]$$

$$= \frac{\partial}{\partial r}\left[\dot{m}_r u_g\vec{r} + \dot{m}_r v_g\vec{\theta} + \dot{m}_r w_g\vec{z}\right] \qquad (C-8)$$

Note that $\frac{\partial\vec{r}}{\partial r} = \frac{\partial\vec{\theta}}{\partial r} = \frac{\partial\vec{z}}{\partial r} = 0$. Therefore,

$$\frac{\partial}{\partial r}(\dot{m}_r\vec{V}) = \frac{\partial}{\partial r}(\dot{m}_r u_g)\,\vec{r} + \frac{\partial}{\partial r}(\dot{m}_r v_g)\,\vec{\theta} + \frac{\partial}{\partial r}(\dot{m}_r w_g)\,\vec{z}$$

Now,

$$\dot{m}_r = \rho_g u_g r d\theta dz_\phi$$

Therefore,

$$\frac{\partial}{\partial r}(\dot{m}_r\vec{V}) = d\theta dz\,\frac{\partial}{\partial r}(\rho_1 r u_g^2)\,\vec{r} + d\theta dz\,\frac{\partial}{\partial r}(\rho_1 u_g v_g r)\,\vec{\theta}$$

$$+ d\theta dz\,\frac{\partial}{\partial r}(\rho_1 u_g w_g r)\,\vec{z} \qquad (C-9)$$

or, $\qquad \frac{\partial}{\partial r}(\dot{m}_r\vec{V}) = d\theta dz\left[\frac{\partial}{\partial r}(\rho_1 u_g^2 r)\,\vec{r} + \frac{\partial}{\partial r}(\rho_1 u_g v_g r)\,\vec{\theta}\right.$

$$\left. + \frac{\partial}{\partial r}(\rho_1 u_g w_g r)\,\vec{z}\right] \quad (4^*) \qquad (C-10)$$

Note: the higher order terms will not be expanded, since they will disappear as before. Going on to term 5, we proceed in a like manner, recalling, however, that $\frac{\partial\vec{r}}{\partial\theta} = \vec{\theta}$, $\frac{\partial\vec{\theta}}{\partial\theta} = -\vec{r}$, $\frac{\partial z}{\partial\theta} = 0$. Therefore,

129

$$\frac{\partial(\dot{m}_\theta \vec{V})}{r\partial\theta} = \frac{\partial}{r\partial\theta}\left(\dot{m}_\theta u_g \vec{r} + \dot{m}_\theta v_g \vec{\theta} + \dot{m}_\theta w_g \vec{z}\right)$$

$$= \frac{\partial}{r\partial\theta}(\dot{m}_\theta u_g)\,\vec{r} + \frac{\dot{m}_\theta u_g}{r}\,\vec{\theta} + \frac{\partial}{r\partial\theta}(\dot{m}_\theta v_g)\,\vec{\theta}$$

$$- \frac{\dot{m}_\theta v_g}{r}\,\vec{r} + \frac{\partial}{r\partial\theta}(\dot{m}_\theta w_g)\,\vec{z} \qquad (C-11)$$

Defining

$$\dot{m}_\theta = \rho_1 dr dz v_g$$

We finally get

$$\frac{\partial}{r\partial\theta}(\dot{m}_\theta \vec{V}) = \frac{1}{r}\,drdz\,\left[\left(\frac{\partial}{\partial\theta}\{\rho_1 u_c v_g\} - \{\rho_1 v_g^2\}\right)\vec{r} + \right. \qquad (5^\star)$$

$$\left.\left(\frac{\partial}{\partial\theta}\{\rho_1 v_g^2\} + \{\rho_1 u_g v_g\}\right)\vec{\theta} + \frac{\partial}{\partial\theta}(\rho_1 v_g w_g)\vec{z}\right]$$

$$(C-12)$$

Similarly, recalling that

$$\frac{\partial\vec{r}}{\partial z} = \frac{\partial\vec{\theta}}{\partial z} = \frac{\partial\vec{z}}{\partial z} = 0,$$

we expand term 6 to get

$$\frac{\partial\dot{m}_z \vec{V}}{\partial z} = rdrd\theta\left[\frac{\partial}{\partial r}(\rho_1 u_g w_g)\vec{r} + \frac{\partial}{\partial z}(\rho_1 v_g w_g)\vec{\theta}\right. \qquad (6^\star)$$

$$\left.+ \frac{\partial}{\partial z}(\rho_1 w_g^2)\vec{z}\right] \qquad (C.13)$$

Next we consider term 7 the pressure stress in the $\vec{r}$ -direction:

$$\vec{A}_r = rd\theta dz\phi \; \vec{r}$$

Therefore,

$$\frac{\partial}{\partial r} (P_g\vec{A}_r)dr = \frac{\partial}{\partial r} (rd\theta dz P_g\phi) \; \vec{r} = \; drd\theta dz \frac{\partial}{\partial r} (P_1 r) \; \vec{r}$$

There is another component of the pressure stress in the $\vec{r}$ -direction which is due to the curvilinear nature of our coordinate system. Consider the r,θ projection of our control volume shown in Figure 57. As can be seen from the drawing, there is a component of the pressure force in the $\vec{\theta}$ -face which acts in the $\vec{r}$ -direction. The magnitude of this force is:

$$P_g A_\theta \sin \left(\frac{d\theta}{2}\right) = P_g A_\theta \left(\frac{d\theta}{2}\right) = \frac{P_g}{2} drd\theta dz\phi \qquad (C-14)$$

Since an equal force is acting on the opposite $\vec{\theta}$ -face, the total force is:

$$\vec{F}_T = -P_g drd\theta dz\phi\vec{r} = -P_1 drd\theta dz\vec{r} \qquad (C-15)$$

Therefore, term 7 becomes:

$$\frac{\partial}{\partial r} (P_g\vec{A}_r)_r = drd\theta dz \left(\frac{\partial}{\partial r} (P_1 r) - P_1\right) \vec{r}$$

$$= drd\theta dz \left(P_1 + r \frac{\partial P_1}{\partial r} - P_1\right) \vec{r}$$

131

$$\frac{\partial}{\partial r} (P_g \vec{A}_r)_r = r\,dr\,d\theta\,dz \left[\frac{\partial}{\partial r} (P_1)\right] \vec{r} \quad (7^\star) \tag{C-16}$$

Proceeding to term 8

$$\frac{\partial}{r\partial\theta} (P_g \vec{A}_\theta)_\theta r\,d\theta = \frac{\partial}{r\partial\theta} \left[P_g\,dr\,dz\phi\right] r\,d\theta\,\vec{\theta}$$

$$= r\,dr\,d\theta\,dz \left[\frac{\partial}{\partial\theta} (P_1)\right] \vec{\theta} \tag{C-17}$$

Again there is component of the stress on the $\vec{r}$-face in the $\vec{\theta}$ direction:

$$- P_g\sin\left(\frac{d\theta}{2}\right) A_r + dr + P_g\sin\left(\frac{d\theta}{2}\right) A_r = F_{\vec{r}-\vec{\theta}} \tag{C-18}$$

$$\vec{F}_{\vec{r}\to\vec{\theta}} = P_g\frac{d\theta}{2} d\theta\,dz\phi \; (r - (r+dr))$$

$$\vec{F}_{\vec{r}\to\vec{\theta}} = - \tfrac{1}{2}P_g\,dr\,d\theta^2\,dz\phi$$

Therefore, term 8 becomes:

$$\frac{\partial}{r\partial\theta} (P_g A_\theta^+)_\theta r\,d\theta = dr\,dz\,d\theta \left[\frac{\partial}{\partial\theta} (P_1) - \frac{1}{2} P_1 d\theta\right] \vec{\theta} \quad (8^\star) \tag{C-19}$$

Similarly, term 9 becomes:

$$\frac{\partial}{\partial z} (P_g \vec{A}_z)_z dz = r\,dr\,d\theta\,dz \frac{\partial}{\partial z} (P_1) \quad (9^\star) \tag{C-20}$$

Now, we plug these starred terms back into Equation C.4 and divide out the volume of the control cell and take the limits as dr, dθ, and dz $\to$ 0. After re-arranging the terms, we finally get:

132

Gas Phase $\vec{r}$ Direction Momentum

$$\frac{\partial}{\partial t} (\rho_1 u_g) = -\frac{1}{r} \frac{\partial}{\partial r} (\rho_1 u_g^2 r) - \frac{1}{r} \frac{\partial}{\partial \theta} (\rho_1 u_g v_g) - \frac{\partial}{\partial z} (\rho_1 u_g w_g)$$

$$+ \frac{\rho_1 v_g^2}{r} - \frac{\partial}{\partial r} (P_1) - D_r + \Gamma u_p \qquad (C\text{-}21)$$

Gas Phase $\vec{\theta}$ -Direction Momentum

$$\frac{\partial}{\partial t} (\rho_1 v_g) = -\frac{1}{r} \frac{\partial}{\partial r} (\rho_1 u_g v_g r) - \frac{1}{r} \frac{\partial}{\partial \theta} (\rho_1 v_g^2) - \frac{\partial}{\partial z} (\rho_1 v_g w_g)$$

$$- \frac{\rho_1 v_g w_g}{r} - \frac{1}{r} \frac{\partial}{\partial \theta} (P_1) - D_\theta + \Gamma v_p \qquad (C\text{-}22)$$

Gas Phase $\vec{z}$ -Direction Momentum

$$\frac{\partial}{\partial t} (\rho_1 w_g) = -\frac{1}{r} \frac{\partial}{\partial r} (\rho_1 u_g w_g r) - \frac{1}{r} \frac{\partial}{\partial \theta} (\rho_1 v_g w_g)$$

$$- \frac{\partial}{\partial z} (\rho_1 w_g^2) - \frac{\partial}{\partial z} (P_1) - D_z + \Gamma w_p \qquad (C\text{-}23)$$

Gas Phase Energy Equation

Once again we perform an energy balance on our control volume:

increase in energy

in control volume

over time t

=

net energy flux through

control volume + work done

in moving gas through C.V.

+

heat transfer, drag work,

chemical energy, and kinetic

energy of the combusted particles

$$\frac{\partial(\rho_g E_{gt} V_g)}{\partial t} = [\dot{m}_r(E_{gt} + \frac{P_g}{\rho_g})]_r - [\dot{m}_r(E_{gt} + \frac{P_g}{\rho_g})]_{r+dr}$$

$$+ [\dot{m}_\theta(E_{gT} + \frac{P_g}{\rho_g})]_\theta - [\dot{m}_\theta(E_{gT} + \frac{P_g}{\rho_g})]_{\theta+d\theta}$$

$$+ [\dot{m}_z(E_{gT} + \frac{P_g}{\rho_g})]_z - [\dot{m}_z(E_{gT} + \frac{P_g}{\rho_g})]_{z+dz}$$

$$- \dot{Q}V_T - D_r u_p V_T - D_\theta v_p V_T - D_z w_p V_T$$

$$+ \Gamma (E_{chem}^g + \frac{u_p^2}{2} + \frac{v_p^2}{2} + \frac{w_p^2}{2}) V_T \qquad (C\text{-}24)$$

Proceeding in an identical manner as before, we finally get:

$$\frac{\partial}{\partial t}(\rho_1 E_{gt}) = -\frac{1}{r}\frac{\partial}{\partial r}[\rho_1 u_g r(E_{gt} + \frac{P_g}{\rho_g})] - \frac{1}{r}\frac{\partial}{\partial \theta}[\rho_1 v_g(E_{gt} + \frac{P_g}{\rho_g})]$$

$$- \frac{\partial}{\partial z}[\rho_1 w_g(E_{gt} + \frac{P_g}{\rho_g})] - \dot{Q} - D_r u_p - D_\theta v_p$$

$$- D_z w_p + \Gamma (E_{chem}^2 + \frac{u_p^2}{2} + \frac{v_p^2}{2} + \frac{w_p^2}{2}) \qquad (C\text{-}25)$$
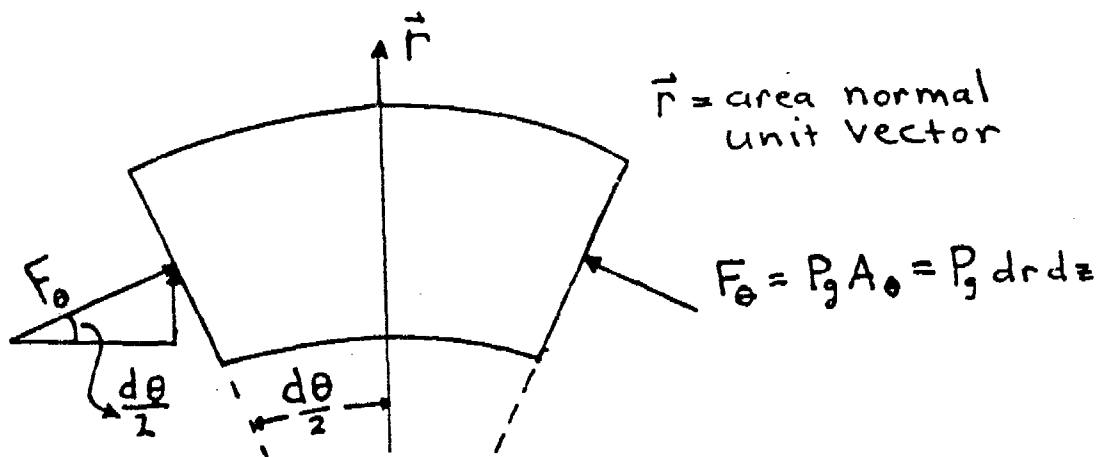
Figure 57. Control Volume Showing Component θ-Stress Acting in the $\vec{r}$-Direction

INITIAL DISTRIBUTION

DTIC-DDAC	2
USA TRADOC SYS ANAL ACTY LIBRARY	1
AUL/LSE	1
FTD/SDNF	1
OO-ALC/MMWMC	1
USA BALLISTIC RES LAB AMXBR-OD-ST	1
USAF/AFSC LIAISON OFFICE CODE 03A4	1
AFWAL/FIESD	1
HQ TAC/XPS	1
AFWAL/FIES/CDIC	2
HQ SAC/NRI	1
AD/XRS	1
AFOSR	1
AD/ENE	1
AFATL/CC	1
AFATL/CCN	1
AFATL/DLODA	1
AFATL/DLODL	2
AFATL/DLJW	1
AFATL/JE	1
HQ USAFE/INATI	1
DEPT OF MECH AND INDUSTRIAL ENGR	10
AFATL/DLYV	2
AD/SES	1